INSTITUTO DE FÍSICA
Universidade Federal Fluminense

Hybrid systems of Graphene and h-BN

Carlos Alberto León Chinchay

Thesis presented as a partial requirement to obtain the degree of PhD in Physics

Supervisor: **Dr. Andrea Latgé**

Niterói – Rio de Janeiro
August 2017

L579 León Chinchay, Carlos Alberto.
Hybrid systems of Graphene and h-BN / Carlos Alberto León Chinchay ; orientador: Andrea Brito Latgé. –- Niterói, 2017.
93 p. : il.

Tese (Doutorado) – Universidade Federal Fluminense, Instituto de Física, Niterói, 2017.
Bibliografia: p. 86-93.

1.MEIO-METAL. 2.GRAFENO. 3.NITRETO DE BORO. 4.DEFORMAÇÃO. 5.POLARIZAÇÃO. I. Latgé, Andrea Brito, orientador. II.Universidade Federal Fluminense. Instituto de Física, Instituição responsável. III.Título.

CDD 530.413

Agradecimentos

A mi familia por todo el apoyo incondicional, por su comprensión, y por su invalorable aliento a seguir adelante. A Nelia, Julián, Michael y Ádila.

A mi orientadora Andrea Latgé, por su paciencia, su guia, su apoyo, y dedicación al trabajo.

Al CNPq por el financiamento.

Abstract

This thesis is devoted to a theoretical study on isolated graphene nanoribbons, isolated hexagonal boron nitrite systems, and other hybrid configurations mixing both kinds of nanoribbon systems. First we analyze the main aspects of the electronic properties of graphene and h-BN nanoribbons including the possibility of getting half metallicity under the presence of external electric fields. Simple tight binding approximations were used as a starting point and real-space normalization schemes are followed to derive Green's functions, local density of states, and also some transport properties such as the conductance. We then construct a hybrid graphene-BN nanoribbon system, using a Hubbard model Hamiltonian within a mean field approximation. Due to different electronegativities of the boron and nitrogen atoms, an electric field is induced across the zigzag graphene strip, breaking the spin degeneracy of the electronic band structure. Optimal tight-binding parameters are found from DFT calculations carried on the Quantum Espresso code, based on density-functional theory, plane waves and pseudopotentials. Edge potentials were proposed as corrections for on-site energies, and to investigate how the BN-graphene nanoribbon interfaces are perturbed. We also study the effects of impurities along the graphene nanoribbon and at the interface regions. We found that energy gap sizes may be properly engineered by controlling the spatial doping process and, moreover, that binding energy impurity calculations may be used to study impurity diffusion processes along the mixed nanoribbons. We show that substitutional impurities may enhance half-metallic response. Different impurity configurations and the corresponding energy stabilities were studied.

In a second study, we consider deformations in graphene nanoribbons that may be considered as central elements in the novel field of straintronics. Various strain geometries have been proposed to produce specific properties, but their experimental realization has been limited. Because strained folds can be engineered on graphene samples on appropriate substrates, we study their effects on graphene transport properties and on the local density of states. Conductance calculations reveal extra channels within the energy range corresponding to the first conductance plateau for the undeformed ribbon, in addition to those due to edge states. Band structure calculations confirm that these channels originate from higher energy states that localize along the strained fold-like area. Furthermore, states with the same velocity show real spatial valley polarization, i.e., a current injected along the deformed structure will be split into two currents: one along the center of the strained fold constituted by states from one valley, and another running at its sides with contributions from states of the other valley. In addition to exhibiting sublattice symmetry breaking, these states are valley polarized, with quasiballistic properties in smooth disorder potentials. These findings could be tested in properly engineered experimental settings. We also investigate the effects of Coulomb correlations on the half metallicity of graphene nanoribbons when mechanical deformations like fold perturbations are taken into account.

Resumo

Esta tese é dedicada ao estudo teórico de nanofitas de grafeno isoladas, nanofitas de nitreto de boro isoladas e algumas outras configurações híbridas que misturam ambos tipos de nanofitas. Inicialmente analisamos os aspectos gerais e calculamos propriedades físicas das nanofitas de grafeno e das nanofitas de BN hexagonal, incluindo a possibilidade de se obter um comportamento de semimetalicidade na presença de campos elétricos externos aplicados na direção transversal das fitas. Hamiltonianos simples na aproximação tight binding são usados como ponto de partida e esquemas de normalização no espaço real são adotados para se derivar funções de Green, densidades de estados eletrônicos locais e ainda algumas propriedades de transporte como a condutância eletrônica. Construímos então um sistema híbrido formado por uma nanofita de grafeno embebida em nanofitas de BN, e adotamos um Hamiltoniano de Hubbard seguindo a aproximação de campo médio. Devido as diferentes eletronegatividades dos átomos de boro e de nitrogênio, um campo elétrico é induzido ao longo da fita zigzag de grafeno embebida, levantando a degnerescência de spin da estrutura de bandas eletrônicas. Neste trabalho procuramos um conjunto de parâmetros otimizados a partir de cálculos obtidos usando o código "Quantum Espresso", baseado na teoria do funcional da densidade (DFT), usando ondas planas e pseudopotenciais. Potenciais de borda e de interface são propostos como correções para as energias "on-site", e para investigar como as nanofitas de BN são perturbadas nas interfaces. Estudamos ainda os efeitos de impurezas do tipo B e N ao longo da região sanduichada da nanofita de grafeno e nas regiões das interfaces. Encontramos que gaps de energia podem ser propriamente manipulados e "engenheirado" a partir do controle do processo de dopagem espacial, e que cálculos de energia de ligação de impurezas podem ser usados para estudar processos de difusão ao longo das nanofitas mescladas. Mostramos ainda que impurezas substitucionais podem aumentar a resposta de semimetalicidade. Diferentes configurações de impurezas e as respectivas estabilidades energéticas são estudadas.

Num segundo estudo consideramos deformações em nanofitas de grafeno, consideradas elementos centrais no novo campo de interesse que é a “straintronics”. Várias geometrias de strain tem sido propostas na literatura para produzir propriedades específicas, mas suas realizações experimentais tem sido bastante limitadas. Como deformações do tipo fold podem ser “engenheirados” em amostras de grafeno sobre substratos apropriados ou mesmo suspensas propomos estudar o efeito destas tensões nas propriedades de transporte e nas densidades de estados local e total desses sistemas quasi-unidimensionais. Cálculos de condutância revelam canais extras no intervalo de energia correspondente ao primeiro plateau quando a fita não está deformada, além daqueles devido aos bem conhecidos estados de borda. Cálculos de estrutura de bandas confirmam que estes canais extras se originam de estados de energia mais alta que se localizam ao longo da área deformada. Além disso, estados com a mesma velocidade mostram polarização de vale no espaço real, i.e., uma corrente injetada ao longo da estrutura deformada será dividida em duas correntes: uma ao longo do centro da perturbação (strained fold) constituída dos estados de um vale, e outra por estados que correm nas laterais da fita com contribuições dos estados de outro vale. Além de exibirem quebra de simetria de rede, estes estados são vale-polarizados, com propriedades quasi balísticas mesmo em potencias de fraca desordem. Estes resultados podem ser testados em arranjos experimentais apropriados. Para finalizar, investigamos os efeitos de correlações Coulombianas sobre a semimetalicidade das nanofitas de grafeno quando deformações mecânicas como as do tipo fold são levadas em conta.

Contents

List of Figures

List of Tables

1

Introduction

In the last decades, 2-dimensional materials have attracted much attention from the scientific community due to their novel properties with no analogy in current Si-based devices, and have lead to a quest for a silicon substitution to continue electronic miniaturization to the quantum level. 2D materials, such as graphene, promise new capabilities compared to its silicon counterpart. The monolayer of carbon atoms arranged in a honeycomb lattice presents a high electronic mobility at room temperature, turning graphene into a candidate for transistor applications, integrated circuit, and electromechanical devices. Suspended graphene exhibited the highest electronic mobility achieved $2.0 \times 10^5\,\mathrm{cm^2V^{-1}s^{-1}}$[19], which is 100 times larger than the electronic mobility of silicon, $1.35 \times 10^3\,\mathrm{cm^2V^{-1}s^{-1}}$[20]. Graphene electronic mobility is the same for electrons and holes due to graphene electron-hole symmetry and it is responsible for the fractional quantum Hall effect[21]. For high quality graphene samples, low energy electrons obey a linear dispersion relation without back-scattering [22], thus achieving its maximum velocity in graphene in the ballistic regime ($v_{\mathrm{Fermi}} \sim 1 \times 10^6\,\mathrm{ms^{-1}}$) as relativistic Dirac fermions. This analogy transforms graphene in a small laboratory for quantum electrodynamics.

Despite of its peculiar electronic properties, graphene is a null-gap material limiting its practical applications. However, this characteristic may be modulated by means of external fields, by introducing other graphene-like materials, or via alternative processes such as the reduction to graphene nanoribbons, which can be made via different techniques[23]. Since its isolation in 2004, Geim and Novoselov have not just presented graphene as a material with unusual electronic and mechanical properties[24], but have also provided the route to the study of other 2D materials [25, 26]. Hexagonal boron nitride sheets, h-BN, molybdene disulphide, MoS_2, and other isostructural graphene analogues promise new electronic capabilities. The search for novel electric responses has led to the study of one-dimensional systems, hybrid materials, and more realistic configurations such as deformed graphitic-like systems. Other attempts to overcome the null gap limitation of graphene include confining the 2D graphene layer into quasi 1D wires. The confinement leads to a discretized band structure, and may result in scenarios with no band crossing at the Fermi level. Also, the confinement may drive the opening of a bandgap, allowing electronic engineering by combining the unique properties of graphene with the inherent properties of quantum confinement. Experimentally, graphene nanoribbons can be synthesized by chemical methods[27] and stacked graphene nanoribbons by the CVD method[28].

Bottom-up methods allows the fabrication of precise graphene nanoribbons by removing halogen atoms from precursor monomers and subsequent thermal procedures[29]. Alternatively, graphene nanoribbons may be generated via unzipping of carbon nanotubes by mechanical sonification[30]. A non-chemical route by cutting multiwalled nanotubes by metal nanoparticles was also proposed by Elias *et. al.*[31]. Following different experimental processes, the quasi 1D graphene nanoribbons emerge as a way to overcome the zero-gap limitation of graphene sheets for its use as a semiconductor with very high electronic mobility in future transistors.

Differently from their 2D counterparts, electronic confinement in nanoribbons provides a frame for gap engineering, with interesting applications in spin-based devices, by modulating external electric or magnetic fields. Actually, electronic correlations and the geometry of zigzag graphene nanoribbons (ZGNRs) under the effects of an electric field give rise to novel responses in which the system appears as a semiconductor for spin up electrons, while behaves as a metallic material for spin down electrons. This half-metallicity behavior promises applications in spintronics and quantum computation[32]. However, the high value of the critical electric field applied to ZGNRs, around $0.1\,\mathrm{V/\AA}$ according to first principle calculations[33], has prompted to new research for other graphene-based materials showing a similar response. A natural tentative was to look for hybrid materials mixing the properties of its components. Specifically, the dielectric properties of an hexagonal boron nitride sheet (h-BN) can be combined with carbon-based materials to fabricate systems with optical bandgap different from the h-BN or graphene sheets[34].

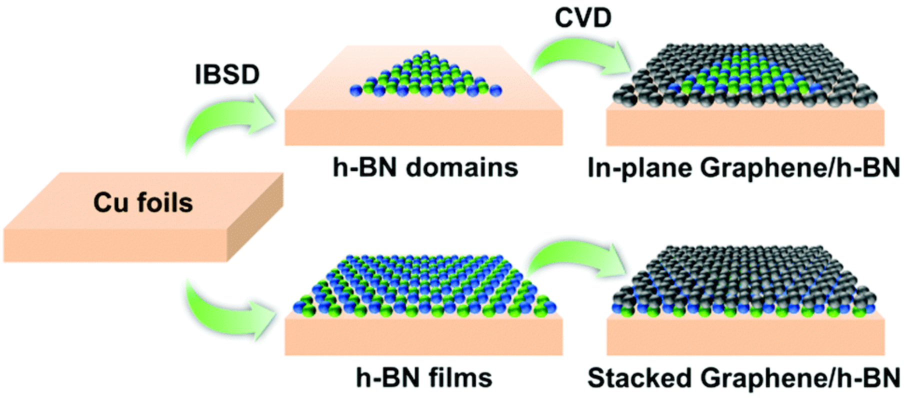

Figure 1.1: Schematic illustration of the growth of graphene/h-BN heterostructures by combining with IBSD and CVD. The h-BN domains and continuous h-BN films were used as the substrates for the growth of in-plane and stacked graphene/h-BN heterostructures, respectively. Taken from Ref. [1].

Hybrid nanoribbons made up of h-BN and graphene can also display half-metallic properties without the need of applying an external electric field. Opposite from what could be naively expected, some imperfection configurations may enhance electronic properties. For example, Li et al[35] took into account line defects in boron nitride nanoribbons and showed that some defect configurations may lead to a half-metallic behavior. Also, a bandgap in zigzag graphene nanoribbons can be opened by doping processes with boron and nitrogen chains[3].

From the experimental point of view, there are many works reporting synthesis of hybrid graphene/h-BN systems. In-plane mixed graphene/h-BN systems have been synthesized by combining ion beam sputtering deposition and chemical vapor deposition [1] as illustrated schematically in Fig.1.1. The characterization of the resulting heterostructures are shown in Fig.1.2 with SEM images of the pre-grown h-BN domains on Cu foils and of graphene grown on h-BN domains with different growth times[1].

Other strategies are also used to fabricate patterned planar graphene/h-BN heterojunctions: BN or graphene is grown on a substrate surface with whole coverage by chemical vapour deposition (CVD), followed by patterned etching and epitaxial re-growth of the second component, as depicted in Fig.1.3(a). SEM images of alternating strip-patterned and non-patterned graphene/h-BN planar heterojunctions, are shown in part (b). The seamless links between the lower graphene and upper BN domains are revealed in the STM image, presented in Fig.1.3(d).

Following these experimental motivations, the state of art on growing quality hybrid samples and the rich physics behind them, we decided to study hybrid systems composed

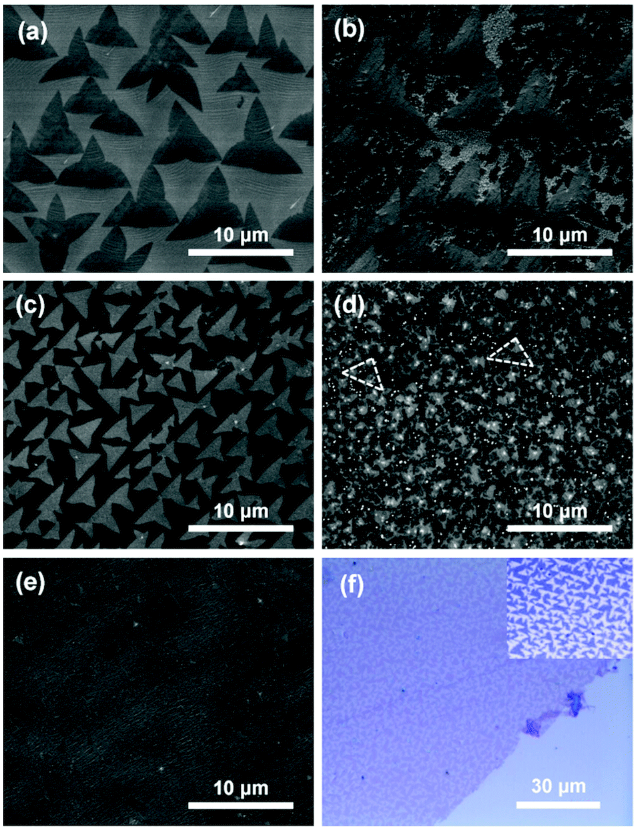

Figure 1.2: Characterization of in-plane graphene/h-BN heterostructures. (a) SEM image of the pre-grown h-BN domains on Cu foils. (b–e) SEM images of graphene grown on h-BN domains with the growth times of (b) 20, (c) 30, (d) 60, and (e) 90 s. The underlying triangular h-BN domains in (d) can be readily distinguished, as highlighted by the white dashed lines. (f) Optical micrograph of the 30 s grown sample transferred onto a SiO2/Si substrate. The inset in (f) reveals that the triangular h-BN domains (lighter colour) are embedded in the percolating graphene film (darker colour). Taken from Ref. [1].

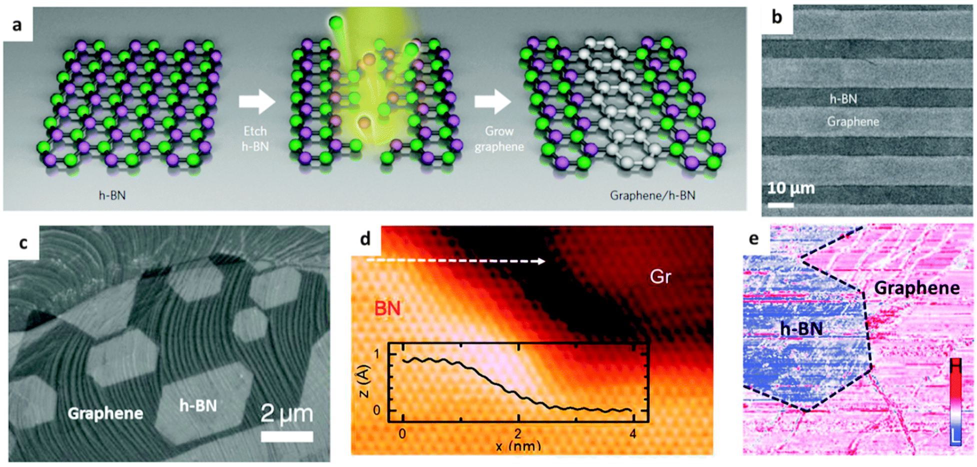

Figure 1.3: (a) Schematic illustration of the procedure fabrications of BN–graphene heterostructures. CVD-grown h-BN sheets are firstly etched by argon ions to obtain the desired patterns, and then CVD growth of graphene on the etched regions is performed. (b) SEM image of strip-patterned BN–graphene heterostructures. (c) SEM image of graphene–BN monolayer heterostructure. The CVD-grown graphene was etched by H2 and then used for epitaxial growth of BN along the graphene edge. (d) STM image of a graphene–BN boundary. The inset is the height profile along the white dashed arrow. (e) The differential tunneling conductance image at the same region in (d). (a and b) are reprinted from Ref. [2], (c–e) are reprinted from [3].

of graphene and h-BN nanoribbons and the possibility of getting half-metallic responses. The challenge was to find a good theoretical model within the tight binding approximation which is able to present a good agreement with first-principles electronic band structures. We worked on hybrid systems composed of an in-plane zigzag graphene stripe embedded in a pair of zigzag BN nanoribbons. We found that due to the different electronegativity of boron and nitrogen, important energy corrections must be implemented and we extended a previous proposed edge potential model [13] to take into account also the carbon-boron and carbon–nitrogen interfaces present in the proposed hybrid systems. Some studies have also been done in this thesis concerning the possible presence of imperfections in the hybrid systems. For that study, we consider B and N migrations into the graphene strip and investigate the possible changes on the gap size of the resulting systems in the presence of such disorder effects (substitutional disorder).

Other types of disorder are also discussed in the present thesis. The disorder degree of a sample is generally related to the choice of the insulating substrate where the 2D system is deposited; excellent graphene samples are grown on h-BN, considered nowadays as a key element for future electronics and optoelectronic applications[36]. On the other hand, recent works have taken advantage of local deformations produced when graphene

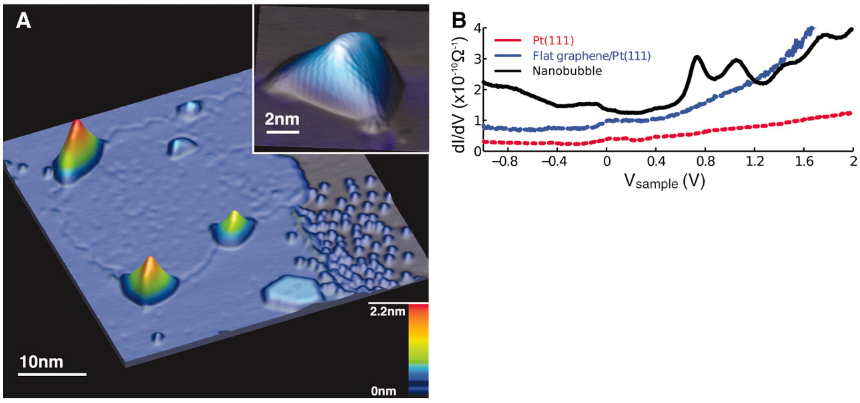

Figure 1.4: STM images and STS spectra taken at 7.5 K. (A) Graphene monolayer patch on Pt(111) with nanobubbles at the graphene-Pt border and in the patch interior ($I_{\text{tunneling}} = 50\,\text{pA}$, $V_{\text{sample}} = 350\,\text{mV}$, 3D z-scale enhanced 4.6x). (Inset) High-resolution image of a graphene nanobubble showing distorted honeycomb lattice resulting from strain in the bubble ($I_{\text{tunneling}} = 50\,\text{pA}$, $V_{\text{sample}} = 200\,\text{mV}$, max $z = 1.6\,\text{nm}$, 3D z-scale enhanced 2×). (B) STS spectra of bare Pt(111), flat graphene on Pt(111) (shifted upward by $3 \times 10^{-11}\,\text{ohm}^{-1}$), and the center of a graphene bubble (shifted upward by $9 \times 10^{-11}\,\text{ohm}^{-1}$). $V_{\text{mod}} = 350\,\text{mV}$. Taken from Ref.[4].

is grown on different substrates or after being mechanically removed from a flake it is vertically stacked forming a graphene/h-BN structure. In this last situation graphene bubbles are formed, inducing important modifications of the electronic properties of the graphene sheet. One of the most interesting is the formation of a pseudo magnetic field that can achieve ultra high values, beyond the experimental real magnetic fields[4] as illustrated in Fig.1.4 in an experiment of graphene on Pt.

Such kind of disorder, may be also experimentally manipulated as an important tool for engineering transport properties of carbon-based materials. The suggestion of using strain to tailor electronic properties has been advanced by several authors[37–53], and pursued in experimental settings [2, 4, 54–56]. Several groups have observed clear signatures of equilibrium properties in strained areas predicted by various models, such as pseudo-Landau levels and sublattice symmetry breaking in STM images [56–58]. Recent works have reported transport measurements on ribbon geometries [59, 60], with one study revealing ballistic transport at room temperatures along nanoribbons deposited on terraced SiC substrates (thus subject to deformations) [61]. This particular geometry highlights the possibility of creating extended strained fold-like structures with unusual transport properties. An example of a kind of fold-strained graphene is illustrated in Fig.1.5, grown on BN. The details of the height profile along the fold perturbation are shown in part (d) of the figure.

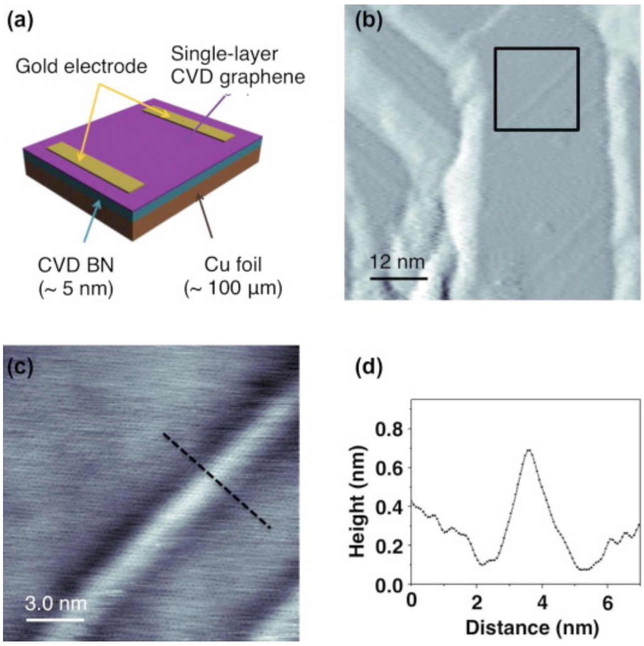

Figure 1.5: (a) A schematic for a epitaxial graphene on hexagonal BN grown on Cu foil. (b) A large-scale derivative STM image obtained from the graphene sample. Image size: $60 \times 60\,\mathrm{nm}$, sample bias: $V_s = -0.3\,\mathrm{V}$, tunneling current: $I = 0.1\,\mathrm{nA}$. (c) An STM image zoomed from the region denoted with a square in (b). Image size: $15 \times 15\,\mathrm{nm}$, sample bias: $V_s = -0.3\,\mathrm{V}$, tunneling current: $I = 0.1\,\mathrm{nA}$. (d) A height profile obtained along a dashed line in (c). Taken from ref.[2].

While models for transport through strained areas have been the topic of several works, transport along deformed areas has been less explored. In fact, due to the peculiar properties of graphene electronic states under strain, extended deformed areas [56] may act as natural electronic waveguides. In this thesis, we studied the case of longitudinal out-of-plane deformations along graphene nanoribbons and show the occurrence of extra conductance channels running parallel to the structure with the remarkable property of being valley polarized. Moreover, we are able to identify a valley-polarization property of such channels. As a consequence, a current injected parallel to the axis of the deformation will naturally split in space, with states from one valley running along the crest while states of the other valley run along the sides. We also show that these channels survive in the presence of highly disordered edges and will behave as quasiballistic for smooth disorder realizations. These results point towards a realistic implementation of valley polarized channels that can be achieved in current experimental settings, by appropriate design of substrates or sample preparation.

The thesis is organized in the following sequence: on Chapter 2 we present all the basic theoretical tools used to discuss the different problems considered. We start with the presentation of the tight binding approximation including Coulomb correlation via a mean field framework, then we present the Green's function formalism used to obtain density of states and transport properties, using the Landauer formula. We show how we calculate the electronic band structures and the localization of the electronic states. As some calculations have been performed within the density function formalism we also dedicate a section to highlight the fundamental ideas and codes used in our calculations. Chapter 3 is devoted to a presentation of the main important physical aspects of the graphene and BN two-dimensional lattices. We focus on the nanoribbon main features of both structures and their responses when submitted to electrical fields. The half-metallicity phenomena is discussed in detail. In Chapter 4, the hybrid system is fully investigated and we present the edge potentials adopted to describe the details of the band structure found by first principle calculations. In Chapter 5 we study transport properties of a nanoribbon when a folded-like mechanical deformation is taken into account. The mapping of strain into pseudomagnetic fields may be seen as a key aspect for engineering electronic properties of folded nanoribbons and valley filtering applications[16]. Finally, we describe the effects of electronic correlation in deformed nanoribbons. The conclusions and perspectives are presented in Chapter 6.

2

Mathematical tools

In this chapter, we describe the mathematical procedures used to calculate the electronic structure of graphene-like nanoribbons. We have considered different theoretical scenarios to better describe the systems considered in this thesis. The idea was to take advantage of first principle calculations in fitting Tight Binding (TB) parameters. First, we describe the Tight Binding model and the self-consistent process of the Hubbard model, implemented in our code. Then, we explain the electronic and transport properties of devices of interest, in the formalism of Landauer. Also, we describe the framework used to calculate band structures, and electronic localization along the nanoribbon. Additionally, we show the recursive Green function renormalization scheme based on Dyson's equation for periodic systems, like the nanoribbons that have been systematically employed in this thesis. Finally, a brief presentation of Density Function Theory is given.

2.1 Tight Binding model with electronic correlation

TB approach is a one-electron model based on the superposition of localized electronic wavefunctions in each atom. A TB model hamiltonian can be written in terms of creation $c_j^\dagger$ and annihilation c_j operators at j-th site as

$$H = \sum_{j\sigma} \varepsilon_j c_{j\sigma}^\dagger c_{j\sigma} + \sum_{\langle ij \rangle \sigma} t_{ij} (c_{j\sigma}^\dagger c_{i\sigma} + c_{i\sigma}^\dagger c_{j\sigma}) \tag{2.1}$$

where ε_j and t_{ij} are the j-th on-site energy and hopping energy between i-th and j-th sites, respectively.

In this model, the electrons are free to move through the system without interacting with other electrons, ignoring the effects of strong intra-atomic coulombian repulsion that sometimes are quite important. Even though this TB model can explain the main features of graphene-like systems, we need a less restrictive approximation allowing to take into account the coulomb interaction at each site, or at least the mean effect of the presence of other electrons in a site. One possibility to overcome this model limitation is to introduce electronic correlation via a Hubbard term as

$$H = \sum_j \varepsilon_j c^\dagger_{j\sigma} c_{j\sigma} + \sum_{\langle ij \rangle \sigma} t_{ij} (c^\dagger_{j\sigma} c_{i\sigma} + c^\dagger_{i\sigma} c_{j\sigma}) + \sum_j U_j n_{j\sigma} n_{j\bar{\sigma}}, \tag{2.2}$$

where $n_{j\sigma} = c^\dagger_j c_j$ is the σ-spin occupation operator acting on the j-th site, and U is the Coulomb energy for two electrons at site j with opposite spins.

In the last expression, the second term of the right side accounts for the electronic itinerant feature. The third term increases the energy due to the coulombian repulsion between a pair of electrons occupying the j-th site. Also, the Hubbard term takes into consideration the Pauli exclusion principle, as the term goes to 0 if electrons with the same spin occupy the same site.

We can realize that the Hubbard term involves a 4-operator product which does not allow a diagonalization of the Hamiltonian. Therefore, we use a mean field approximation to simplify the factor $n_{j\sigma} n_{j\bar{\sigma}}$. In this mean field approximation, we assume that the number of electrons in the j-th site is around an average value with small deviations, i.e

$$n_{j\sigma} \approx \langle n_{j\sigma} \rangle + \delta n. \tag{2.3}$$

So, we can write

$$n_{j\uparrow} n_{j\downarrow} \approx (\langle n_{j\uparrow} \rangle + \delta n_{j\uparrow})(\langle n_{j\downarrow} \rangle + \delta n_{j\downarrow}). \tag{2.4}$$

By neglecting quadratic terms, we arrive to

$$n_{j\uparrow} n_{j\downarrow} \approx \langle n_{j\downarrow} \rangle n_{j\uparrow} + \langle n_{j\uparrow} \rangle n_{j\downarrow} - \langle n_{j\downarrow} \rangle \langle n_{j\uparrow} \rangle, \tag{2.5}$$

where the last term is just a constant and can be omitted (as it represents just a shift in

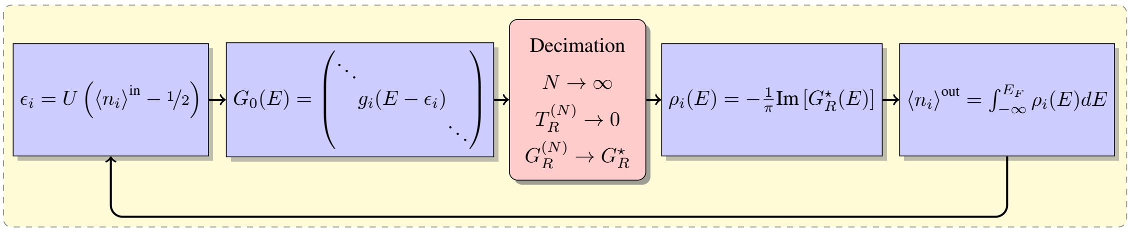

Figure 2.1: Self-consistent process used in the Hubbard model. Decimation or renormalization procedures introduce information about the geometry of the system.

the energy spectrum). Therefore, the hamiltonian can be written as

$$H = \sum_j \varepsilon_j c_j^\dagger c_j + \sum_{\langle ij\rangle} t_{ij}(c_j^\dagger c_i + c_i^\dagger c_j) + \sum_j U_j \left(\langle n_{j\downarrow}\rangle\, n_{j\uparrow} + \langle n_{j\uparrow}\rangle\, n_{j\downarrow}\right). \tag{2.6}$$

This hamiltonian decouples the spin up and down channels and so it can be given as,

$$H = \sum_\sigma H_\sigma \tag{2.7}$$

$$H_\sigma = \sum_j \varepsilon_j c_{j\sigma}^\dagger c_{j\sigma} + \sum_{\langle ij\rangle} t_{ij}(c_{j\sigma}^\dagger c_{i\sigma} + c_{i\sigma}^\dagger c_{j\sigma}) + \sum_j U_j \,\langle n_{j\bar{\sigma}}\rangle\, n_{j\sigma}. \tag{2.8}$$

The decoupled hamiltonian 2.8 indicates that the response of σ-spin electrons depends on the mean field generated by the $\bar{\sigma}$-spin electrons, leading then, to a self-consistent process when solving the hamiltonian. In this work, we use an iterative process, as indicated schematically in Fig.2.1, in a decimation or recursive Green function renormalization, that will be explained later in this chapter (see Section 2.3).

2.2 Transport in nanoconductors

2.2.1 One energy level device

Let us consider a system C, small enough such that the wavelength of their confined electrons is comparable to the size of the system, so its energy spectrum is discrete[62]. We can then, write a time-independent Schrödinger equation for this isolated device,

$$\left(E - \hat{H}_C\right)|\varphi\rangle = 0, \tag{2.9}$$

where E is treated as an *independent variable*, and the eigenvalues are given by the hamiltonian $\hat{H}_C$. If it happens that this device were even smaller in such a way that it is characterized by just one energy level, ε_C, we will have the simple equation $(E-\varepsilon_C)\,|\varphi\rangle = 0$.

Now, let us connect this device to a pair of semi-infinite and macroscopic leads, L (left lead) and R (right lead). By doing so, we gain a new system $L \oplus C \oplus R$. Because of their macroscopic nature, the electrodes are characterized by a continuous energy spectrum, broadening the well defined energy level ε_C. This broadening causes the electron in the device to have a finite life time in this energy level, according to the uncertainty principle $\triangle E \triangle t \geq \hbar/2$. In consequence, the electron has a probability to escape from the device through the electrodes at an average escape rate $\sim 1/\triangle t = \gamma/\hbar$, γ being the broadening of the level ε_C. It is interesting to notice that the escape rate gives us the degree of interaction between the leads and the device; well connected leads are related to high lead-device interactions and high escape rates. This lead-device interaction can be added to the hamiltonian for the isolated device $\hat{H}_C$. The time-dependent Schrödinger equation then reads

$$\left(i\hbar\frac{\partial}{\partial t} - \hat{H} + i\frac{\gamma_L}{2} + i\frac{\gamma_R}{2}\right)|\Psi(t)\rangle = 0, \tag{2.10}$$

from which we can find the temporal part of the eigenstate, i.e.,

$$\exp(-iEt/\hbar)\ \exp(-\frac{\gamma_I}{2\hbar}t)\ \exp(-\frac{\gamma_D}{2\hbar}t). \tag{2.11}$$

The probability of finding an electron in the system is then given by

$$n \propto \exp(-\gamma_L t/\hbar)\ \exp(-\gamma_R t/\hbar), \tag{2.12}$$

i.e. the electronic density decreases time-exponentially at a rate $\gamma_{L(R)}t/\hbar$ trough the $L(R)$ lead.

Here, we use the assumptions done in the Landauer formalism, as dismissing the interaction between the electrodes, and the influence of electrons in the leads over the electrons in the device[63].

Let us consider a perturbation given by a flux of electronic charges from the left lead, described by the state $|s_L\rangle$, coming from L to C. Mathematically, it is described by an inhomogeneous Schrödinger equation,

$$(E - H_{\text{open}}) |\varphi\rangle = |s_L\rangle \,, \tag{2.13}$$

with

$$H_{\text{open}} = H_C - i\frac{\gamma_L}{2} - i\frac{\gamma_R}{2}, \tag{2.14}$$

as an effective hamiltonian describing the interaction of the isolated device C after connecting to the leads L and R.

We can find $|\varphi\rangle$ in terms of $|s_L\rangle$ by means of the Green function of the open C system

$$|\varphi\rangle = G(E) |s_L\rangle \,. \tag{2.15}$$

On the other hand, we will assume that the number of electronic charges crossing from the lead to the device is proportional to the rate of escape from the device to the electrode, and to the number of available states at the lead given by the Fermi-Dirac distribution, $f_L(E)$, i.e,

$$\| |s_L\rangle \|^2 = \gamma_L f_L(E). \tag{2.16}$$

This expression can be decomposed in terms of the elements of a base $\{|j\rangle\}$ as $|s_L\rangle = \sum_j |j\rangle \langle j|s_L\rangle$, and we obtain $\gamma_L f_L(E) = \langle s_L|s_L\rangle = \sum_j \langle j| (|s_L\rangle \langle s_L|) |j\rangle$. Here, we define an operator Γ_I in such a way that it satisfies the following,

$$\Gamma_L f_L(E) \equiv |s_L\rangle \langle s_L| \,, \tag{2.17}$$

and we can rewrite (2.16) as $\| |s_L\rangle \|^2 = \sum_j \langle j| (|s_L\rangle \langle s_L|) |j\rangle = \sum_j \langle j| \Gamma_L f_L(E) |j\rangle$.

The electronic density in the device is then $n = \langle \varphi|\varphi\rangle$, which can be written in terms of a base $|j\rangle$ of the device as

$$n = \sum_j \langle j| (|\varphi\rangle \langle \varphi|) |j\rangle \,. \tag{2.18}$$

We can rewrite the last expression by using the result (2.15) to show that $n = \sum_j \langle j| \left(G |s_L\rangle \langle s_L| G^\dagger\right) |j\rangle$. Also, by means of eq.(2.17), it can demonstrated that $n = \sum_j \langle j| \left(G\Gamma_L f_L G^\dagger\right) |j\rangle = \mathrm{Tr}(G\Gamma_L G^\dagger) f_L$. The contribution from both leads result in

$$n = \mathrm{Tr}(G\Gamma_L G^\dagger) f_L + \mathrm{Tr}(G\Gamma_R G^\dagger) f_R \tag{2.19}$$

Here, $G^n(\equiv -iG^<) = |\phi_C\rangle \langle\phi_C|$ is the correlation function whose diagonal elements are the electron density n[62]. The mean value measured at the device, at the state $|i\rangle$, is $\langle i| G^n |i\rangle$ and hence we can understand (2.18) as the mean total density in the device, $n = \mathrm{Tr}(G^n)$. Then, according from (2.19), G^n can also be written as

$$G^n = G\mathit{\Gamma}_L G^\dagger f_L + G\mathit{\Gamma}_R G^\dagger f_R \tag{2.20}$$

It is well known that the Fermi-Dirac distribution, $f(E)$, gives the probability of finding an electron with energy E. The number of available states, per unit of energy is then[64]

$$A = G\mathit{\Gamma}_L G^\dagger + G\mathit{\Gamma}_R G^\dagger \tag{2.21}$$

or written in a more reduced way if we define $\mathit{\Gamma} \equiv \mathit{\Gamma}_L + \mathit{\Gamma}_R$,

$$A = G\mathit{\Gamma} G^\dagger \tag{2.22}$$

2.2.1.1 Device with many energy levels: general case

Now we consider a pair of semi-infinite leads (L and R) connected to a device C. The device is characterized by a discrete energy spectrum, and is big enough so that interactions between leads can be neglected. If $\hat{H}_i$ ($i = L, C, R$) represents the hamiltonian for the isolated L, R and C systems, and $\hat{V}_{ij}$ represents the interaction between a lead and the device, then the hamiltonian reads

$$H = \hat{H}_L + \hat{H}_C + \hat{H}_D + \hat{V}_{LC} + \hat{V}_{LC}^\dagger + \hat{V}_{CD} + \hat{V}_{CD}^\dagger. \tag{2.23}$$

The Schrödinger equation for the complete system can also be written in a matrix form,

$$\begin{pmatrix} \hat{H}_L & \hat{V}_{LC} & 0 \\ \hat{V}_{LC}^\dagger & \hat{H}_C & \hat{V}_{RC}^\dagger \\ 0 & \hat{V}_{RC} & \hat{H}_R \end{pmatrix} \begin{pmatrix} |\phi_L\rangle \\ |\phi_C\rangle \\ |\phi_R\rangle \end{pmatrix} = E \begin{pmatrix} |\phi_L\rangle \\ |\phi_C\rangle \\ |\phi_R\rangle \end{pmatrix}, \tag{2.24}$$

where $|\phi_{L,C,R}\rangle$ are the components of the eigenfunction at the L, C and R subsystems. From the last expression, an equation for the central device can be obtained (see Ref.[65])

$$\left(E - \hat{H}_C - \hat{\Sigma}_L - \hat{\Sigma}_R\right)|\phi_C\rangle = 0, \tag{2.25}$$

where

$$\begin{aligned} \hat{\Sigma}_L &\equiv \hat{V}^\dagger_{LC} g_L \hat{V}_{LC}, \\ \hat{\Sigma}_R &\equiv \hat{V}^\dagger_{RC} g_R \hat{V}_{RC}, \end{aligned} \tag{2.26}$$

and $g_i(E) = (E - \hat{H}_i)^{-1}$, $(i = L, C, R)$ are the Green functions of the isolated subsystems L, C, or R.

The last result can be interpreted as a system with an open hamiltonian $H_{\text{open}} = H_C + \hat{\Sigma}_L + \hat{\Sigma}_R$ describing the central device interacting with right and left leads through the non-hermitian self-energies matrices $\hat{\Sigma}_{L(R)}$(see ref.[66]). Similar to the imaginary part of the hamiltonian for the one energy level device example in 2.14, the imaginary part of the self-energies operators,

$$\hat{\Gamma} = 2\text{Im}(\hat{\Sigma}) = i(\hat{\Sigma} - \hat{\Sigma}^\dagger), \tag{2.27}$$

confers a mean lifetime to electrons in the device, leading to an electronic decay rate in the device and an electronic escape rate from the device to the electrodes.

Expression 2.25 can be directly related to the Green function of the device interacting with the electrodes as

$$G_C^{-1}(E) = g_C^{-1}(E) - \hat{\Sigma}_L - \hat{\Sigma}_R, \tag{2.28}$$

where $g_C^{-1}(E) = E - H_C$ is the Green function of the isolated device. From here, it can be demonstrated that

$$G_C = g_C + g_C \hat{\Sigma}_L G_C + g_C \hat{\Sigma}_R G_C, \tag{2.29}$$

or write the following expression in terms of the interactions:

$$G_C = g_C + g_C \hat{V}^\dagger_{LC} g_L \hat{V}_{LC} G_C + g_C \hat{V}^\dagger_{RC} g_R \hat{V}_{RC} G_C. \tag{2.30}$$

Considering the interaction as hermitic operators ($V^\dagger_{LC} = V_{CL}$ and $V^\dagger_{RC} = V_{CR}$), we arrive at Dyson's equation[65]

$$\begin{aligned} G_C &= g_C + g_C V_{CL} G_{LC} + g_C V_{CR} G_{RC}, \\ G_{LC} &= g_L \hat{V}_{LC} G_C, \\ G_{RC} &= g_R \hat{V}_{RC} G_C. \end{aligned} \tag{2.31}$$

From 2.29, it is straightforth to demonstrate $(G_C^\dagger)^{-1} - G_C^{-1} = \hat{\Sigma} + \hat{\Sigma}^\dagger$ (using the definition $\Sigma \equiv \Sigma_L + \Sigma_R$). From the last expression, we identify Γ according to 2.27, so we have $(G_C^\dagger)^{-1} - G_C^{-1} = \Gamma$, from which we can demonstrate $G_C - G_C^\dagger = -iG_C \Gamma G_C^\dagger$. Hence, the spectral function from 2.22, $A = G_C \mathit{\Gamma} G_C^\dagger$, is expressed just in terms of G_C,

$$A = i(G_C - G_C^\dagger). \tag{2.32}$$

Current through the device In the Landauer approximation, we consider the stationary state where the electronic charge in the device does not change in time, and it is mathematically written in terms of G^n as

$$0 = \frac{d}{dt}\hat{G}^n = \frac{i}{\hbar}\left[\hat{H}, \hat{G}^n\right], \tag{2.33}$$

and because the particle density is given by the trace of G^n, the current will be given by its temporal derivative. So, we calculate the trace for the two terms at the right side of the last equation, $\text{Tr}(\frac{dG^n}{dt}) = \frac{i}{h}(\text{Tr}(HG^n) - \text{Tr}(G^n H))$. And we can rewrite it by means of the definition $G^n \equiv |\phi_C\rangle \langle\phi_C|$ as

$$\text{Tr}\left(\frac{dG^n}{dt}\right) = \frac{i}{h}\sum_j \Big(\langle j| \left(|H\phi_C\rangle\right) \langle\phi_C|j\rangle - \langle j|\phi_C\rangle \left(H\,|\phi_C\rangle\right)^\dagger |j\rangle\Big), \tag{2.34}$$

where we have considered $\langle\phi_C|\,H = (H\,|\phi_C\rangle)^\dagger$. Here we can substitute $H = H_{\text{open}} \equiv H_C + \mathit{\Sigma}_L + \mathit{\Sigma}_R$ and sum over the states $|j\rangle$ to arrive at

$$= \frac{i}{h}\Big(\langle\phi_C|H_C + \mathit{\Sigma}_L + \mathit{\Sigma}_R|\phi_C\rangle - \Big\langle\phi_C|H_C + \mathit{\Sigma}_L^\dagger + \mathit{\Sigma}_R^\dagger|\phi_C\Big\rangle\Big), \tag{2.35}$$

and because H_C is hermitic, the expression reduces to

$$= \frac{i}{h}\Big(\Big\langle\phi_C|\Sigma_L - \Sigma_L^\dagger|\phi_C\Big\rangle - \Big\langle\phi_C|\Sigma_R - \Sigma_R^\dagger|\phi_C\Big\rangle\Big). \tag{2.36}$$

By using the definition $\Gamma_{L(R)} \equiv i\left(\Sigma_{L(R)} - \Sigma^{\dagger}_{L(R)}\right)$, (2.33) takes the following form

$$0 = \frac{d}{dt}\hat{G}^{n} = \frac{i}{h}\left(\langle \phi_C | \mathit{\Gamma}_L | \phi_C \rangle - \langle \phi_C | \mathit{\Gamma}_R | \phi_C \rangle\right). \tag{2.37}$$

Here, we identify the first (second) term at the right as the variation of charge through the left (right) lead. Then, the electric current trough the right contact is

$$I_R = \frac{e}{h}\langle \phi_C | \mathit{\Gamma}_R | \phi_C \rangle . \tag{2.38}$$

On the other hand, it can be shown[65] that a perturbation $\left|\psi_n^{\text{left}}\right\rangle$ (n stands for the transverse states, transverse to the current $L - C - R$), coming from the left lead, causes a response from the entire system $L \oplus C \oplus R$ with solutions at each subsystem in terms of the perturbation as follows,

$$|\phi_C\rangle = G_C V^{\dagger}_{LC}\left|\psi_n^{\text{left}}\right\rangle , \tag{2.39}$$

$$|\phi_R\rangle = g_R V_{CR} G_C V^{\dagger}_{LC}\left|\psi_n^{\text{left}}\right\rangle , \tag{2.40}$$

$$|\phi_L\rangle = \left(\hat{1} + g_L V_{LC} G_C V^{\dagger}_{LC}\right)\left|\psi_n^{\text{left}}\right\rangle . \tag{2.41}$$

Here, $\left|\psi_n^{\text{left}}\right\rangle$ is interpreted as the stationary state of the **isolated** L-electrode before being connected to the device C, and reflected totally in one of its ends. When connected to the device, it is generated a response in itself (as noted by (2.41) where $\widehat{1}$ and $g_L V_{LC} G_C V^{\dagger}_{LC}$ accounts for the initial perturbation, and the response when connecting to the device, respectively). It is also generated a response in C and R-electrode, as shown in (2.39) and (2.40). Substituting (2.39) in (2.38) we arrive to

$$I_R = \frac{e}{h}\left\langle \psi_n^{\text{left}} | V_{LC} G^{\dagger}_{C} \mathit{\Gamma}_R G_C V^{\dagger}_{LC} | \psi_n^{\text{left}} \right\rangle . \tag{2.42}$$

We integrate in energy to obtain the total current

$$I_R = \frac{e}{h}\int dE \cdot f_L(E) \sum_n \delta(E - E_n)\left\langle \psi_n^{\text{left}} | V_{LC} G^{\dagger}_{C} \mathit{\Gamma}_R G_C V^{\dagger}_{LC} | \psi_n^{\text{left}} \right\rangle . \tag{2.43}$$

Expanding over sates $|j\rangle$ and then summing up the contributions from the transverse modes allow us rewrite the last expression as

$$I_R = \frac{e}{h}\int dE \cdot f_L(E) \sum_n \delta(E-E_n) \sum_j \left\langle \psi_n^{\text{left}} | V_{LC} \left| j \right\rangle \left\langle j \right| G_C^\dagger \mathit{\Gamma}_R G_C V_{LC}^\dagger | \psi_n^{\text{left}} \right\rangle , \tag{2.44}$$

$$I_R = \frac{e}{h}\int dE \cdot f_L(E) \sum_j \left\langle j \right| G_C^\dagger \mathit{\Gamma}_R G_C V_{LC}^\dagger \sum_n \left(\left| \psi_n^{\text{left}} \right\rangle \delta(E-E_n) \left\langle \psi_n^{\text{left}} \right| \right) V_{LC} \left| j \right\rangle . \tag{2.45}$$

In the last expression, we can recognize the term in parenthesis as the density of states for the L-electrode, A_L. Then, we gain a factor $V_{LC}^\dagger A_L V_{LC}$ that can be rewritten in terms of the Green function of L if we use 2.32: $A_L = i(G_L - G_L^\dagger)$. So, we find $V_{LC}^\dagger A_L V_{LC} = i(V_{LC}^\dagger G_L V_{LC} - V_{LC}^\dagger G_L^\dagger V_{LC})$, and by means of (2.26) we show that $V_{LC}^\dagger A_L V_{LC} = i(\mathit{\Sigma}_L - \mathit{\Sigma}_L^\dagger) = \mathit{\Gamma}_L$. Therefore, (2.45) becomes

$$I_R = \frac{e}{h}\int dE \cdot f_L(E) \sum_j \left\langle j \right| G_C^\dagger \mathit{\Gamma}_R G_C \mathit{\Gamma}_L \left| j \right\rangle = \frac{e}{h}\int dE \cdot \mathrm{Tr}\left(G_C^\dagger \mathit{\Gamma}_R G_C \mathit{\Gamma}_L \right) f_L(E), \tag{2.46}$$

where we use the convention that the current is measured from the leads to the device.

Finally, perturbations from the left and right electrode would give a net current given by the Landauer formula

$$I_R = \frac{e}{h}\int dE \cdot \mathrm{Tr}\left(G_C^\dagger \mathit{\Gamma}_R G_C \mathit{\Gamma}_L \right)(f_L(E) - f_R(E)), \tag{2.47}$$

with a Transmission function as

$$T(E) = \mathrm{Tr}\left(G_C^\dagger \mathit{\Gamma}_R G_C \mathit{\Gamma}_L \right) = \mathrm{Tr}\left(G_C \mathit{\Gamma}_L G_C^\dagger \mathit{\Gamma}_D \right) . \tag{2.48}$$

2.3 Recursive Green function renormalization

Dyson's equation allow us to find the electronic structure of nanoribbons directly from the Green functions. According to 2.31, the Green function of an arrangement of atomic sites can be calculated in terms of the Green function of the isolated sites[67]

$$\mathscr{G}_{i,j}(E) = \delta_{i,j}\mathcal{G}_i(E) + \mathcal{G}_i(E) \sum_l T_{i,l} \mathscr{G}_{l,j}(E) . \tag{2.49}$$

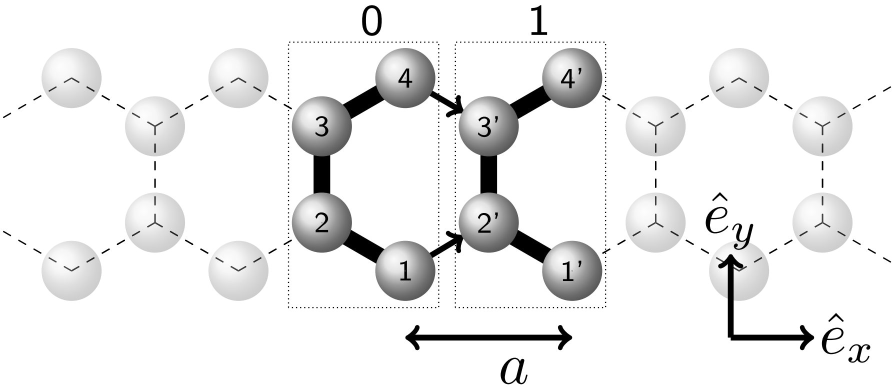

Figure 2.2: The unit cell of a 2-ZGNR. The “cell” 0 is connected to its neighbor “cell” 1 through the transfer matrix $T_{0,1}$.

Here $T_{i,l}$ represents the hopping matrix between cell i and cell l, and $\mathcal{G}_i$ is a diagonal matrix whose elements are the Green functions of each isolated m-th site in the periodic unit cell, $\mathrm{g}^{(\mathrm{m})}(E) = (E - \varepsilon_m + i\eta)^{-1}$, where ε_m is the on-site energy at the m-site, and $\eta \to 0^+$. Fig.2.2 shows the unit cell and its neighbors for a 2-ZGNR. For this system, the Green function matrices of a set of isolated sites in the unit cell, the interaction between the sites inside the unit cell, and the hopping matrices between the unit cell and its neighbors for a 2-ZGNR (2 zigzag chains and4 atoms in the unit cell) are, respectively, given by $\mathcal{G}_0$, $T_{0,0}$, and $T_{0,1}$ as,

$$\mathcal{G}_0 = \begin{pmatrix} \mathrm{g}^{(1)} & 0 & 0 & 0 \\ 0 & \mathrm{g}^{(2)} & 0 & 0 \\ 0 & 0 & \mathrm{g}^{(3)} & 0 \\ 0 & 0 & 0 & \mathrm{g}^{(4)} \end{pmatrix} \qquad T_{0,0} = \begin{pmatrix} 0 & t & 0 & 0 \\ t & 0 & t & 0 \\ 0 & t & 0 & t \\ 0 & 0 & t & 0 \end{pmatrix} \qquad T_{0,1} = T^{\dagger}_{0,\bar{1}} = \begin{pmatrix} 0 & t & 0 & 0 \\ 0 & 0 & 0 & 0 \\ 0 & 0 & 0 & 0 \\ 0 & 0 & t & 0 \end{pmatrix}, \tag{2.50}$$

with t being the hopping energy between two first neighbor atoms, taken as a constant.

Having built the hopping matrices and Green functions of the isolated unit cell, we can find the Green function of the unit cell open to their infinite neighbors by using the Dyson's equation in a recursive procedure. This process is a renormalization scheme by which the unit cell transforms into an equivalent system keeping the original structure, conserving the translational symmetry, and decreasing the strength of the hopping matrices compared with the original system. It is a iterative process by which the transfer matrices tend to zero in the limit of infinite iterations. To illustrate this process let's take the Dyson's equation considering interactions between first neighbors sites:

$$
\begin{aligned}
\mathscr{G}_{00} &= \mathcal{G}_0 + \mathcal{G}_0\hat{T}_{00}\mathscr{G}_{00} + \mathcal{G}_0\hat{T}_{01}\mathscr{G}_{10} + \mathcal{G}_0\hat{T}_{0\bar{1}}\mathscr{G}_{\bar{1}0} \\
\mathscr{G}_{00} &= \mathcal{G}_R^{(0)}\left[1 + \hat{T}\mathscr{G}_{10} + \hat{T}^{\dagger}\mathscr{G}_{\bar{1}0}\right]
\end{aligned}
\tag{2.51}
$$

where we have defined $\mathcal{G}_R^{(0)} \equiv \left\{[1 - \mathcal{G}_0\hat{T}_{00}]^{-1}\mathcal{G}_0\right\}$ and $\hat{T} = \hat{T}_{0,1}$. For ZGNRs, it can be shown that $\hat{T}_{0,\bar{1}} = \hat{T}^{\dagger}$. Now we use again Dyson's equation to find $\mathscr{G}_{\bar{1}0}$ e $\mathscr{G}_{10}$,

$$
\mathscr{G}_{\bar{1}0} = \mathcal{G}_{\bar{1}}\hat{T}_{\bar{1}0}\mathscr{G}_{00} + \mathcal{G}_{\bar{1}}\hat{T}_{\bar{1}\bar{1}}\mathscr{G}_{\bar{1}0} + \mathcal{G}_{\bar{1}}\hat{T}_{\bar{1}\bar{2}}\mathscr{G}_{\bar{2}0} \;\rightarrow\; \mathscr{G}_{\bar{1}0} = \mathcal{G}_R^{(0)}\left[\hat{T}\mathscr{G}_{00} + \hat{T}^{\dagger}\mathscr{G}_{\bar{2}0}\right], \tag{2.52}
$$

$$
\mathscr{G}_{10} = \mathcal{G}_{1}\hat{T}_{10}\mathscr{G}_{00} + \mathcal{G}_{1}\hat{T}_{11}\mathscr{G}_{10} + \mathcal{G}_{1}\hat{T}_{12}\mathscr{G}_{20} \;\rightarrow\; \mathscr{G}_{10} = \mathcal{G}_R^{(0)}\left[\hat{T}^{\dagger}\mathscr{G}_{00} + \hat{T}\mathscr{G}_{20}\right], \tag{2.53}
$$

where we have used the fact that $\mathcal{G}_R^{(\bar{1})} \equiv \left\{[1 - \mathcal{G}_{\bar{1}}\hat{T}_{\bar{1}\bar{1}}]^{-1}\mathcal{G}_{\bar{1}}\right\} = \mathcal{G}_R^{(0)}$.

Then 2.51 becomes:

$$
\mathscr{G}_{00} = \mathcal{G}_R^{(1)}\left[1 + \hat{T}^{(1)}\mathscr{G}_{20} + \hat{T}_D^{(1)}\mathscr{G}_{\bar{2}0}\right] , \tag{2.54}
$$

where

$$
\mathcal{G}_R^{(1)} = \left[1 - ZZ_D - Z_D Z\right]^{-1}\mathcal{G}_R^{(0)} , \tag{2.55}
$$

$$
Z = \mathcal{G}_R^{(0)}T , \quad Z_D = \mathcal{G}_R^{(0)}T^{\dagger} , \quad \hat{T}^{(1)} = T\mathcal{G}_R^{(0)}T , \quad \hat{T}_D^{(1)} = T^{\dagger}\mathcal{G}_R^{(0)}T^{\dagger} . \tag{2.56}
$$

The last result shows that the original system may be replaced by its equivalent, with its renormalized Green function $\mathcal{G}_R^{(1)}$, and hopping $\hat{T}^{(1)}$, refering to the sites $\bar{2}, 0, 2$ instead of the original equation 2.51 where it refers to sites $\bar{1}, 0, 1$. This process allows us to find a recursive result:

$$
\mathcal{G}_R^{(N)} = \left[1 - Z^{(N-1)}Z_D^{(N-1)} - Z_D^{(N-1)}Z^{(N-1)}\right]^{-1}\mathcal{G}_R^{(N-1)} , \tag{2.57}
$$

where

$$\begin{aligned}
Z^{(N-1)} &= \mathcal{G}_R^{(N-1)} T^{(N-1)} \ , \\
Z_D^{(N-1)} &= \mathcal{G}_R^{(N-1)} T_D^{(N-1)} \ , \\
\hat{T}^{(N)} &= T^{(N-1)} \mathcal{G}_R^{(N-1)} T^{(N-1)} \ , \\
\hat{T}_D^{(N)} &= T_D^{(N-1)} \mathcal{G}_R^{(N-1)} T_D^{(N-1)} \ ,
\end{aligned} \tag{2.58}$$

with initial conditions $T^{(0)} = T$; $T_D^{(0)} = T^\dagger$; $\mathcal{G}_R^{(0)} = \left\{ [1 - \mathcal{G}_0 \hat{T}_{00}]^{-1} \mathcal{G}_0 \right\}$.

The cells of the equivalent system are expected to be very far from each other in the limit $N \to \infty$, and hence the hopping between neighbor cells would tend to zero, $\lim_{N \to 0} T^{(N)} = 0$. In this limit the final Green function of the system is the renormalized Green function $\mathcal{G}_R^{(N)}$, within an error defined by $\left| \mathcal{G}_R^{(N)} - \mathcal{G}_R^{(N-1)} \right| \ll \delta$, with δ being a small number (of the order of $10^{-4}\eta$).

2.4 Band structure calculation

The electronic band structures of the systems treated in this thesis show how we calculate the electronic band structures and the localization of the electronic states. As some calculahave been calculated from the eigenvalues of the corresponding hamiltonian H. For all the studied nanosystems, we use the TB approximation to express the hamiltonian in a basis of single orbitals centered at each site (one p_z orbital per site). For the infinite and periodic nanoribbons, it is more convenient to work with the hamiltonian of the unit cell opened to semi-infinite electrodes. The same N-atom unit cell is repeated every a units in the x-direction, as shown in Fig.2.2. Mathematically, if $T_{\vec{a}}$ is the translation operator along the vector $\vec{a} = a\hat{e}_x$, then the eigenvector $\Psi_k(\vec{r})$ of the hamiltonian satisfies $T_{\vec{a}} \Psi_k(\vec{r}) = e^{ika} \Psi_k(\vec{r})$. Finally, due to the periodic nature of our system, we can express the eigenvectors of H as a linear composition of Bloch waves $\chi_k(\vec{r})$,

$$\chi_k(\vec{r}) = \frac{1}{\sqrt{N}} \sum_{i=1}^{N} e^{ikr} \phi(\vec{r} - \vec{R}_i), \tag{2.59}$$

where $\phi(\vec{r} - \vec{R}_i)$ is a p_z orbital centered at the i-th site. From such considerations, we can show that the hamiltonian of the open system is a contribution of an isolated unit cell and its interaction with neighbor cells.

We call H_{00} the matrix form of the hamiltonian of a unit cell (cell '0' as shown in Fig.2.2) as if it was **isolated** from its neighboring cells

$$H_{00} = \left\langle \chi_k(\vec{r}) \left| \hat{H} \right| \chi_k(\vec{r}) \right\rangle = \left[H^{i,j}_{0,0} \right]_{N\times N} \quad , \tag{2.60}$$

with matrix elements $H^{i,i}_{0,0} = \varepsilon_i$ and $H^{i,j}_{0,0} = \frac{1}{\sqrt{N}} \int d\vec{r} \phi^*(\vec{r} - \vec{R}_i) \hat{H} \phi(\vec{r} - \vec{R}_j) \equiv t$ as the on-site energy value of the i-th site and the hopping integral between the i-th and$j$-th site, respectively.

The interaction between neighbor cells is given by

$$H_{01} = \left\langle \chi_k(\vec{r}) \left| \hat{H} \right| \chi_k(\vec{r} - \vec{a}) \right\rangle . \tag{2.61}$$

When written in terms of the orbital basis, it becomes

$$\begin{aligned} H^{ij}_{01} &= \frac{1}{\sqrt{N}} \int d\vec{r} e^{ikr} \phi^*(\vec{r} - \vec{R}_i) \hat{H} e^{-ik(r+a)} \phi(\vec{r} - \vec{R}_j - a\hat{e}_x), \\ H^{ij}_{01} &= \left[\frac{1}{\sqrt{N}} \int d\vec{r} e^{ika} \phi^*(\vec{r} - \vec{R}_i) \hat{H} \phi(\vec{r} - \vec{R}_j - a\hat{e}_x) \right] e^{ika} = \left[T^{i,j}_{0,1} \right]_{N\times N} e^{ika}, \end{aligned} \tag{2.62}$$

From this last equation, we see that H_{01} is a $N \times N$ matrix with only hopping integrals, between the i-th site of the '0'-cell and the j-th site of the '1'-cell. We can find a similar result for the interaction between the central cell and the cell at the left, $H_{0\bar{1}}$. Finally, we arrive at the following expression for the hamiltonian of the central cell interacting with its neighboring cells:

$$H(k) = H_{00} + T_{01} \exp(ika) + T_{0\bar{1}} \exp(-ika)$$

For a zigzag nanoribbon with 4 sites (see Fig.2.2), the hamiltonian takes the following form:

$$H(k) = \begin{pmatrix} \varepsilon_1 & t & 0 & 0 \\ t & \varepsilon_2 & t & 0 \\ 0 & t & \varepsilon_3 & t \\ 0 & 0 & t & \varepsilon_4 \end{pmatrix} + \begin{pmatrix} 0 & t & 0 & 0 \\ 0 & 0 & 0 & 0 \\ 0 & 0 & 0 & 0 \\ 0 & 0 & t & 0 \end{pmatrix} e^{ika} + \begin{pmatrix} 0 & 0 & 0 & 0 \\ t & 0 & 0 & 0 \\ 0 & 0 & 0 & t \\ 0 & 0 & 0 & 0 \end{pmatrix} e^{-ika}, \tag{2.63}$$

and can be simplified to

$$H(k) = \begin{pmatrix} \varepsilon_1 & tf_k & 0 & 0 \\ tf_k^* & \varepsilon_2 & t & 0 \\ 0 & t & \varepsilon_3 & tf_k \\ 0 & 0 & tf_k & \varepsilon_4 \end{pmatrix}, \tag{2.64}$$

where $f_k = 2\cos(ka/2)e^{ika/2}$.

For a zigzag nanoribbon with an N-atom unit cell, $H(k)$ adopts a particular shape when $ka = \pi$:

$$H(ka = \pi) = \begin{pmatrix} [\varepsilon_1] & 0 \quad 0 & & & 0 \\ \begin{matrix} 0 \\ 0 \end{matrix} & \begin{bmatrix} \varepsilon_2 & t \\ t & \varepsilon_3 \end{bmatrix} & \begin{matrix} 0 \\ 0 \end{matrix} & & \\ & 0 \quad 0 & \ddots & 0 \quad 0 & \\ & & \begin{matrix} 0 \\ 0 \end{matrix} & \begin{bmatrix} \varepsilon_{N-2} & t \\ t & \varepsilon_{N-1} \end{bmatrix} & \begin{matrix} 0 \\ 0 \end{matrix} \\ 0 & & & 0 \quad 0 & [\varepsilon_N] \end{pmatrix}, \tag{2.65}$$

i.e, the band structure of the zigzag nanoribbon shows two solutions at ε_1 and ε_N at $ka = \pi$. Also, the hamiltonian 2.65 leads to a pair of eigenvectors, localized either on the 1st site, or at the N-th site, i.e., at the edges of the zigzag nanoribbon. Consequently, by identifying the highest localized states of a zigzag nanoribbon in the correspondent band structure, we are able to estimate the on-site energy values at the edge atoms. Moreover, if he zigzag nanoribbons are made up of an alternated arrangement of just boron and nitrogen atoms, as in the case h-BN nanoribbons, then we can directly obtain their on-site energies by analyzing the localized states in the band structure.

2.4.1 Band structure localization

In a TB model, the H_k-eigenvectors (see hamiltonian at 2.64) can be expressed in terms of the orbitals centered at every i-th site, i.e. $\Psi_{nk}(\vec{r}) = \sum_{i=1}^{N} c_i \phi(\vec{r} - \vec{R}_i)$, where the probability amplitudes, c_i, must satisfy the normalization condition for the N-atom unit cell, $\sum_{i=1}^{N} |c_i|^2 = 1$. Here, we use the definition given by Zheng *et al*[13] which allows us to know the degree of electronic localization in the unit cell, given by a localization function ,

$$F \equiv \sum_{i=1}^{N} |c_i|^4, \tag{2.66}$$

which can be written in terms of A_c^{-2}, A_c being the area of the unit cell.

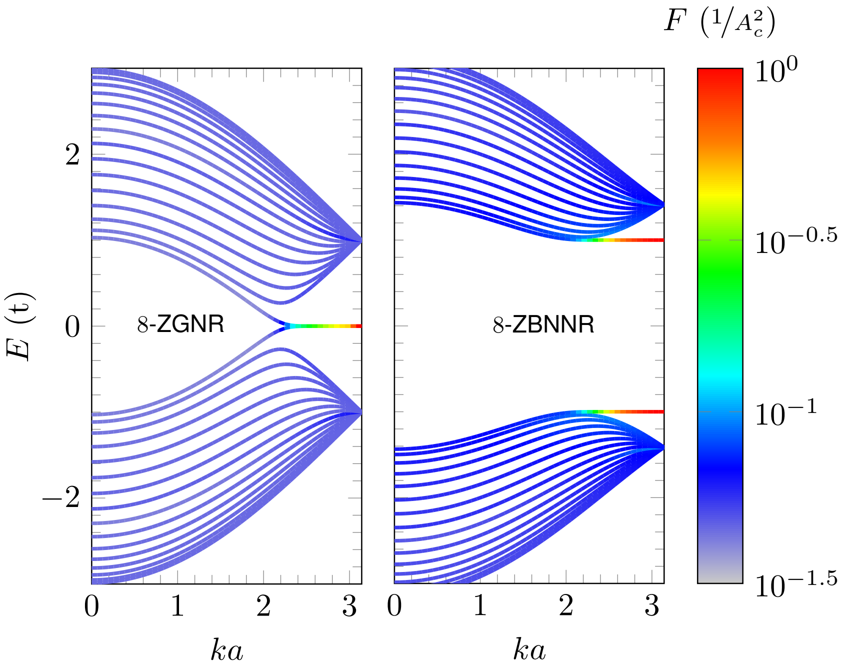

Figure 2.3: Band structure of a 8-ZGNR and a 8-ZBNNR in units of hopping energy, t, in a TB model. The on-site energy values for carbon, boron, and nitrogen atoms are 0, t, and $-t$, respectively. F gives localization, in color. The corresponding lattice parameter is a.

Therefore, by taking into account the normalization condition, we conclude that if the electron is localized at just one site of the unit cell, then $F = 1$. However, if it is equally distributed over the entire the N-atom unit cell, then $F = N\left(\frac{1}{\sqrt{N}}\right)^4 = \frac{1}{N}$, tending to zero for wider unit cells.

Flat bands localized at the zigzag edges (called *edge states*) happen due to the special geometry of the nanoribbons edges. In Fig.2.3, we can recognize such flat bands at which the parameter F is around 1 when $ka \to \pi$. In this limit, we can also find the on-site energy values at zigzag edge atoms. The examples show the band structures of a 8-ZGNR and a 8-ZBNNR (boron nitride nanoribbon) as calculated by TB hamiltonians and parameters described in the caption. The localization intensity is given by the color pattern defined in the Figure.

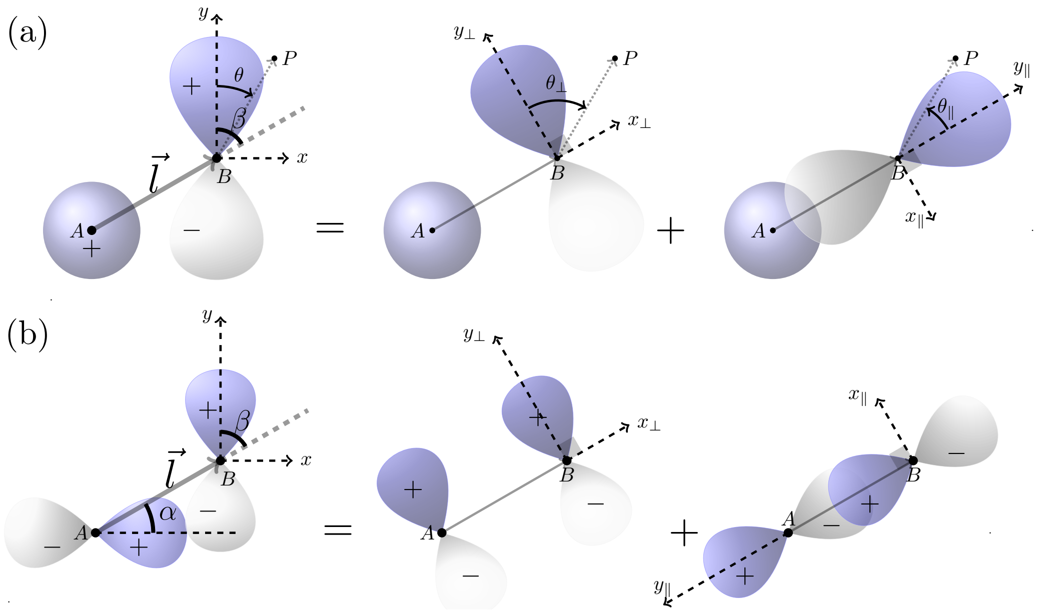

Figure 2.4: Orbitals decomposing and inter-atomic (a) s and p_y-orbital hybridization and (b) p_x and p_y-orbital hybridization. Atoms are centered at A and B.

2.5 Slater-Koster matrix

Consider a pair of carbon atoms, A and B, and their s-orbital and p_y-orbital interacting as illustrated in Fig.2.4(a). Depending on the crystal geometry where A and B are embedded, the p_y-orbital will be tilted at an angle β with respect to the line connecting atoms A and B. We are wondering about their interaction in terms of geometrical independent ones.

In Fig.2.4(a), we denote $\vec{l}$ as the vector going from nucleus B to a point where electronic density is measured at P, and is written as $\vec{l} = l\sin(\theta)\cos(\phi)\hat{x} + l\cos(\theta)\hat{y} + l\sin(\theta)\sin(\phi)\hat{z}$, in spherical coordinates. If the xy-coordinate system centered at B were rotated around the z-axis in such a way that its $y_\perp$-axis were perpendicular to $\vec{AB}$, then the angle rotated would be $\frac{\pi}{2} - \beta$. In this new $x_\perp y_\perp$-coordinate system, we have $\vec{l} = l\sin(\theta_\perp)\cos(\phi_\perp)\hat{x}_\perp + l\cos(\theta_\perp)\hat{y}_\perp + l\sin(\theta_\perp)\sin(\phi_\perp)\hat{z}$. Additionally, the unit vectors of the new system may be written in terms of the unit vectors of the xy-system and the rotation operator $\mathbf{R}$, as $\mathbf{R}(\frac{\pi}{2} - \beta)\hat{y} = \hat{y}_\perp$ and $\mathbf{R}(\frac{\pi}{2} - \beta)\hat{x} = \hat{x}_\perp$. If we calculate $\cos(\theta)$

$$\cos(\theta) = \frac{\hat{y}\cdot\vec{l}}{l} = \cos(\theta_\perp)\sin(\beta) + \sin(\theta_\perp)\cos(\phi_\perp)\cos(\beta). \tag{2.67}$$

Now consider a $x_\parallel y_\parallel$-coordinate system centered at B with its $y_\parallel$-axis parallel to $\vec{AB}$

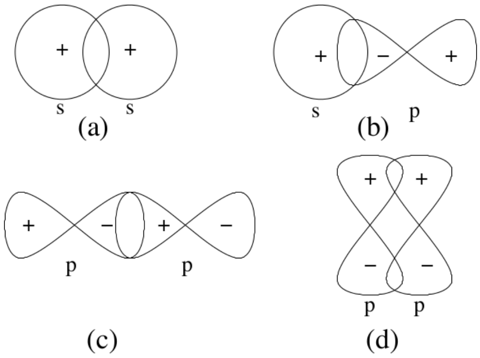

Figure 2.5: Basic hybridization energies for s-p bonds: (a)$V_{ss\sigma}$, (b)$V_{sp\sigma}$, (c) $V_{pp\sigma}$, (d)$V_{pp\pi}$. From reference [5].

(see Fig.2.4(a)). Here, the polar angle, $\theta_{\|}$, is measured from the $y_{\|}$-axis. Then, it can be shown that $\cos(\theta)$ from (2.67) becomes

$$\cos(\theta) = \cos(\theta_{\perp})\sin(\beta) + \cos(\theta_{\|})\cos(\beta). \tag{2.68}$$

Because the p_y-orbital depends on the polar angle θ as $\langle \vec{r}|p_y\rangle = R_p(r)\cos(\theta)$ (see reference [5]), then expression 2.68 tells us the lobe can be decomposed into the components parallel and perpendicular to the $y_{\perp}$-direction, as if it was a vector decomposition,

$$p_y = p_{y\perp}\sin(\beta) + p_{y\|}\cos(\beta). \tag{2.69}$$

The last result 2.68 allows us to express $s-p$ orbital interactions in a crystal in terms of four basic orbital interactions: $V_{ss\sigma}$, $V_{sp\sigma}$, $V_{pp\sigma}$ and $V_{pp\pi}$, as shown in Fig.2.5.

For our example in Fig.2.4(a), we can argue that

$$\left\langle s \middle| \hat{H} \middle| p_y \right\rangle = \left\langle s \middle| \hat{H} \middle| p_{y\perp} \right\rangle \sin(\beta) + \left\langle s \middle| \hat{H} \middle| p_{y\|} \right\rangle \cos(\beta). \tag{2.70}$$

It can be shown that $\left\langle s \middle| \hat{H} \middle| p_{y\perp} \right\rangle = 0$ due to symmetry arguments, and finally we have

$$\left\langle s \middle| \hat{H} \middle| p_y \right\rangle = V_{sp\sigma}\cos(\beta). \tag{2.71}$$

Now, take the hybridization between p_x and p_y-orbitals with the geometry shown in Fig.2.4(b). The orbitals can be decomposed as $p_x = -p_{x\perp}\sin(\alpha) - p_{x\|}\cos(\alpha)$, and $p_y = p_{y\perp}\sin(\beta) - p_{y\|}\cos(\beta)$. Then, the interaction between p_x and p_y orbitals is

$$\left\langle p_x \middle| \hat{H} \middle| p_y \right\rangle = -\left\langle p_{x\perp} \middle| \hat{H} \middle| p_{y\perp} \right\rangle \sin(\alpha)\sin(\beta) + \left\langle p_{x\parallel} \middle| \hat{H} \middle| p_{y\parallel} \right\rangle \cos(\alpha)\cos(\beta). \tag{2.72}$$

We can reduce this expression by noting that $c_x \equiv \hat{x}\cdot\vec{l}/l = \cos(\alpha)$, $c_y \equiv \hat{y}\cdot\vec{l}/l = \cos(\beta)$, and $c_z \equiv (z_B - z_A)/l$ are the directional cosines of $\vec{l}$ (going from atom A to atom B) with respect to the xy-coordinate system. By using the four basic orbital interactions (see Fig.2.5), we arrive to the following result,

$$\left\langle p_x \middle| \hat{H} \middle| p_y \right\rangle = (V_{pp\sigma} - V_{pp\pi})c_x c_y. \tag{2.73}$$

Following this methodology, we can build a hamiltonian for the interaction between atoms A and B in terms of the interaction between their atomic orbitals $2s$, $2p_z$, $2p_x$, $2p_y$:

$$h_{AB} = \begin{pmatrix} V_{ss\sigma} & V_{sp\sigma}c_z & V_{sp\sigma}c_x & V_{sp\sigma}c_y \\ -V_{sp\sigma}c_z & (V_{pp\sigma} - V_{pp\pi z})c_z^2 + V_{pp\pi z} & (V_{pp\sigma} - V_{pp\pi})c_z c_x & (V_{pp\sigma} - V_{pp\pi})c_z c_y \\ -V_{sp\sigma}c_x & (V_{pp\sigma} - V_{pp\pi})c_x c_z & (V_{pp\sigma} - V_{pp\pi})c_x^2 + V_{pp\pi} & (V_{pp\sigma} - V_{pp\pi})c_x c_y \\ -V_{sp\sigma}c_y & (V_{pp\sigma} - V_{pp\pi})c_y c_z & (V_{pp\sigma} - V_{pp\pi})c_y c_x & (V_{pp\sigma} - V_{pp\pi})c_y^2 + V_{pp\pi} \end{pmatrix}, \tag{2.74}$$

and from here, the Slater-Koster hamiltonian[68] is built for a pair of atoms as

$$H_{AB} = \begin{pmatrix} h_{AA} & h_{AB} \\ h_{AB}^{\dagger} & h_{BB} \end{pmatrix}. \tag{2.75}$$

where h_{AA}, h_{BB} are the on-site hamiltonians:

$$h_{AA} = h_{BB} = \begin{array}{c} \\ |s\rangle \\ |p_z\rangle \\ |p_x\rangle \\ |p_y\rangle \end{array} \begin{array}{c} \begin{array}{cccc} |s\rangle & |p_z\rangle & |p_x\rangle & |p_y\rangle \end{array} \\ \begin{pmatrix} \varepsilon_s & 0 & 0 & 0 \\ 0 & \varepsilon_p & 0 & 0 \\ 0 & 0 & \varepsilon_p & 0 \\ 0 & 0 & 0 & \varepsilon_p \end{pmatrix} \end{array} \tag{2.76}$$

2.6 DFT calculations

Density Functional Theory (DFT) approximates an interacting many-body problem to eletrons in an effective potential, leading to the Kohn-Sham equations[69],

$$-\frac{\hbar^2}{2m}\nabla^2\varphi_j + V_{eff}\varphi_j = \varepsilon_j\varphi_j, \tag{2.77}$$

where the density of the interacting system can be expressed in terms of an auxiliar and non-interacting system, that can be described by single-particle fictitious spin-orbitals, $\varphi_j(\vec{r})$,

$$n(\vec{r}) = \sum |\varphi_j(\vec{r})|, \tag{2.78}$$

and the non-interacting $\varphi_j(\vec{r})$ orbitals are immerse in the effective potential,

$$V_{eff} = \frac{1}{4\pi\varepsilon_0}\int d^3r'\frac{n(\vec{r})}{|\vec{r}-\vec{r}'|} + V_{ext} + \frac{\delta E_{xc}}{\delta n}, \tag{2.79}$$

where the first term refers to the Hartree potential, the second term represents the potential generated by the ions of the crystal, and the third term is the exchange and correlation potential. Until here, the theory is exact if v_{xc} was known. The usefulness of DFT calculations depends on finding simple and accurate exchange and correlation potentials.

In this thesis, we use DFT calculations to retrieve TB parameters in an approximate way. We also compare our TB results with DFT predictions. We use the Quantum ESPRESSO (QE) code[70] to perform DFT calculations.

Unless otherwised indicated, we perform spin-DFT calculations using the QE code with ultrasoft Vandelbirt pseudopotentials[71]. The cutoff energy of plane wave expansion is 30 Ry. We use a k-point sampling of 52 points over the one-dimensional Brillouin zone. We use a periodic set of ribbons separated by a vacuum of 12 Å to avoid spurious interactions. We used the same separation for nanoribbons in z-direction.

For the zigzag hybrid system, the unit cell is made up of an armchair chain of carbon atoms embedded in BN regions, with hydrogenated edges.

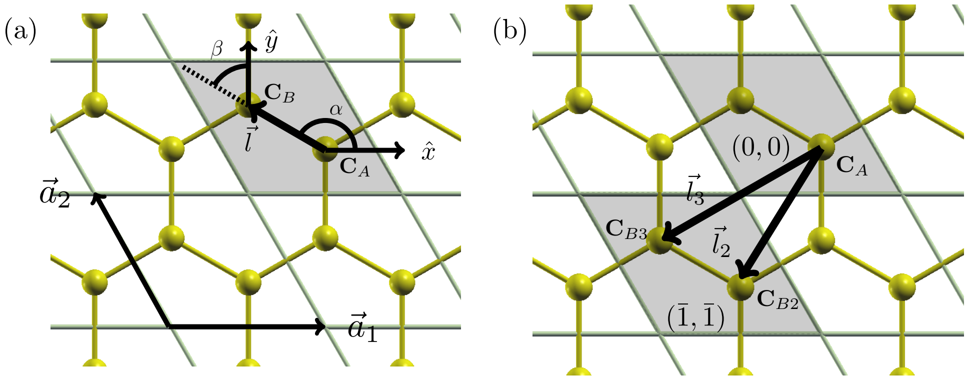

Figure 2.6: First **(a)**, second and third **(b)** carbon interactions in a graphene sheet. The interaction can also be expressed in terms of real unit cells defined by the crystal vectors $\vec{a}_1$, $\vec{a}_2$ as $(0,0)$, and $(\bar{1},\bar{1})$.

2.7 Fitting TB parameters from QE/WanT

We also use the WanT code [72, 73] as post-processing DFT calculations to project the Khon-Sham solutions into localized atomic orbitals, in an attempt to estimate hopping and on-site energy values, useful for our TB model. Here we describe the fitting process for a graphene sheet.

Quantum Espresso defines a trigonal lattice as shown in Fig.(2.6). The matrix h_{AB} written in (2.74) takes the following form ($c_x = \hat{x}\cdot\vec{l}/l = \cos(5\pi/6)$, $c_y = \hat{y}\cdot\vec{l}/l = \cos(\pi/3)$),

$$h_{AB} = \begin{pmatrix} V_{ss\sigma} & 0 & -\frac{\sqrt{3}}{2}V_{sp\sigma} & \frac{1}{2}V_{sp\sigma} \\ 0 & V_{pp\pi z} & 0 & 0 \\ \frac{\sqrt{3}}{2}V_{sp\sigma} & 0 & \frac{3}{4}V_{pp\sigma} + \frac{1}{4}V_{pp\pi} & -\frac{\sqrt{3}}{4}(V_{pp\sigma} - V_{pp\pi}) \\ -\frac{1}{2}V_{sp\sigma} & 0 & -\frac{\sqrt{3}}{4}(V_{pp\sigma} - V_{pp\pi}) & \frac{1}{4}V_{pp\sigma} + \frac{3}{4}V_{pp\pi} \end{pmatrix} = \begin{pmatrix} -3.14 & 0.00 & -3.40 & 1.97 \\ 0.00 & -2.10 & 0.00 & 0.00 \\ -3.40 & 0.00 & 1.76 & -1.80 \\ 1.97 & 0.00 & -1.80 & -0.33 \end{pmatrix}, \tag{2.80}$$

and can be compared to the first-neighbor hamiltonian from WanT, shown at the right side of the last expression. The last matrix refers to a particular pair of sites (first neighbors), but Want provides effective hamiltonians for every pair of sites in the unit cell. From here, the hopping and on-site energy values can be estimated, and are exposed in Table (2.1). The calculation displayed Eq.2.80 can be repeated to find hopping values for the next first neighbors. In Fig.2.7(a) we show the TB band structure using up to 5-first-neighbor hopping values with very good agreement to the DFT band strucutre. However, when considering just the first-neighbor interaction, the band structure departs

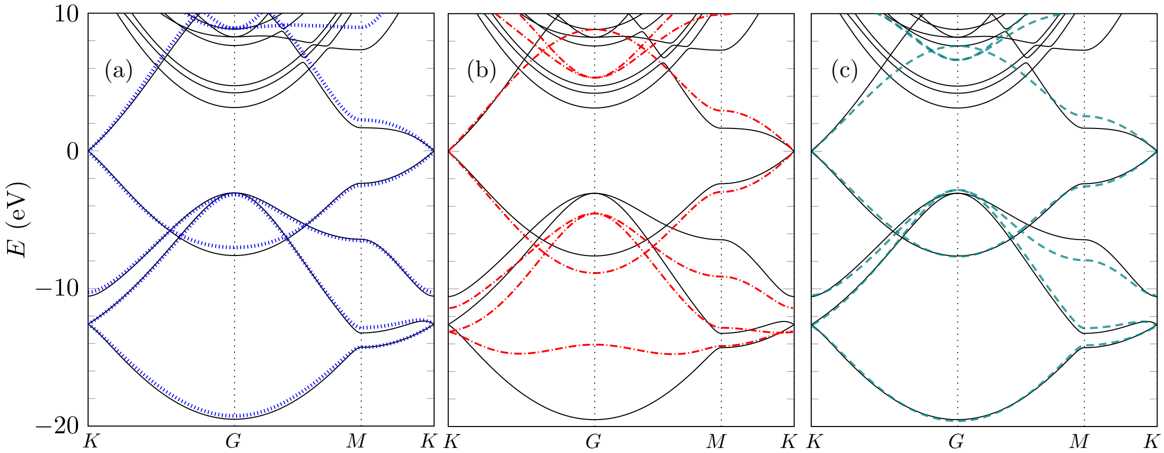

Figure 2.7: Black lines indicate DFT graphene band structure; and colored lines correspond to TB calculations. Band structure diagram using **(a)** 5 first nearest neighbors from WanT, **(b)** first neighbors hoppings from WanT, and **(c)** an optimal set of fitted hopping values, in blue, red, and green dashed lines, respectively.

from DFT results, as displayed in Fig.2.7(b). By adjusting the first-neighbor hoppings, we are able an optimal set of Slater-Koster parameter values that best match the DFT band structure, and the result is exhibited in Fig.2.7(c). The Slater-Koster parameters for first-neighbor interactions are presented in Table (2.1).

eV units	Ref.[74]	Ref.[75]	QE/WanT	fit
ε_s	-7.30	-8.8	-0.82	-3.40
ε_{px}	0.00	0.0	0.41	1.91
ε_{py}	0.00	0.0	0.41	1.91
ε_{pz}	0.00	0.0	0.00	0.00
$V_{ss\sigma}$	-4.30	-7.76	-3.14	-5.40
$V_{sp\sigma}$	4.98	8.16	3.93	5.48
$V_{pp\sigma}$	6.38	7.48	2.80	5.70
$V_{pp\pi}$	-2.66	-3.59	-1.37	-2.55
$V_{pp\pi z}$	-2.66	-3.59	-2.10	-2.55

Table 2.1: SK parameter values for a graphene sheet.

3

Graphene and h-BN lattice nanoribbons

3.1 Graphene

Graphene is a planar structure of carbon atoms disposed in a hexagonal mesh, bonded by strong covalent bonds. Graphene, as a 2D structure, was believed to be thermodynamically unstable, and thus the planar mesh would return back to its 3D structure[76]. However, in 2004, Geim and Novoselov were able to obtain high quality samples of graphene by repeatedly peeling up graphite crystals with scotch adhesive tapes. The samples revealed high quality graphene sheets in normal conditions[24]. This achievement gave rise to a plethora of studies not only in fundamental physics research, but also in a quest for its technological applications. Graphene production also opens the way to the study of other non-carbon 2D materials useful for nanoelectronics applications, such as Si, Ge, ZnO, and h-BN[77]. Yet, studies have focused on graphene due to the peculiar behavior of electrons in a honeycomb arrangement, that can be used as a small laboratory for quantum electrodynamics research, which usually requires big and costly equipment. Additionally, graphene offers possible applications for its use in transistors, integral circuitry, and hydrogen storage. Doped graphene also promises future devices such as gas sensors and photo-detectors.

Graphene research begins with the study of other carbon allotropes with hexagonal lattice such as graphite, carbon nanotubes and fullerenes. We remark the Wallace's theoretical work [78], showing that the conduction and valence bands of a graphite layer shows a degenerate state at the vertices of the first Brillouin zone of the hexagonal lattice, giving rise to subsequent studies on graphite [79, 80]. Later in 1985, H. Kroto found strange carbon spectral lines coming from giant red stars, discovering in following studies that it was the very fingerprint of carbon clusters, “fullerenes”, synthesized at laboratory[81]. In 1991, unique properties of carbon nanotubes attracted the attention of the scientific community after they were obtained in arc discharges[82], the same method to obtain fullerenes. Finally, the mechanical exfoliation procedure allowed the isolation of a unique graphene sheet in 2004[24]. However, at that time, the procedure used optical interference to recognize one single graphene sheet from other members of packing layers, limiting its industrial production at large scales, what have restricted its practical application. Nevertheless, efforts to obtain big graphene layers include beam molecular method, chemical vapor deposition (CVD) technique, among others. For example, a $\sim 60\,\mathrm{cm} \times 60\,\mathrm{cm}$ graphene sheet has been obtained with the CVD technique[83, 84]. However, the fabricated samples show regions with several layers, affecting graphene application as an electric conductor.

Because electrons in the ultimate atomic layer are weakly bonded to its nucleus, they are much more influenced by the presence of other carbon atoms in graphene. The electronic interaction when forming a honeycomb lattice is in such a way that electrons occupy new states in order to minimize the total energy of the graphene sheet. These new states are called hybridized orbitals, sp^2, and result from a linear combination of the carbon atomic orbitals $2s$, $2p_x$, and $2p_y$. The sp^2 orbitals join a carbon atom to its three neighbors. On the other hand, the $2p_z$ atomic orbitals do not hybridize and are responsible for the peculiar properties of graphene. Also, the electronic interactions between $2p_z$ orbitals through the sheet determines whether the system is planar or not. This is the case of Ge and Si for which the weaker interaction between $2p_z$ orbitals in their honeycomb lattices does not allow a planar structure[85].

Graphene can be modeled by the Tight Binding (TB) approximation. Even though the TB model was conceived to explain systems where electrons are highly localized around their nucleus, it also explains some systems with delocalized electrons, such as π-bands in graphene, reproducing the main features of more sophisticated models such as first principle calculations.

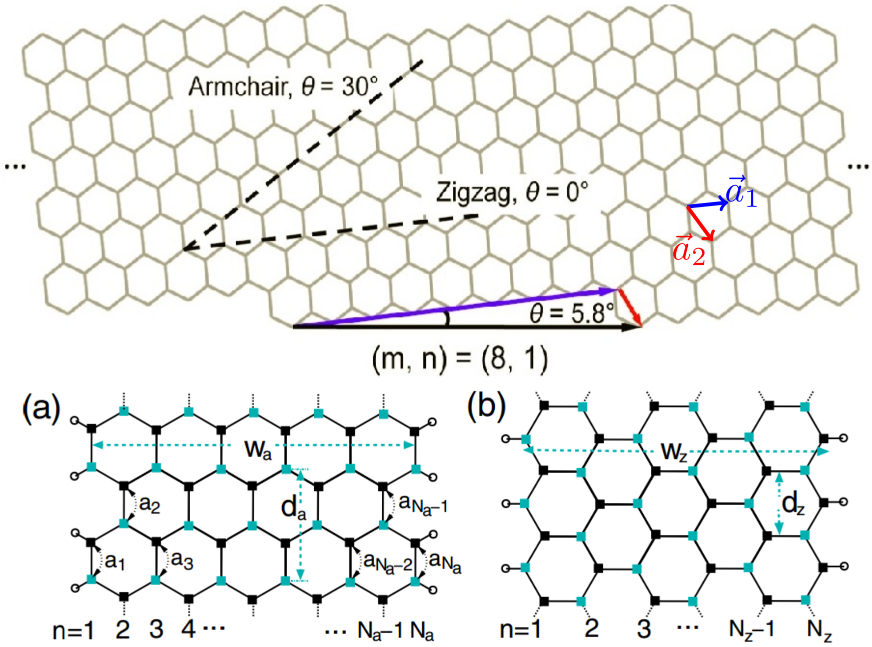

Figure 3.1: Top: Chiral nanoribbon with index $(m,n) = (8{,}1)$. A zigzag (armchair) nanoribbon is obtained by cutting along the dashed line $\theta = 0^{\text{o}}$ ($\theta = 30^{\text{o}}$). Bottom: hydrogenated 11-AGNR and a 6-ZGNR, with edges parallel to the vertical direction. Taken from Ref.[6]

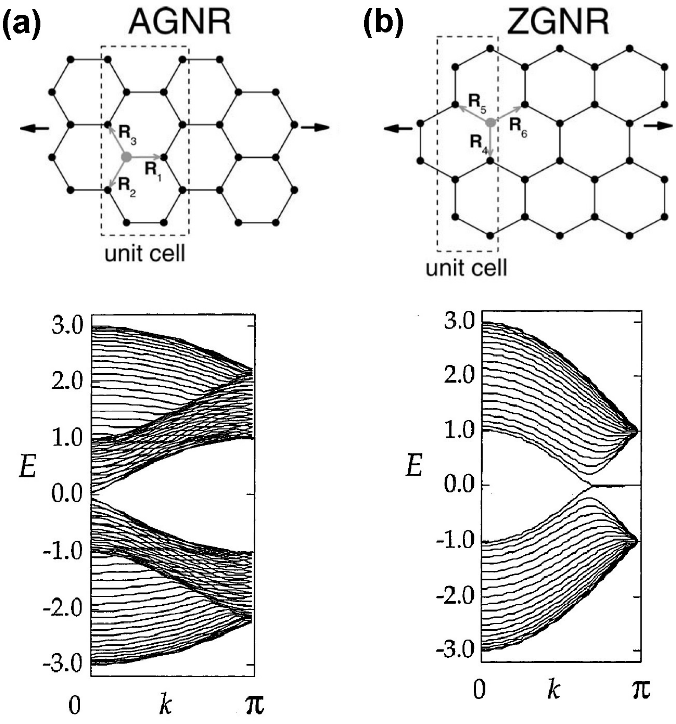

Figure 3.2: Top: Armchair (a) and zigzag (b) nanoribbons. Bottom: Band structures for a 20-AGNR (a) and a 20-ZGNR (b). Taken from reference[7].

3.2 Graphene nanoribbons

Graphene nanoribbons (GNRs), as mentioned earlier, turn into possible solutions to overcome the limitations of a null gap in graphene sheets. In 2008, Li *et al*[27] synthesized nanoribbons with widths less than 10 nm and thus electronically confining the electrons in one of the material's dimensions. The electronic confinement plays an important role at nanometric scales, where the electronic wavelength becomes comparable to the nanoribbon width. Consequently, the high carrier mobility of graphene combines with electronic confinement to give rise to materials with width-dependent bandgap, which are useful for applications as components of transistors at room-temperature , and as an electromechanical switching[86].

The first studies on nanoribbons demonstrated the influence of edge shapes in the response of nanoribbons. In 1987, a TB model applied to polyacenes (1D polymers made up of an arrangement of aromatic rings)[87] showed that the electronic properties of such 1D polyacenes depend on the the geometry of the edges. Later, K. Kobayashi[88] demonstrated by first principles calculations that graphite microstructures with aligned edges presented unusual properties compared with other carbon allotropes, and were directly related with localized states at the edges. Consequently, the classification of the edge shapes would define the electronic character of nanoribbons, and according to their symmetry, the edges can be zigzag, armchair, or a combination of them in chiral edges as shown in Fig.3.1.

3.2.1 Zigzag graphene nanoribbon

GNRs with zigzag edges (ZGNRs) are characterized by edge states with spin-polarization, and antiferromagnetic ordering. TB calculations for a ZGNR show a peak in the DOS at the Fermi level, as a consequence of the localized edge states, as depicted in Fig.3.3. The figure also presents the band structure of the ZGNR, where the edge states appear as a flat band going from $ka = 2\pi/3$ at the K valley, to $ka = \pi$ at X point, with a being the lattice parameter, $a = 2.46\,\text{Å}$. The band structure enhances the electronic localization given in color by the quantity F (defined in Sub-sec.2.4.1), so the edge states are easily identified.

When considering the Hubbard term in our TB model, as described in Sec.2.1, the intra-atomic electronic repulsion induces a bandgap in the ZGNR's electronic structure,

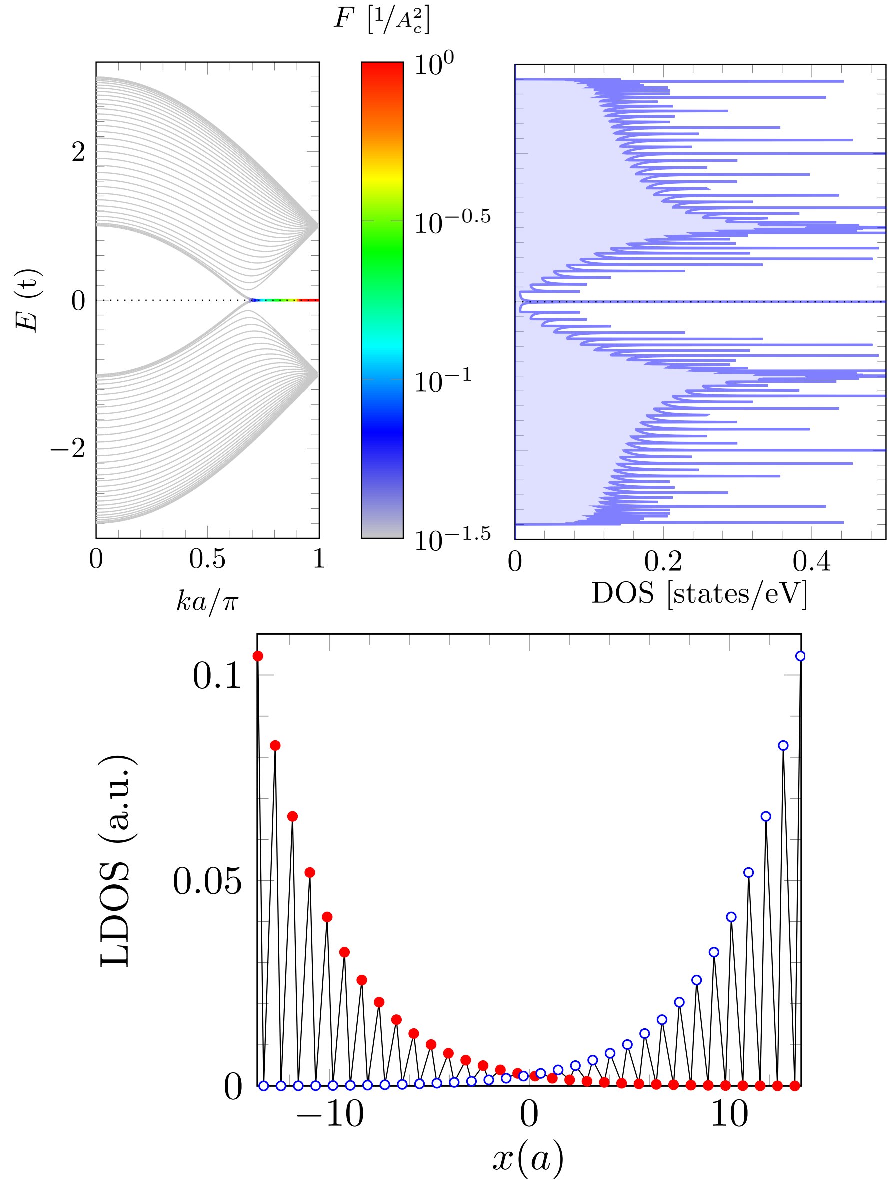

Figure 3.3: Top: Band structure and DOS of a 32-ZGNR when no electronic correlation is considered. Colored lines indicate the F-localization. Bottom: LDOS of the first conduction band at an energy 0.05 eV.

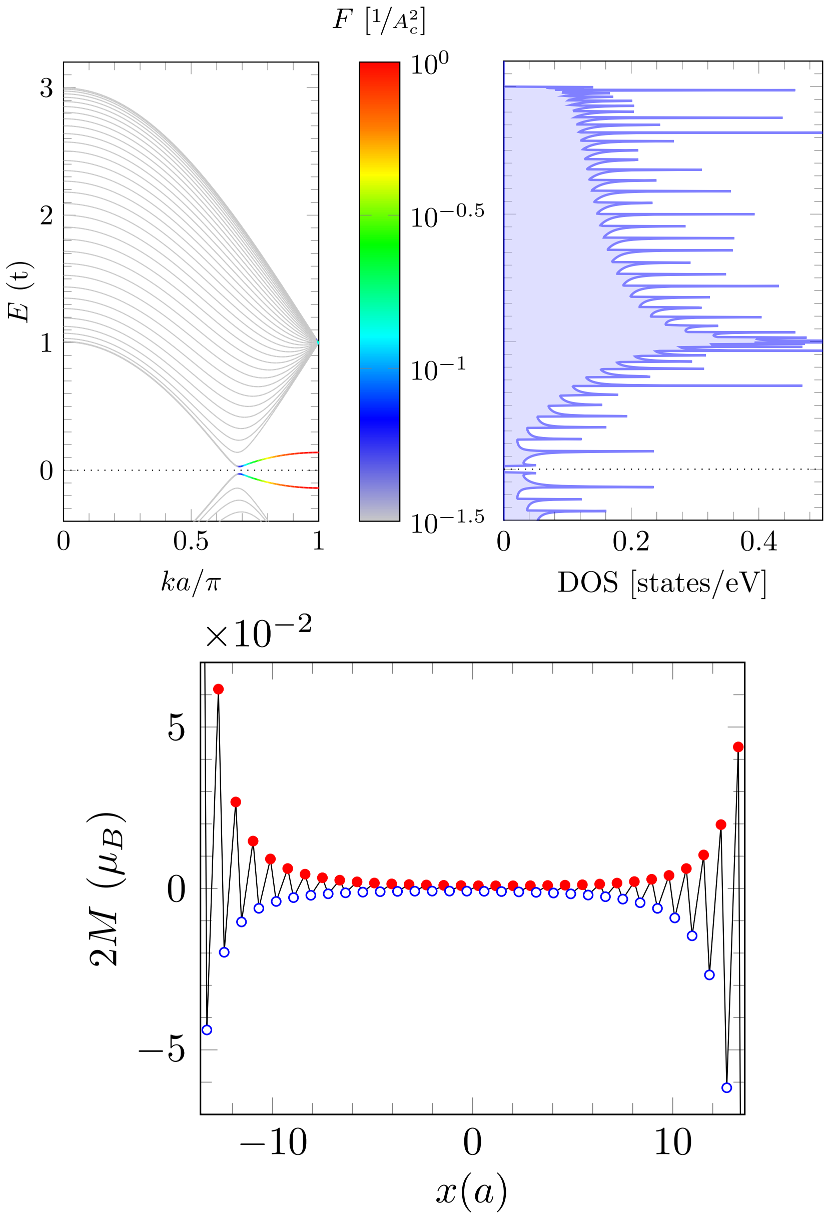

Figure 3.4: Top: Band structure and DOS of a 32-ZGNR when the electronic correlation $U = t = 2.65\,\text{eV}$. Colored lines indicate the F-localization intensity. Bottom: Magnetization through the transverse direction of the ZGNR.

as shown in Fig.3.4. The electronic correlation also redistribute the charges according to the spin of electrons. Fig.3.4(bottom) exhibits the magnetization along the ZGNR. Clearly, the interaction between the edges is in such a way that the redistribution of charge leads to a higer occupation of α-spin electrons at one edge, and higher occupation of β-spin electrons at the other edge. Here, the magnetization is defined as (μ_B is the Bohr magneton)[89]

$$M_i = \frac{\mu_B}{2}\left(\langle n_{i\uparrow}\rangle - \langle n_{i\downarrow}\rangle\right), \tag{3.1}$$

so the electronic interaction leads to a ferromagnetic order at each one of the edges, and an antiferromagnetic order through the ZGNR width.

The electronic and magnetic properties of ZGNRs just discussed turned clear that ZGNRs may be useful for magnetic applications. However, GNRs reactive edges restrict their applications as the edges easily oxidize in the presence of air, affecting its electronic and magnetic properties. Attempts to protect the edges magnetization include edge passivation with hydrogen atoms, with C_2H_4 ethylene molecules[90], or with CO_2 molecules due to its easy absorption and enhancement of ZGNRs magnetic properties by turning it into a ferromagnetic semiconductors[91].

Although this is a stimulating research frame, much of the theoretical predictions still need experimental corroboration. Intrinsic obstacles for direct graphene nanoribbon applications comes from the well defined edges issue. To overcome those limitations, several techniques have been implemented, and include lithography processes and chemical sonification. Additionally, high quality nanoribbons with ultra-defined edges by unrolling carbon nanotubes[92] are promising to verify the unusual properties of ZGNRs.

3.2.2 Armchair graphene nanoribbons

On the other hand, armchair graphene nanoribbons (AGNRs) can behave not just as semiconductors showing a width-dependent bandgap but also as metallic nanowires. TB approximations show that the number of dimer lines defines whether or not the AGNR is a metallic or semiconductor system[93]. If the N-AGNR width, $W = (N-1)/2$ (in terms of a, where a is the lattice parameter) satisfies the condition $^1/_W \ll 1$, then it can be found an analytic expression for the bandgap[89] located at the Γ symmetry point,

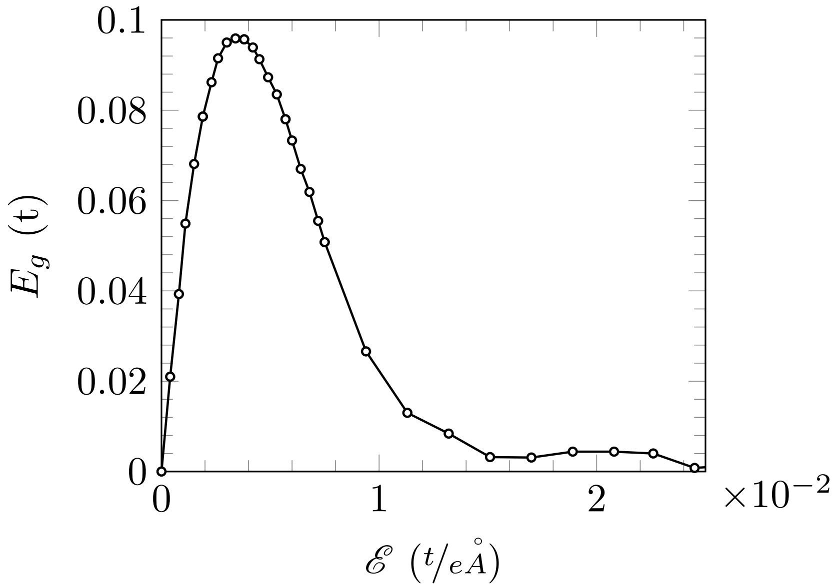

Figure 3.5: Gap evolution with respect to a transverse electric field for a 32-ZGNR.

$$E_g \sim \begin{cases} 0, & N = 3m - 1 \\ \frac{\pi}{W + \sqrt{3}/2}, & N = 3m \\ \frac{\pi}{W}, & N = 3m + 1 \end{cases} \tag{3.2}$$

leaving in evidence the dependence of the bandgap with respect to the nanoribbon width[7]. As a consequence, AGNRs can be a metallic system for the $N = 3M - 1$ family. However, relaxation at the edges of AGNRs leads to an small opening of the bandgap for the $3M - 1$ family[6]. The bandgap behavior has been measured in AGNRs with atomic-level precision, indicating that cutting or adding one dimmer line can totally change the electronic properties of an AGNR[94].

3.2.3 Interaction with external fields

Electric fields affect the electronic response of ZGNRs and metallic AGNRs due to the presence of electronic carriers at the Fermi level. To include the effects of external fields in our TB model, we consider that under the presence of an electric field, a charge q at the position $\vec{r}$ suffers an electrostatic potential energy $\mathcal{V} = -q\vec{\mathscr{E}} \cdot \vec{r}$. This potential can be associated to an operator $\hat{\mathcal{V}}_i = |e|\vec{\mathscr{E}} \cdot \vec{r}_i \hat{n}_i$ acting at the i-site. This term enters in our TB model affecting the on-site energy, as

$$\varepsilon_i' = \varepsilon_i + |e|\vec{\mathscr{E}} \cdot \vec{r}_i. \tag{3.3}$$

Fig.3.5 show the results of a TB calculation for the gap dependence on a transverse electric field. The calculation does not include electronic correlation. The gap increases as the external field increases until reaching a maximum bandgap. For higher values of electric field, the bandgap decreases and oscillates.

3.2.3.1 Half-metallicity

Electronic correlation changes dramatically the scenario depicted in Fig.3.5 for ZGNRs. Son *et al* [33] predicted a half-metallic response for ZGNRs in the presence of electric fields. i.e. when the ZGNR behaves as a metallic system for α-electrons, while it behaves as a conductor for β-electrons, with α and β being up and down spin components.

To understand the process, let's consider the system before applying an electric field. In this case, in the single-orbital model, the occupation at the i-th site is $n_i = 1$. When a transverse electric is applied to a ZGNR, and considering a sufficiently small electric field, then we can argue that every i-th site experiences an increase (or decrease) in the occupation of energy potential of the form $n_i = 1 - |k|\mathcal{V}(\vec{r}_i)$, where k is a constant and $\mathcal{V}(\vec{r})$ is a symmetric energy potential centered at the nanoribbon.

Also, the occupation at every i-site is the contribution from its up and down components $n_i = n_{i\uparrow} + n_{i\downarrow}$. If we write the magnetization as $m_i = n_{i\uparrow} - n_{i\downarrow}$, then we can demonstrate that

$$\begin{aligned} n_{i\uparrow} - \tfrac{1}{2} &= -\tfrac{1}{2}|k|\mathcal{V}_i + \tfrac{1}{2}m_i, \\ n_{i\downarrow} - \tfrac{1}{2} &= -\tfrac{1}{2}|k|\mathcal{V}_i - \tfrac{1}{2}m_i. \end{aligned} \tag{3.4}$$

In an antiferromagnetic ordering solution, $\alpha(\beta)$-spin electrons occupies mostly the left(right) edge. So, the magnetization at the edges satisfies $m_L = -m_R \equiv \mathcal{M}$. Then, in the absence of an external electric field ($V = 0$), the effective on-site energy of the i-th site in the Hubbard model ($\varepsilon_{i\sigma}' = \varepsilon_0 + U(\langle n_{i\bar{\sigma}}\rangle - {}^1\!/_2)$) takes the following form

$$\begin{aligned}
\varepsilon_{L\uparrow}(0) &= \varepsilon_0 - \tfrac{1}{2}U\mathcal{M}, \\
\varepsilon_{R\uparrow}(0) &= \varepsilon_0 + \tfrac{1}{2}U\mathcal{M}, \\
\varepsilon_{L\downarrow}(0) &= \varepsilon_0 + \tfrac{1}{2}U\mathcal{M}, \\
\varepsilon_{R\downarrow}(0) &= \varepsilon_0 - \tfrac{1}{2}U\mathcal{M}.
\end{aligned} \tag{3.5}$$

When applying a transverse electric field, the edges are under an electric energy potential, $\mathcal{V}_L = -\mathcal{V}_R = |e|\triangle V$. So, the effective on-site energies at the edges become

$$\begin{aligned}
\varepsilon_{L\uparrow}(\triangle V) &= \varepsilon_{L\uparrow}(0) - \tfrac{1}{2}U|ke|\triangle V, \\
\varepsilon_{R\uparrow}(\triangle V) &= \varepsilon_{R\uparrow}(0) + \tfrac{1}{2}U|ke|\triangle V, \\
\varepsilon_{L\downarrow}(\triangle V) &= \varepsilon_{L\downarrow}(0) - \tfrac{1}{2}U|ke|\triangle V, \\
\varepsilon_{R\downarrow}(\triangle V) &= \varepsilon_{R\downarrow}(0) + \tfrac{1}{2}U|ke|\triangle V.
\end{aligned} \tag{3.6}$$

Therefore, an increasing transverse electric field shifts down(up) the energy spectrum at the left(right) edge. The process continues until attaining a critical electric field value, where states at one edge become available to electrons at the other edge, with energy being equal to the Fermi level. At this point, the bandgap for one of the spin channel closes. Consequently, only electrons with a specific spin moves at the Fermi level allowing a spin-polarized current.

The half-metallic response turns ZGNRs interesting for spintronic applications. However, high external electric field values are required to produce such a response. Research to reduce the electric field values includes chemical functionalization by edge-oxidization[95], functionalization to carbon nanotubes[96], and hybridization with h-BN nanoribbons. In this work we are going to focus in hybrid systems of graphene and h-BN as they combine the conductive properties of graphene with the dielectric characteristics of h-BN, and shows an intrinsic half-metallicity without the presence of an external electric field.

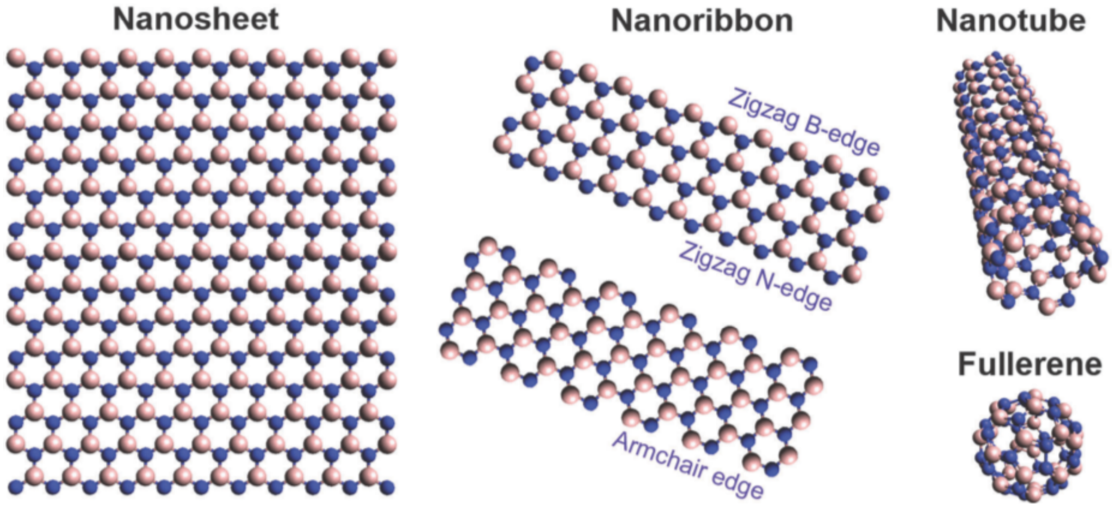

Figure 3.6: 2D and 1D h-BN structures counterpart of graphene systems. Taken from [8]

3.3 Boron nitride structures

Hexagonal boron nitride (h-BN) sheets are considered as the 2D isostructural and isoelectronic counterpart of graphene (see Fig.3.6). Composed of boron and nitrogen atoms disposed in a regular network of BN hexagons, the material has an indirect bandgap of 5.955 eV[97]. The lattice parameter of h-BN is $a_{BN} = 0.251\,\text{nm}$, just 1.8% larger than the lattice constant of graphene, 0.251 nm[98, 99]. The system is partially ionic due to the large different electronegativities of boron and nitrogen atoms. Hence, the system is more stable in a multilayer AA' Bernal configuration[8], difficulting the process of isolating a monolayer h-BN sheet via the exfoliation process.

Synthesis of h-BN gained attention as an alternative for mechanical support in STM measurements on graphene samples[100]. The interaction between graphene and SiO_2 substrates interfere with graphene's electronic performance and turns inaccessible to Dirac's physics at the neutrality point. However, h-BN shows itself as a dielectric layer, free of dangling bonds and charge traps due to its high oxidation resistance. Also, STM measurements exhibits a $\sim$ 100 times more smooth surface when compared to the high roughness of SiO_2 and an enhancement of the electronic mobility[98, 99, 101]. Recent applications includes encapsulated carbon nanotubes in h-BN to be used in field effect transistors[102], showing a 6-7 times current enhancement trough the nanotube, compared with SiO2 substrates.

One-dimensional structures can also be obtained from h-BN sheets, by unzipping h-

	B	C	N
electronegativity	2.04	2.55	3.04
calculated ratio	87 pm	67 pm	56 pm
valence electrons	3	4	5

Table 3.1: Electronegativity values of boron, nitrogen and carbon atoms. Taken from ref.[17].

BN nanotubes, for example. However, differently to quasi 1D graphene structures, h-BN nanoribbons have a non zero bandgap for both armchair (ABNNR) and zigzag boron nitride nanoribbons (ZBNNR), and due to its semiconductor features, it has application in optics and opto-electronics[103].

BNNRs are dielectric materials due to the difference between B and N electronegativities (see Table 3.1). However, edge functionalization can modify their electronic properties[104]. DFT calculations show that ABNNRs hydrogenated at boron edges, or Fe-edge terminated, may lead to a half-metallic state[105–107]. Also, ZBNNRs hydrogenated at only one edge[13] or $\sim 80\%$ hydrogenated through the ribbon[108] could lead to a half-metallic system without the requirement of an external electric field. The results open the way to the study of hybrid systems graphene/h-BN that combines the conductive properties of graphene and the ionic nature of h-BN nanoribbons.

4

Hybrid nanoribbons

Hybrid structures may allow the use of a single graphene layer in field effect transistors. Calculations performed[109] on graphene layer sandwiched in h-BN sheets have revealed not only a tunable bandgap when applying an external electric field, but also a higher on/off current ratio through the graphene sheet when compared with a pure single graphene layer. It is shown that the stacking configuration influences the electronic properties of the hybrid system. For h-BN sandwiched between graphene layers, the bandgap of the hybrid system in the presence of an electric field reaches maximum values for the the AAA stacking configuration[9](see Fig.4.1). Also, according to DFT calculations, hybrid structures made up of bilayer graphene over stacked h-BN sheets have shown to have a tunable bandgap depending on the number of h-BN layers, and leading to a conductor material when a perpendicular electric field is applied[10].

Here we focus on the study of systems where half-metallicity is achieved without the presence of an external electric field. We combine the dielectric properties coming from the high electronegativity difference between boron and nitrogen atoms in ZBNNRs with the spin-dependent properties of ZGNRs. The hybrid system would consist of a planar ZGNR structure embedded in a pair of ZBNNRs. Such systems might be synthesized through a series of CVD steps[3, 110] or etching graphene over lithographic patterned h-BN[111]. STM measurements of hybrid h-BN/graphene interfaces are shown in Fig.4.2. We describe the effects of zigzag edges on ZBNNRs on the electronic structure using edge potentials. Then, we study hybrid ZBNNR/ZGNR/ZBNNRs, where ZBNNRs induce an electric field across the zigzag graphene strip, breaking the spin degeneracy of the electronic band structure. We propose a correction to the on-site energies in the used TB model in the form of edge and interface potentials. A set of optimal TB parameters are found from DFT calculations that enables us to explain non-magnetic and spin-dependent band structures of hybrid systems.

4.1 Edge potentials in ZBNNRs

DFT calculations predict an indirect gap for ZBNNRs as shown in Fig.4.3. Here E_g is the indirect gap energy and E_X is the energy difference between the highest valence band and the lowest conduction band at $ka = \pi$ (X symmetry point). Fig.4.4 exhibits the behavior of E_g and E_X with respect to the nanoribbon width, where we compare our DFT results (blue symbols) with the results from ref.[12]. Additionally, TB approximation can also explains the behavior of E_g and E_X.

In Fig.4.5(left) we compare the DFT band structure of a 12-ZBNNR with our simple TB model. By identifying the edge states at $ka = \pi$, we can estimate the on-site energy values at the edge sites to be used in our TB model (see Sec.2.4). The eigenvalues of the hamiltonian 2.65:

$$H_{ka=\pi} = \begin{pmatrix} [\varepsilon_B] & 0 & 0 & & & & 0 \\ 0 & \varepsilon_N & t & 0 & & & \\ 0 & t & \varepsilon_B & 0 & & & \\ & 0 & 0 & \ddots & 0 & 0 & \\ & & & 0 & \varepsilon_N & t & 0 \\ & & & 0 & t & \varepsilon_B & 0 \\ 0 & & & & 0 & 0 & [\varepsilon_N] \end{pmatrix}, \tag{4.1}$$

will give us directly the on-site energies ε_B and ε_N for boron and nitrogen atoms. The resulting TB band structure is shown in Fig.4.5(right). However, we can notice two main differences of TB with respect to the DFT band structures: a degenerated state at $ka = \pi$, and the presence of highly-localized flat bands. Also, according to this TB approach, E_g and E_X would be equal between them, and would show no dependence on the nanoribbon width. To solve those differences, Zheng *et al*[13] proposed a correction to the on-site energies in the form of exponential-like edge potentials. The correction comes from the different electronegativities of boron and nitrogen atoms, and the partially ionized edges composed of just boron or nitrogen atoms. The proposed edge potentials reads

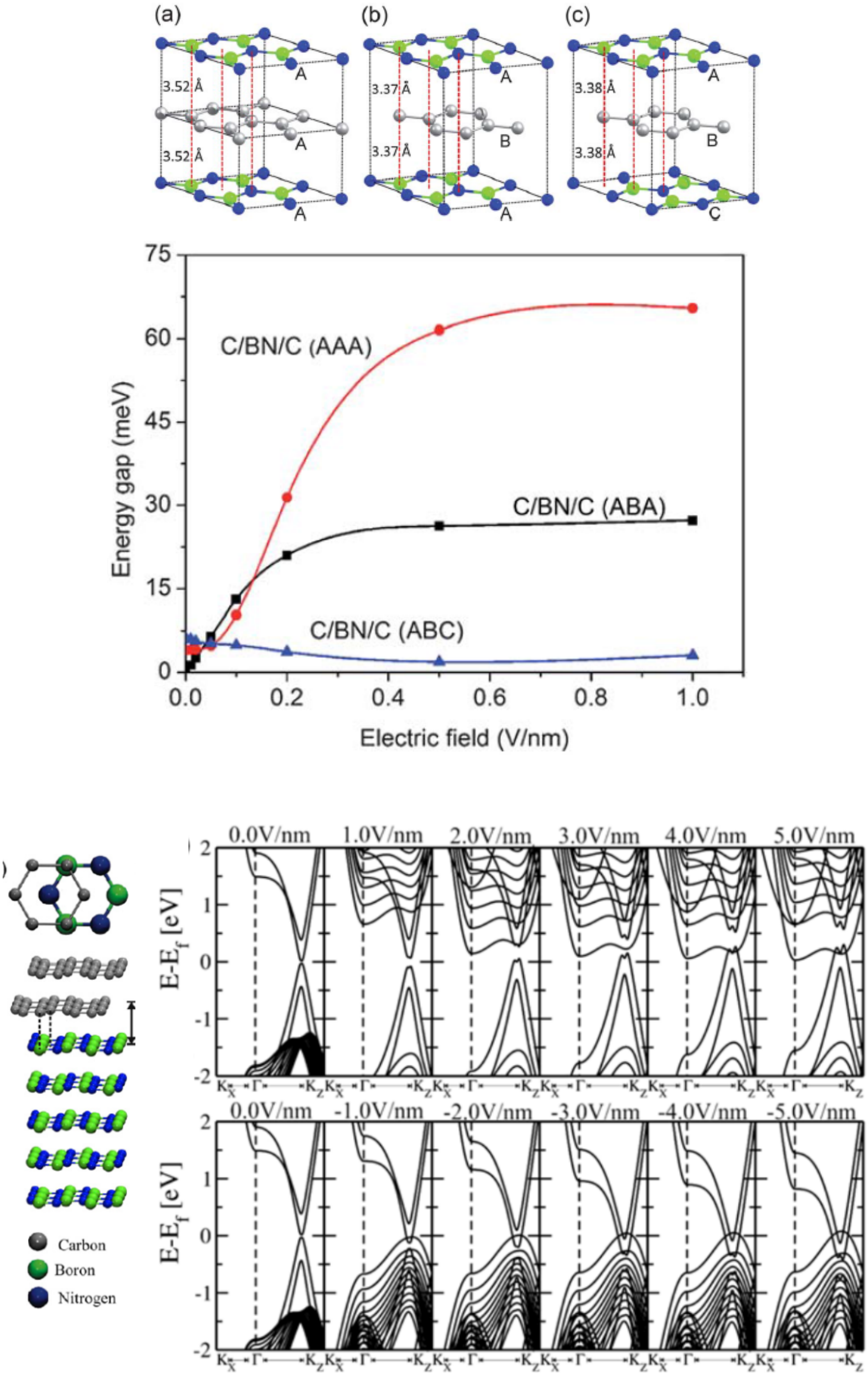

Figure 4.1: Top: Different stack configurations for an hybrid h-BN/graphene system and their responses to an external electric field. Bottom: Band structure of a bilayer graphene deposited over h-BN layers. The h-BN can introduce new states into the bandgap. Taken from [9](top), and [10](bottom).

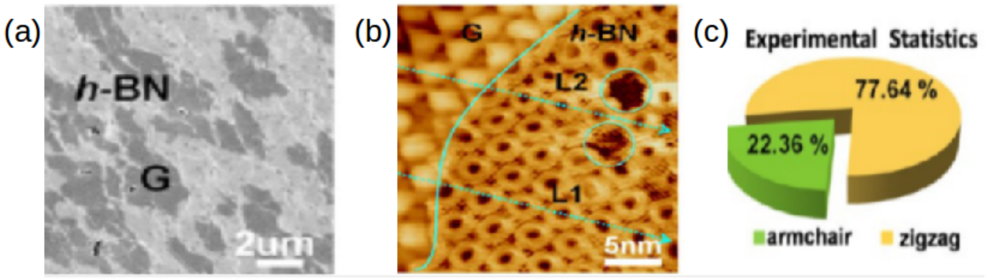

Figure 4.2: (a) SEM morphology and (b) STM measurements of hybrid h-BN/graphene interfaces. (c) Most of the samples stabilize in zigzag interfaces. Taken from ref.[11].

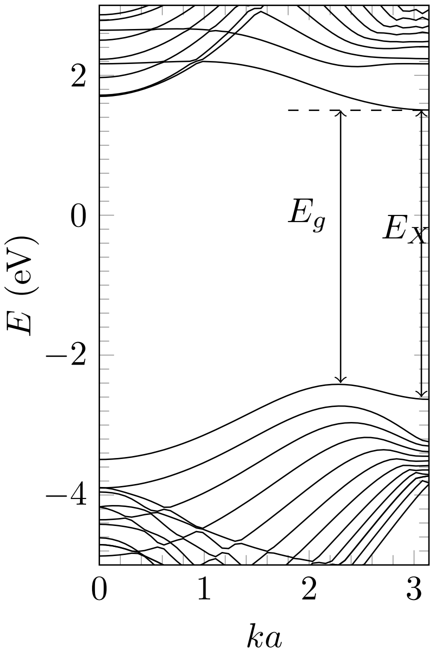

Figure 4.3: 12-ZBNNR band structure according to our DFT calculations.

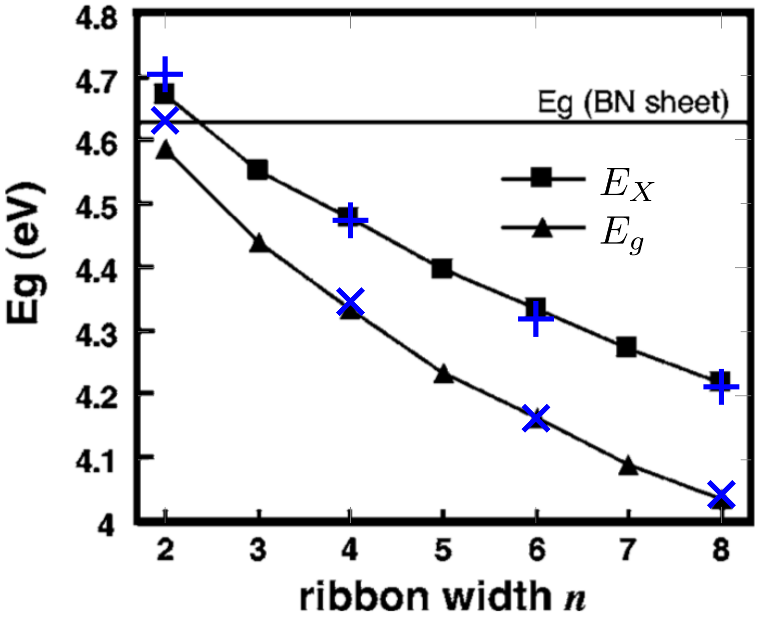

Figure 4.4: n-ZBNNR gap evolution with respect to the nanoribbon width n. Filled black symbols correspond to DFT results from Nakamura *et al* (figure adapted from [12]), while blue symbols correspond to our DFT calculations.

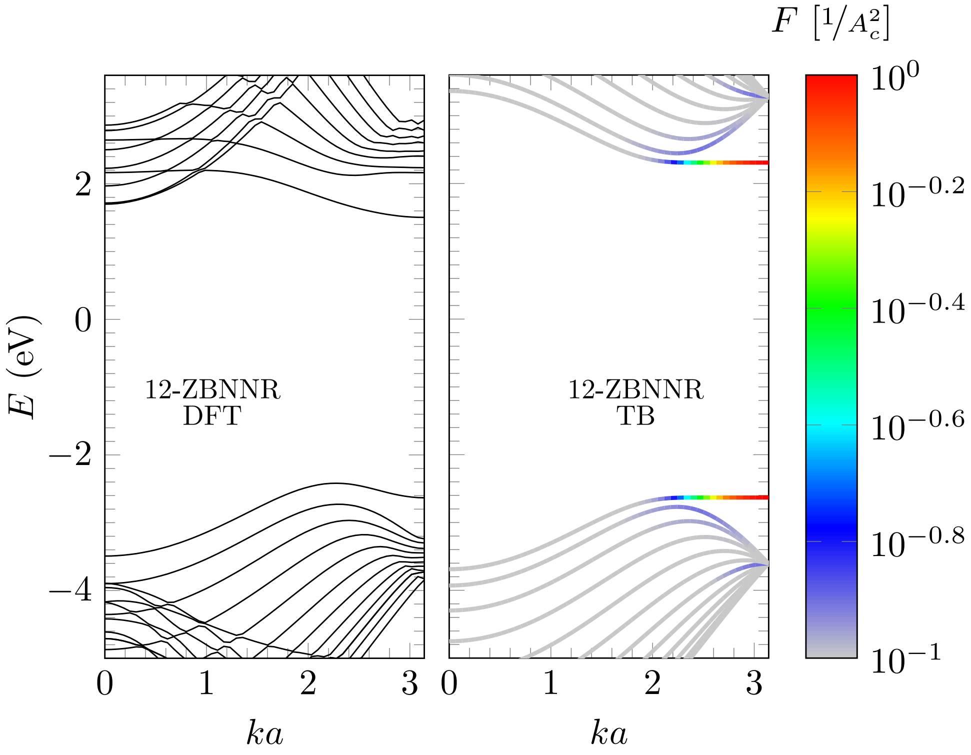

Figure 4.5: 12-ZBNNR band structures according to DFT (left) and TB (right) calculations. Highly localized states are in red.

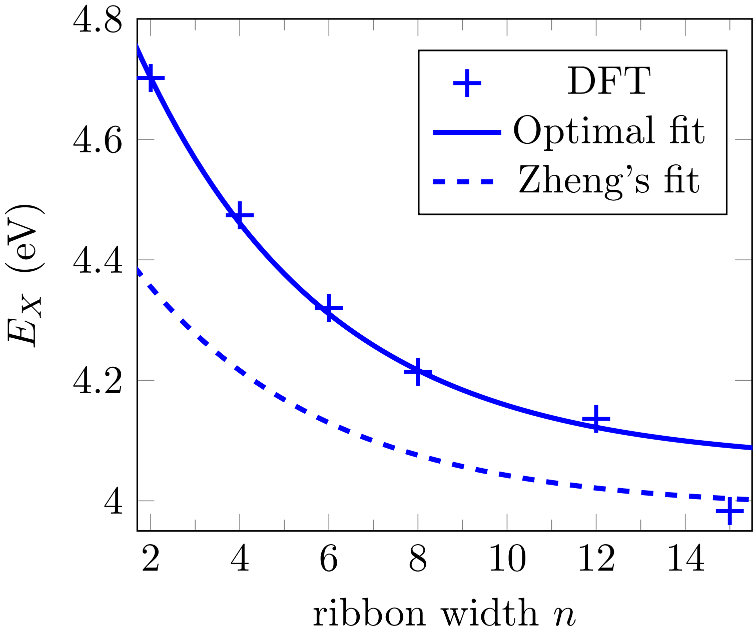

Figure 4.6: Fitting DFT results and E_{gX1}, compared to predictions from reference [13].

	$\triangle$(eV)	λ(Å)	$\delta P \equiv (P_B - P_N)$
Optimal fit	2.470	9.0	$-0.356\triangle$
Zheng et al[13]	2.246	9.0	$-0.225\triangle$

Table 4.1: Parameter values for E_{gX} to fit with DFT results in our TB calculations and obtained by Zheng *et al*[13].

$$V_{\text{edge}}(x) = P_B e^{-|x-x_B|/\lambda} + P_N e^{-|x-x_N|/\lambda}, \tag{4.2}$$

where x_B and x_N are the posititions of the boron and nitrogen edges. P_B, P_N and λ being parameters to be adjusted to fit DFT results. If we define $\triangle \equiv (\varepsilon_B - \varepsilon_N)/2$ and $\delta P \equiv (P_B - P_N)$, then it can be demonstrated that[13]

$$E_X(L) = 2\triangle + \delta P \cdot (1 - e^{-L/\lambda}) \tag{4.3}$$

where L is the nanoribbon width. So, by adjusting an optimal δP value, we can fit E_X from DFT calculations by means of the last expression. Fig.4.6 shows the resulting fitting we found, superposed to our DFT data. We also compare our fit with that of Ref.[13]. In Table 4.1 we display the fitting parameters.

On the other hand, we were unable to reproduce the DFT band structures of different

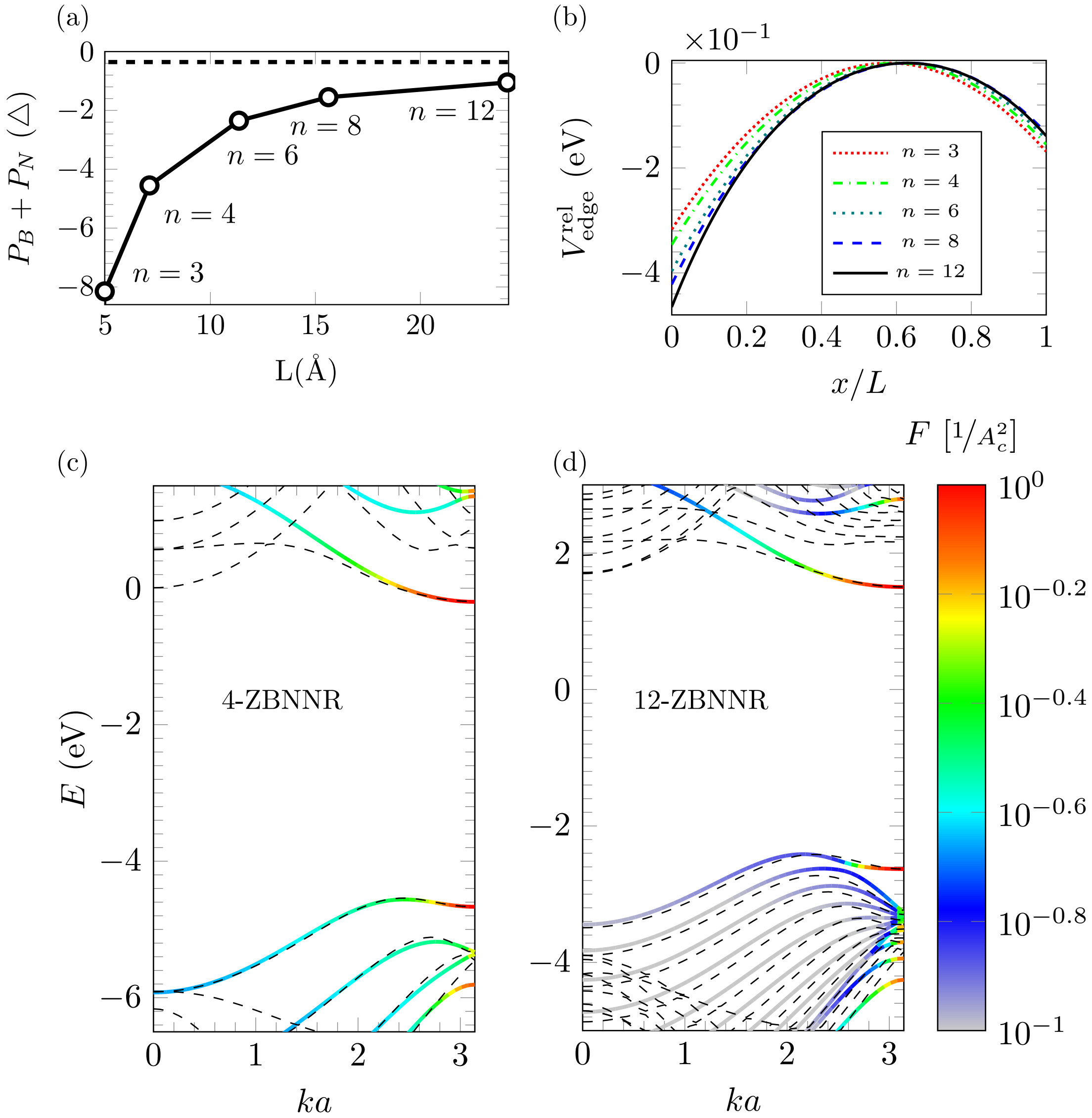

Figure 4.7: (a) Dependence of $P_B + P_N$ with respect to the nanoribbon width in order to match TB band structures and DFT results. Dashed line corresponds to the limit case $P_B = -0.356\triangle$ and $P_N = 0$. (b) Relative edge potentials correcting the atomic on-site energies along the n-ZBNNR. The relative edge potential is calculated with respect to its maximum value. (c, d) Electronic band structures for 4 and 12-ZBNNR. Dashed lines indicate DFT calculations and colored lines show TB results including edge potentials. Colors indicate the F-localization.

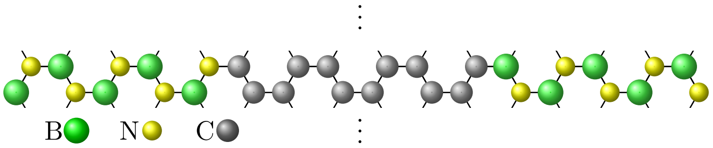

Figure 4.8: Unit cell of the hybrid 5BN/6G/5BN.

nanoribbon widths by using a unique pair of P_B and P_N values. We adjusted the TB band structures to the DFT results by means of a set of P_B and P_N values. While $\delta P \equiv (P_B - P_N)$ can be fixed to a constant value, as indicated in Table 4.1, each parameter depends on the nanoribbon width, as implied by the dependence of the sum $P_B + P_N$ shown in Fig.4.7(a). Even though this figure shows higher P_B and P_N values for shorter nanoribbons, the difference $\delta P \equiv (P_B - P_N)$ preserves the constant value. Fig.4.7(b) shows the resulting V_{edge} when fitting P_B and P_N values for different nanoribbon widths. For comparison, we have normalized the nanoribbon width, L, to 1. Fig.4.7(c) and (d) show the TB band structures of ZBNNRs when using an optimal fitted V_{edge} to match DFT band structures.

4.2 Interface potentials in zigzag hybrid systems

Here we study an hybrid system made up of a graphene stripe embedded in ZBNNRs. Optimal on-site energies and hopping parameter values for other BN/graphene systems are reported elsewhere[18]. However, for the present hybrid system, we adjust those parameter values to obtain an electronic effective potential[112], affected by the presence of ZBNNR's edges and BN/C interfaces. We follow a similar recipe to edge potentials proposed by Zheng et al[13], to study the hybrid system with B and N edges (see Fig.4.8). Additionally to the edge corrections, we also consider the effects of the zigzag interfaces (N/C and C/B), on the on-site energies of the hybrid system.

The Quantum ESPRESSO (QE)[70] code is also used to compute the electronic structure for the hybrid systems, followed by the WanT Package[72, 73] to obtain on-site and hopping energy values. The codes provide a procedure based on projecting the Khon-Sham solutions into localized atomic orbitals. The corresponding Hamiltonian in the real space has a Slater-Koster-matrix shape[68] from which we may obtain the TB parameter values. Even though the post-processing DFT calculations consider interaction between a large range of neighbor atoms, we are just interested in the on-site energy and first nearest

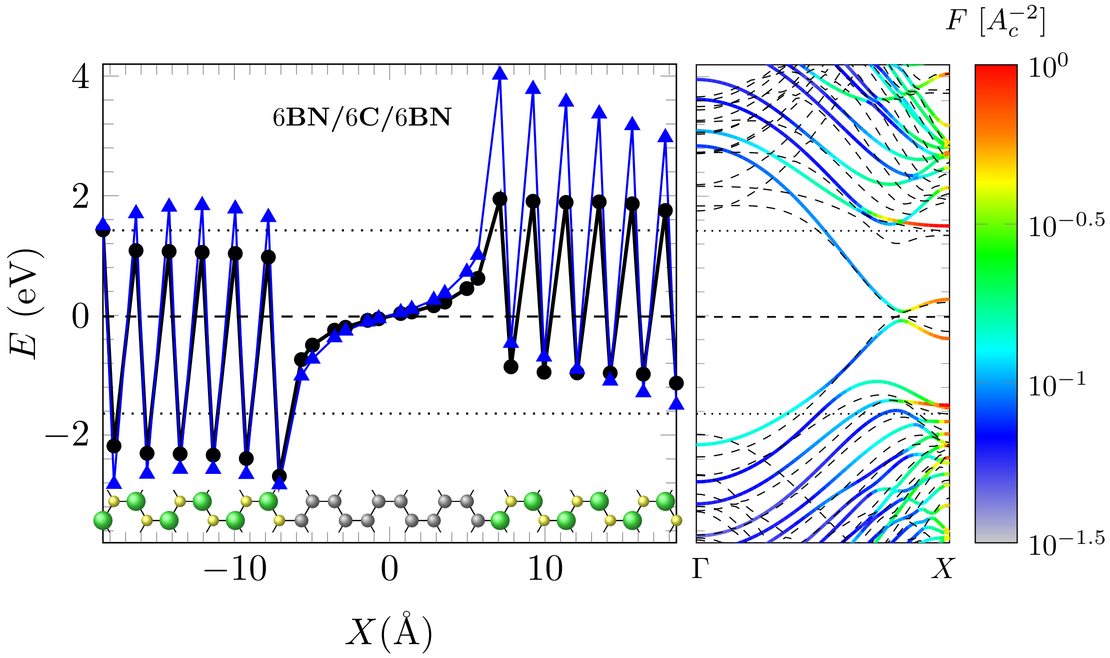

Figure 4.9: Left: On-site energies according to DFT calculations (black symbols) and TB model (blue symbols). The inset shows the unit cell of the zigzag hybrid system. Right: DFT (dashed lines) and TB (colored lines) band structures. Colors indicate the F-localization.

neighbor hopping values. Therefore, the parameters obtained from QE and WanT will be taken and adjusted to build an optimal set of TB parameters, accordingly to the present demand. The results obtained from post-processing DFT calculations for the on-site energy values, ε_i, for B, N and C atoms are shown as black circles in Fig.4.9, which may be fitted into an envelope function according to

$$\varepsilon_i = \varepsilon_i^{(0)} + V(x_i) \tag{4.4}$$

where $\varepsilon_i^{(0)}$ are the on-site energy values for the i-site far enough from the edges or interfaces.

The envelope function $V(x)$ is not directly obtained from post-processing DFT calculations due to the influence of a large number of neighbor interactions. Here, we are interested in an effective TB model taking only the first nearest neighbor interactions. Blue triangles in the left panel of Fig.4.9 are obtained by using an optimal envelope that reproduces quite well the band structures of several hybrid systems. The optimal envelope function is proposed within a similar recipe for edge potentials in ZBNNRs as exponential-type functions . Here, the present proposal incorporates the effects from BN

P_B	P_N	P_G	λ	λ_G
$-1.18\,\mathrm{eV}$	$-0.66\,\mathrm{eV}$	$1.5\,\mathrm{eV}$	9.0Å	1.7Å

Table 4.2: Parameter values for the effective potential through our hybrid system.

edges and BN/graphene interfaces, i.e. for the BN region we have the same contribution from the edges, as done in the previous section,

$$V_{\text{edge}}(x) = P_B e^{-|x-x_B|/\lambda} + P_N e^{-|x-x_N|/\lambda}, \tag{4.5}$$

which accounts for the different electronegativities and high π-electron density at x_B and x_N edges. For the internal graphene strip the contributions from the interfaces are chosen also as decaying exponential functions centered at the x_L and x_R interfaces,

$$V_{\text{int}}(x) = -P_G e^{-|x-x_L|/\lambda_G} + P_G e^{-|x-x_R|/\lambda_G}. \tag{4.6}$$

Post-processing DFT calculations may provide the hoppings and the atomic on-site energies. However, DFT consider many neighbor contributions, while we are interested in the first-neighbor interaction for our simple TB model. Also, unnocupied states with high kinetic energy may have plane-waves components that do not project well in a finite atomic basis[113] and may lead into unphysical atomic on-site energy values. To ovecome this difficulty, we can estimate the B and N on-site energy values by identifying the edge states in a band-structure diagram, as explained in 2.4. To identify the edge states, we calculate the degree of localization in all electronic bands according to the localization function F defined in Sub-sec.2.4.1. The band structure diagrams are shown in Fig.4.9 for DFT and TB calculations. For the TB diagram, the degree of localization is indicated in color, where the maximum value $F = 1$ corresponds to the case where the electron is localized in just one atom. Maximum F values happen at $ka = \pi$ for electrons localized at the B or N atoms at the edges of the zigzag nanoribbon (indicated by the upper and lower dotted lines in the same figure). Then, by adjusting the on-site energy values of B and N, we are able to match the boron-nitride edge states of DFT and TB band structures.

The resulting parameter values for edge and interface potentials are shown in Table4.2. The λ_G value describes a short-range interface potential when compared to the edge potentials range, λ, in the BN nanoribbon regions. This is a reasonable result since the graphene stripe is composed just of carbon atoms (no changes in the electronegativity

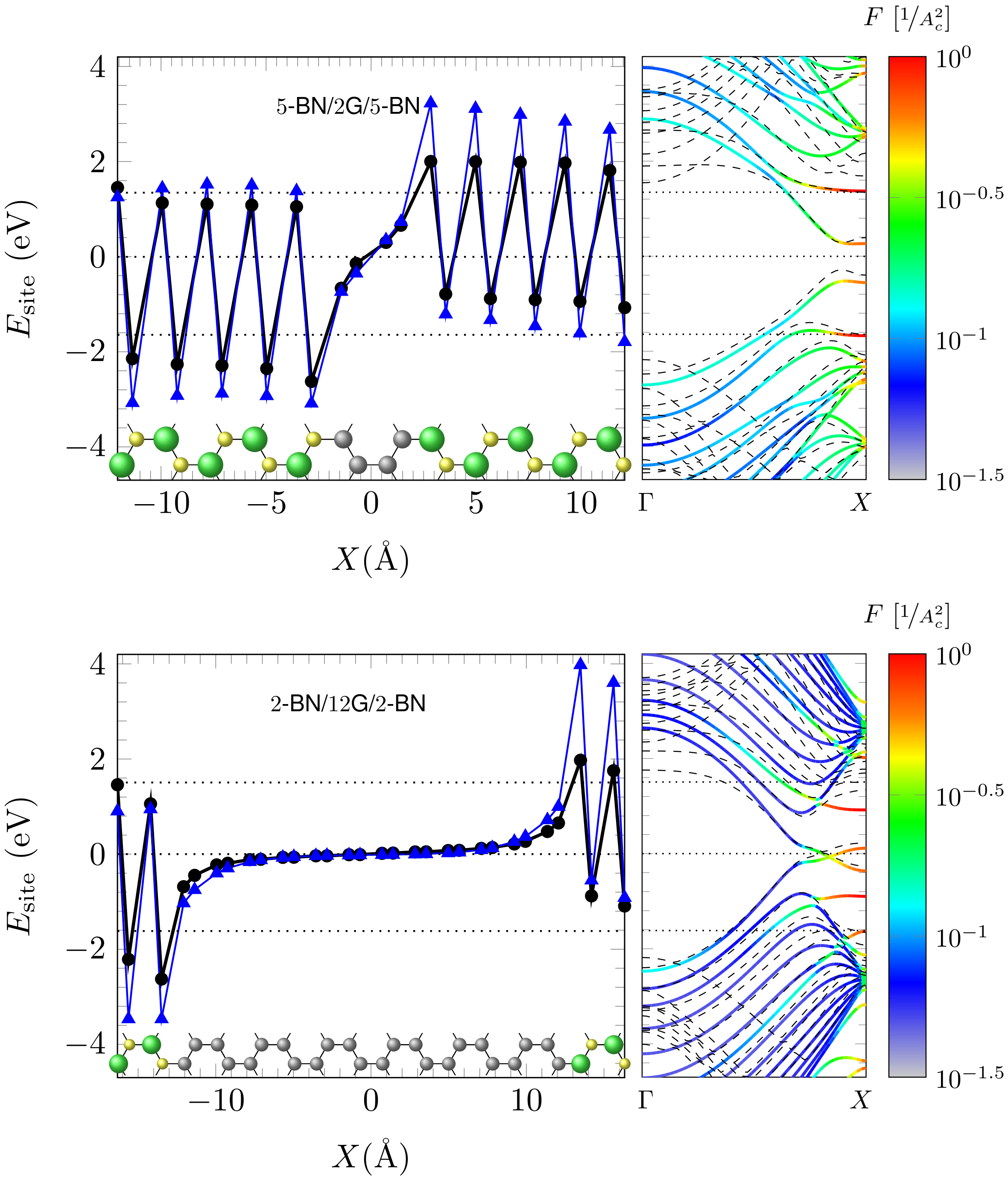

Figure 4.10: Results for 5BN/2G/5-BN and 2BN/12G/2-BN structures. **Left**: On-site energies according to DFT calculations (black symbols) and TB model (blue symbols). The insets show the unit cells of the zigzag hybrid systems. **Right**: DFT (dashed lines) and TB (colored lines) band structures, where colors indicate the F-localization.. The same TB parameters and fitting curves were used for short (**top**) and long (**bottom**) graphene stripes.

$\varepsilon_C^{(0)}$	$\varepsilon_B^{(0)}$	$\varepsilon_N^{(0)}$	t_{CC}	t_{CB}	t_{CN}	t_{BN}	U_C	U_B	U_N
0.0	3.31	-1.09	-2.65	-2.25	-1.80	-2.40	2.7	0.0	0.0

Table 4.3: Optimal TB parameter values for our zigzag mBN/nG/mBN nanoribbon systems. Units are given in eV.

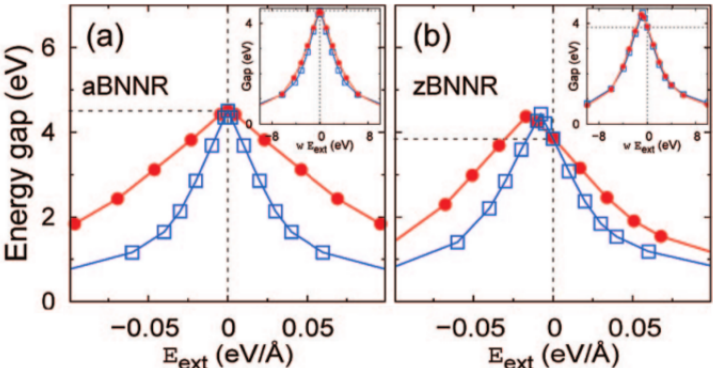

Figure 4.11: First principle results of Park et al [14] for a 36(red symbols)- and 84(blue symbols)-ABNNR **(a)** and 27(red symbols)- and 46(blue symbols)-ZBNNR **(b)** as a function of a transverse electric field. Insets indicate the gap response to a potential difference between the edges.

values happen through the graphene stripe) where charge carriers are more susceptible to electronic screening when compared with the BN region. It is important to remark that the same TB parameter values explain the main band structure features of other hybrid systems, and the interface potential proposed fits them even for wider graphene stripes, as shown in Fig.4.10, where the exponential behavior from interfaces is more clear. Actually, we have worked with a set of mBN/nG/mBN with $(m; n) =$ (5; 2, 3, . . . , 6), (3; 6), (4; 6), (4; 4), (2; 12).

The curves were fitted by taking $\varepsilon_i^{(0)}$ values to be in agreement with TB results from Zhao *et al* work[18] for BN quantum dots embedded in graphene. Here we considered those values with some adjustments (see Table 4.3) to better reproduce the DFT band structure of the hybrid systems. We shifted the on-site energy values for B and N atoms by 0.55 eV to match TB and DFT band structures at $ka = \pi$. Also, we depart 0.10 eV from their t_{CN} value to explain better the non-magnetic solution for 5BN/2G/5BN, as discussed in the next sub-section.

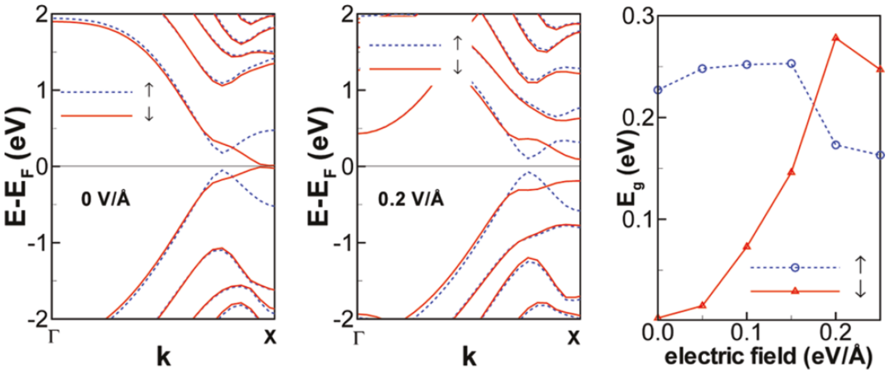

Figure 4.12: First principle results of Bhowmick et al[15]. Left: Half-metallicity in an in-plane hybrid h-BN/6G/h-BN system. Center: Half-metallicity is lifted at a critical value of a transverse electric field. Right: Gap dependence of the hybrid system with respect to the external electric field.

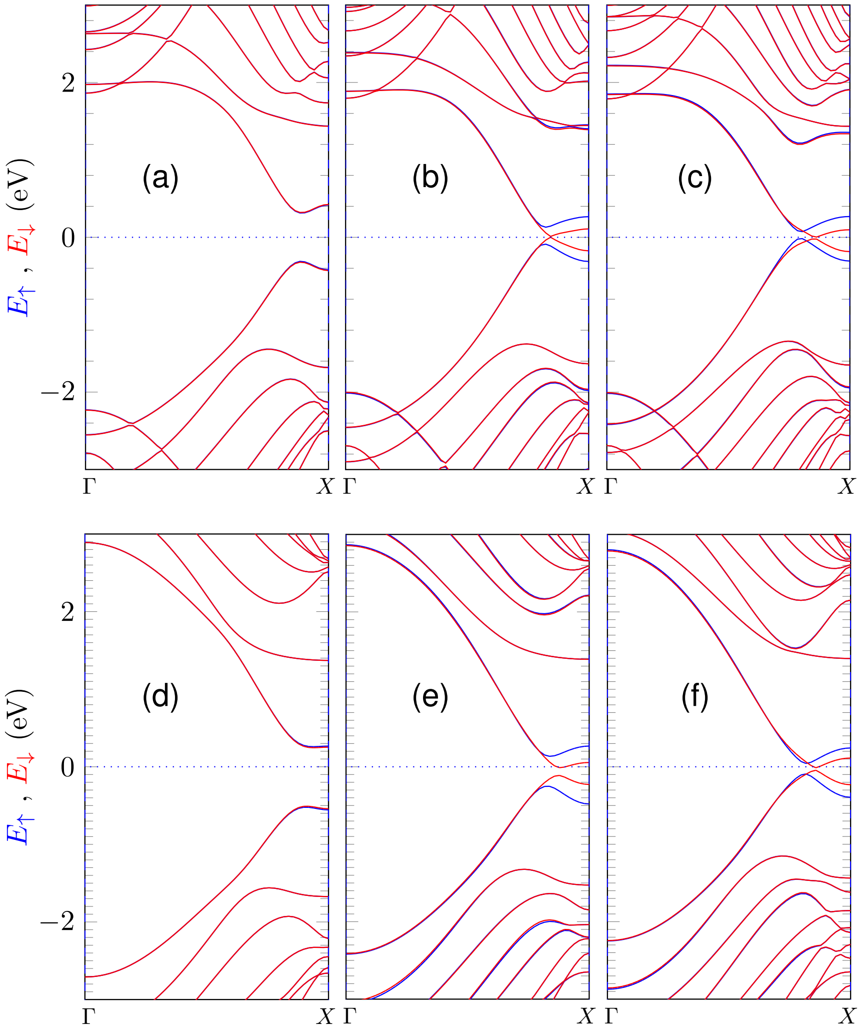

Figure 4.13: DFT(top) and TB(bottom) band structure calculations for mBN/nG/mBN ribbons. $(m; n) = (5; 2)$ for (a) and (d). $(m; n) = (5; 4)$ for (b) and (e). $(m; n) = (5; 6)$ for (c) and (f).

4.2.1 Half-metallicity in hybrid systems

Due to the high electronegativity difference between B and N atoms, an electric field is induced across the ZBNNR. To illustrate this response, we show in Fig.4.11 the dependence of an armchair(a) and a zigzag(b) BNNR with an external electric field. Differently from the armchair response, the asymmetric gap behavior observed for the zigzag BNNR suggests an intrinsic electric field induced in the nanoribbon that can be compensated by an external field in the opposite direction. Furthermore, the half-metallic response of the in-plane graphene embedded in a pair of ZBNNRs is explained by the presence of an effective electric potential generated through the graphene stripe. When an external electric field is applied to the hybrid system in the opposite direction, the gap for the up and down spin channels eventually equal each other at a critical external electric field value as shown in the DFT results by Bhowmick *et al*[15] in Fig.4.12. Here we model the intrinsic field according to Eq.4.6.

When the graphene's width is comparable to λ_G, the interface potential resembles the potential generated by a constant electric field, where the system becomes half-metallic for a critical electric field value[33]. We have adjusted P_G so that half-metallicity is achieved for certain systems (see Fig.4.13), accordingly to reported DFT calculations[114].

Up to now, we have used our TB parameter values in an attempt to retrieve DFT results. Particularly, DFT predicts a half-metallic response for mBN/nG/mBN systems with $(m;n) = (5;4)$ and $(5;6)$, while $(m;n) = (5;2)$ remains as a non-magnetic solution, as shown in Fig.4.13(a-c), in agreement with Ding *et al* results[114]. For comparison, we also show our TB results in Fig.4.13(d-f). Edge states and valence bands (next to the X point at $ka = \pi$) are quite similar to DFT results, and the closing-gap trend for wider graphene stripes is recovered.

Finally, electronic and transport properties are calculated with this fitting. Fig.4.14 shows the band structure of the 5BN/6G/5BN system and the corresponding DOS and transport properties of the hybrid system. The conductance is enhanced for energies around the Fermi level. The hybrid system is antiferromagnetically ordered between the two edges (one interface is spin down and the other interface with spin up).

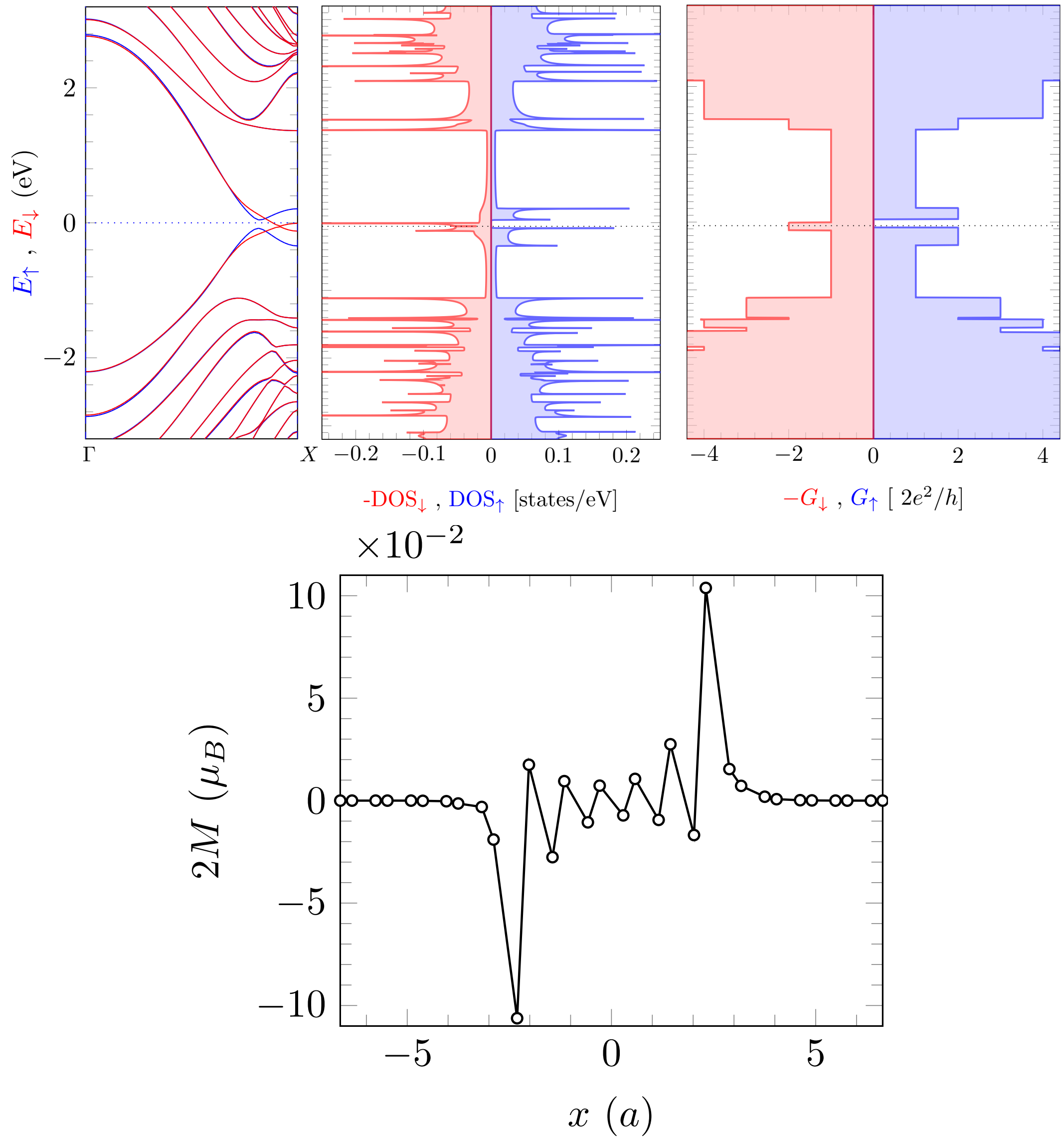

Figure 4.14: Spin-dependent (a) band structures, (b) DOS, and (c) conductance for an hybrid 5BN/6G/5BN system. (d) Magnetization along the unit cell in unit of Bohr magneton.

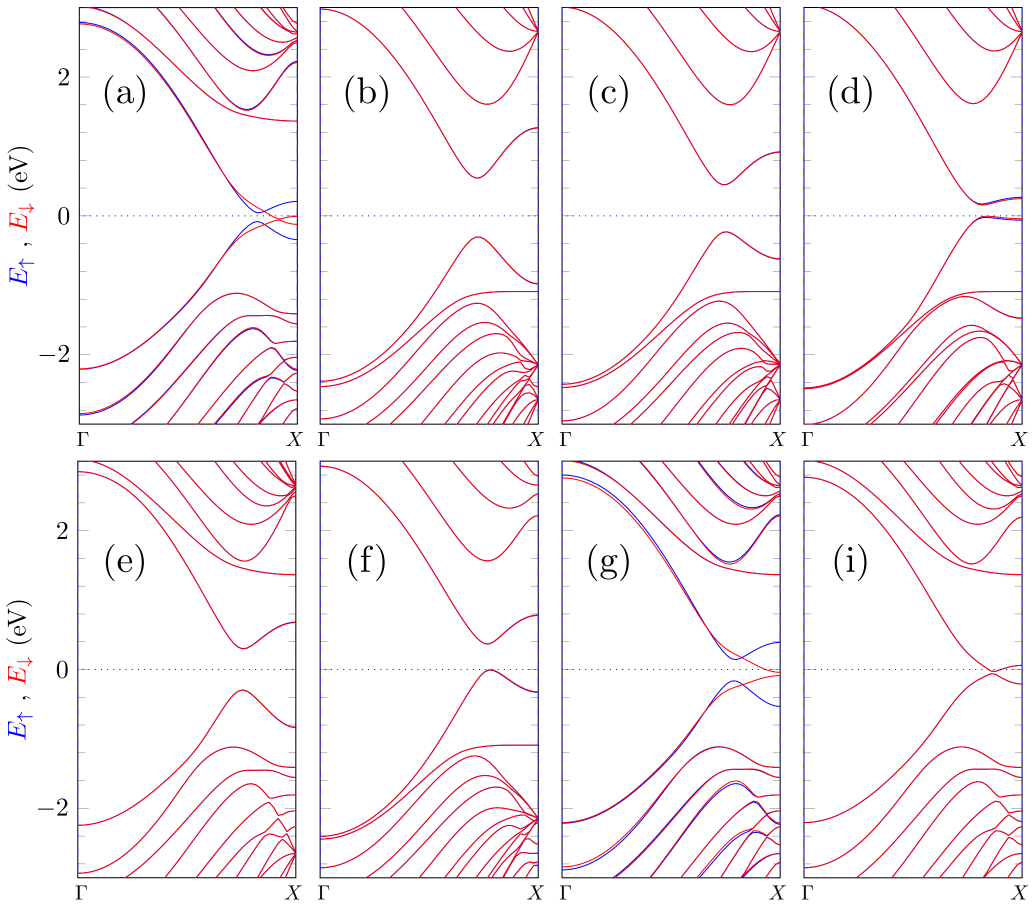

Figure 4.15: Band structures for the 5BN/6G/5BN system, (a) according to the proposed TB and fitting parameters listed in Tables 4.2 and 4.3, (b) zero edge and interface potentials, (c) zero edge and interface potentials and decreased t_{CN}, t_{BN} values by a factor of 0.8, (d) zero edge and interface potentials and decreased t_{CN}, t_{BN} values by a factor of 0.4, (e) zero edge potential, (f) zero interface potential, (g) $U_C = 3.0\,\text{eV}$ with both interface and edge potentials, and (h) $U_C = 0$ with edge and interface potentials.

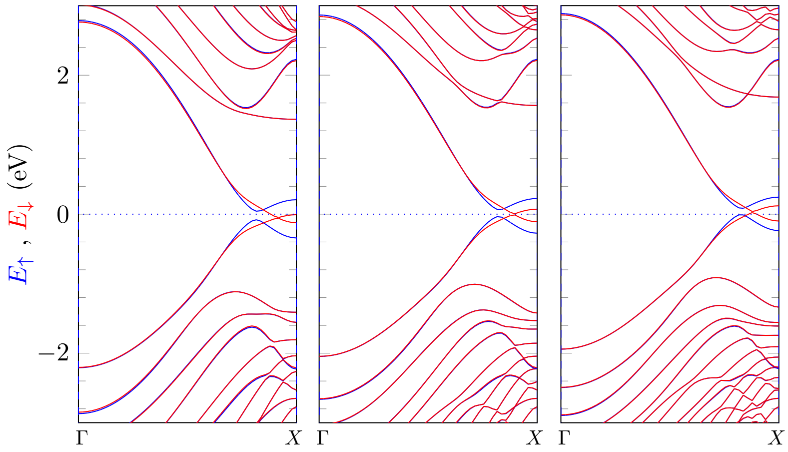

Figure 4.16: mBN/6G/mBN band structures for $m = 5$(left), 7(center) and 9(right), using the same TB and fitting parameters.

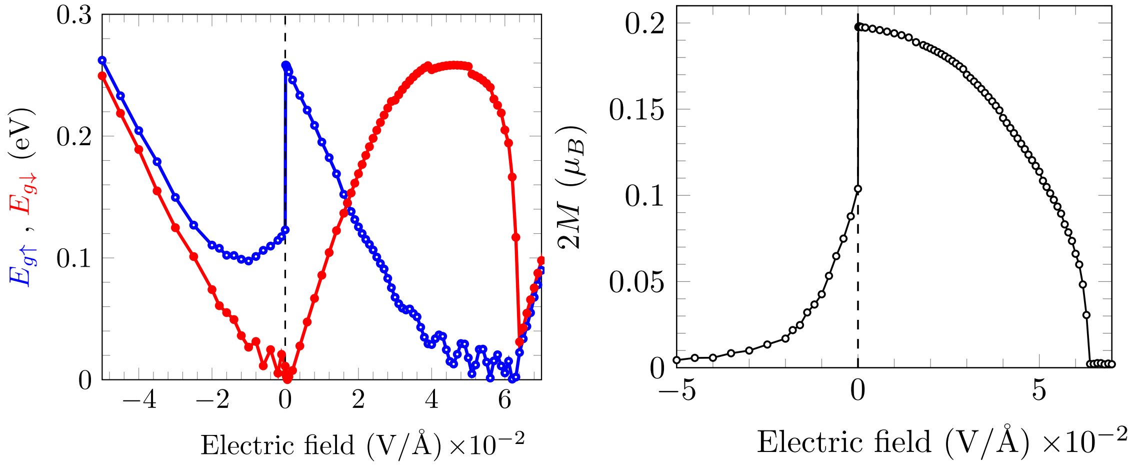

Figure 4.17: **(a)** Spin-dependent bandgap and **(b)** magnetization at the left and right graphene interfaces of a hybrid system as a function of an external field applied in the transverse direction of a 5BN/6G/5BN nanoribbon.

4.3 TB and fitting parameters considerations

In this section we analyze the role of some parameters on the electronic band structures. Different approaches are considered to obtain the TB parameters and contributions from the edges and interfaces. Such approaches avoid the use of edge and interface potentials, which result in the band structure shown in Fig.4.15(b), but correcting the hopping energy values at the edges [6, 115] due to a relaxation on the B-N bondings at the edge atoms. We proposed a similar approach for the interfaces hoppings N/C and C/B in the hybrid system. Fig.4.15(c) and (d) exhibit band structures for decreasing t_{CN} and t_{BN} values, and as a result, the bandgap decreases to reach similar DFT bandgap results. This approach can be combined with on-site energy corrections at the interfaces, in a similar fashion to Zhao *et. al.*[116], which proposed energy corrections to the on-site energies of edge atoms in ZBNNRs, in order to reproduce DFT band structures. They consider a positive energy correction at atoms at one edge, and a negative energy correction at atoms at the other edge of the ZBNNR. This approach mimics the potential induced by the ionized B and N edges in a ZBNNR. However, for the hybrid systems we study, this approach leads into nonphysical interface-hopping values tending to zero and very high on-site energy corrections at carbon atoms in the interfaces. Note that in the limit of zero hoppings at the interface, the graphene stripe would be isolated (unconnected) from the ZBNNRs, giving rise to the characteristic zero-energy edge states of a ZGNR. However, we chose more reasonable hopping values, in agreement with the literature for similar systems[18].

It turns out that the correction on the on-site energies at every site, when modeled by an interface potential, also plays an important role not only at the degeneracy point at $ka = \pi$, but also defines the bandgap as it decreases when the intensity of interface potential, P_G, increases. Therefore, we chose an appropriate value of P_G to narrow the bandgap, in an attempt to reproduce DFT results.

Also, according to Eq.4.6, each one of the on-site corrections considered for the edge atoms reaches their maximum absolute values for wider graphene stripes. On the other hand, with a similar argument presented in Sub-sec.3.2.3.1, higher values of edge potentials at each interface lead to a a closing bandgap for one spin. Consequently, ZGNRs with wider widths would present a trend of a closing bandgap for one spin channel, and a semiconductor gap for the other spin channel. Fig.4.13 illustrate clearly this trend. Even longer graphene stripes embedded in short ZBNNRs show the trend, and present a half-metallic behavior, in agreement with DFT results (see Fig.4.10(bottom)). Therefore, the absence of interface and edge potentials in the theoretical model leads to an opening of the bandgap of the hybrid system and the absence of half-metallicity, as shown in the studies presented in Fig.4.15(c,d,e,f), where we do not consider neither the edge nor interface potentials, or one of them, respectively.

It is important to remark that we did not include electronic correlation on B and N atoms due to the spin-unpolarized nature of ZBNNRs. We only include a non zero Hubbard term for carbon electrons with an optimal value for U_C. Higher U_C values shifts positively the k-position of the spin-down bandgap, as shown in Fig.4.15(g). It also breaks the spin degeneracy of other bands, in disagreement with DFT results. Conversely, Fig.4.15(h) shows the band structure of the hybrid system when no electronic correlation is present.

Attempts to find the optimal TB parameters without the use of interface potentials, but just hopping and on-site energy values adjustments, works well for a specific hybrid nanoribbon width. However, interface potentials provided a more robust scenario for the use of the same set of TB parameter values. Fig.4.16 shows the same half-metallic behavior, even for wider boron-nitride regions by considering increasing values of m in the hybrid mBN/6G/mBN system (m=5, 7, and 9).

The interface potential proposed here is the optimal one which mimics the intrinsic electric field with a critical value that leads into a half-metallic hybrid system.

$\varepsilon_C^{(0)}$	$\varepsilon_B^{(0)}$	$\varepsilon_N^{(0)}$	t_{CC}	t_{CB}	t_{CN}	t_{BN}	U_C	U_B	U_N
0.0	2.76	−1.64	−2.65	−2.25	1.70	−2.40	0	0	0

Table 4.4: TB parameters for armchair mBN/nG/mBN nanoribbon systems. Units are given in eV. Taken from Ref.[18].

When adding a negative external electric field, the bandgap for the up channel decreases rapidly, while the bandgap for the down channel widens. For increasing negative electric fields, the bandgaps for spin channels up and down eventually equal each other, as shown in 4.17(a). This response resembles that of a ZGNR around a critical electric field value where the system reaches the half-metallic stage[33, 117]. In our hybrid system, the critical electric field is played by the intrinsic field induced by the ZBNNRs. Therefore, adding an external electric field breaks the half-metallic behavior. This response is in agreement with DFT results from Bohwmick *et al*[15] shown in Fig.4.12. Positive electric field values added to the hybrid system also remove the half-metallic response. However, for enough high values of electric field, our TB model predicts that the hybrid nanoribbon turns again into a half-metallic system. After this point, the system becomes a nonmagnetic semiconductor for both spin channels. Additionally, consider Fig.4.17(b) where the system exhibits a magnetization quenching for negative electric fields. This response also resembles the magnetization response of a ZGNR in the neighborhood of a critical value of an external transverse electric field[117, 118]. Moreover, increasing positively the external field leads to a second magnetization quenching.

4.4 Armchair hybrid system

Differently from the systems with zigzag edges studied in previous sections, the TB band structures of ABNNRs fits well with DFT results without energy corrections as edge potentials. This is because each edge is composed of both boron and nitrogen atoms, leading to an average non-ionized edge. Also, Sasaki *et. al.* [119] explain the absence of pseudospin polarization in terms of a gauge field for the edge states.

To calculate transport properties of armchair hybrid systems, we use the TB parameters provided in the literature [18], shown in Table 4.4. Our models are the armchair unit cells displayed in Fig.4.18(a-d). Begining with a pristine ABNNR, carbon dimers replaces B and N atoms, maintaining constant the width of the hybrid system to 17 dimers. The

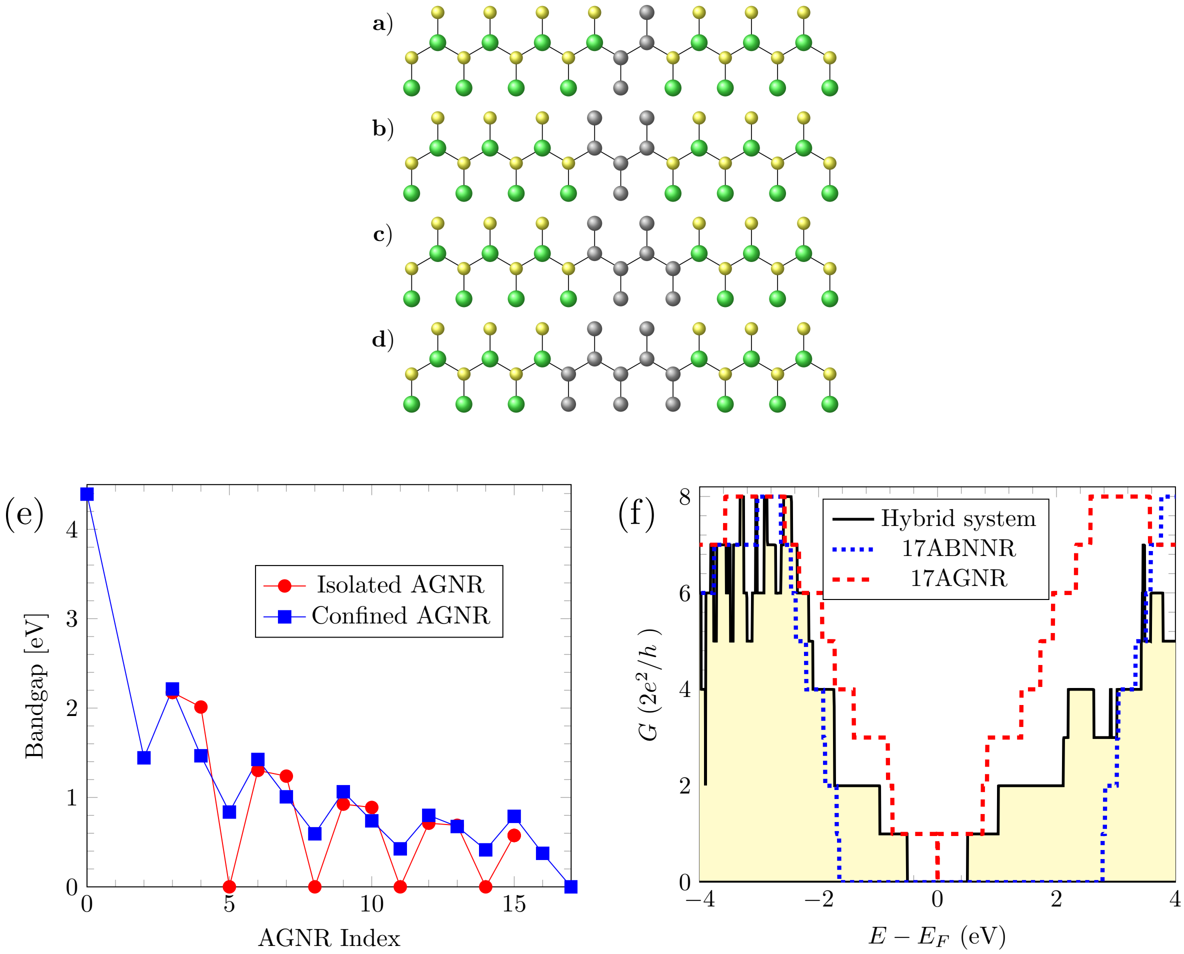

Figure 4.18: (a-d) Unit cells of different hybrid armchair nanoribbons. The ribbon axis is parallel to the armchair edge. (a) 8BN/2G/7BN, (b)7BN/3G/7BN, (c) 7BN/4G/6BN, (d) 6BN/5G/6BN. (e) Bandgap behavior of an isolated AGNR (red marks) and an AGNR being part of a 17-dimer-hybrid system (blue marks). (f) Conductace of the hybrid armchair 5BN/7G/5BN, 17ABNNR and 17AGNR.

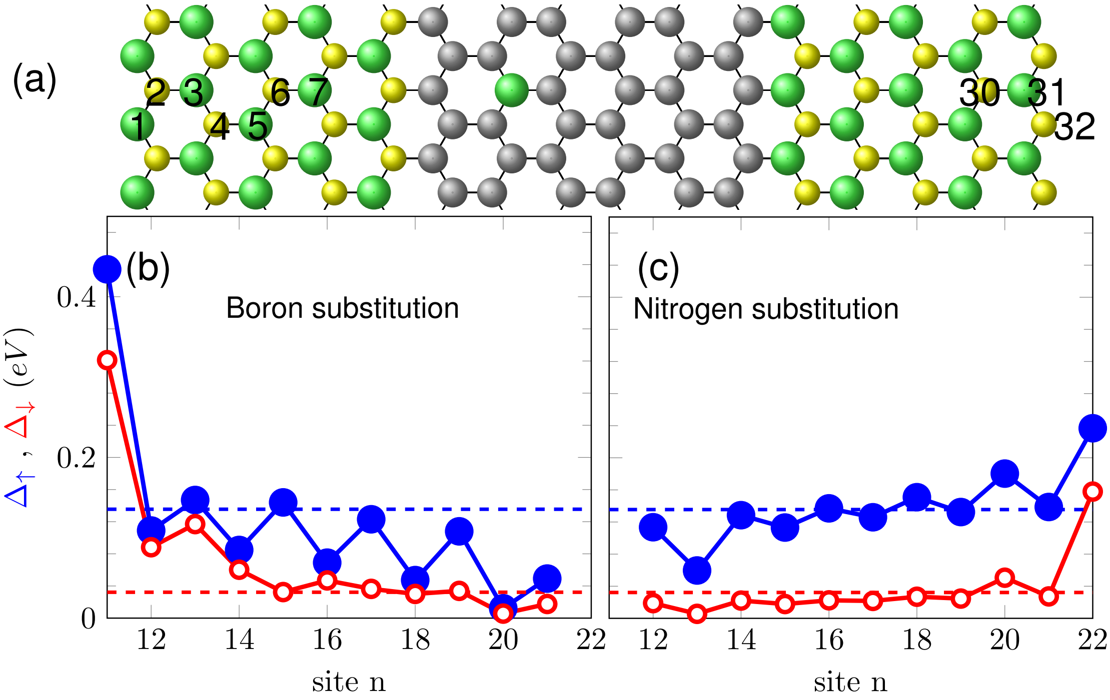

Figure 4.19: (a) Hybrid 5BN/6G/5BN nanoribbon with a boron atom diffusing trough the graphene stripe. Green, yellow, and gray balls represent boron, nitrogen, and carbon atoms, respectively. Bandgap dependence with respect to boron (b) or nitrogen (c) substitutions along the graphene ribbon in the unit cell. Zigzag edges are parallel to vertical direction

center part of Fig.4.18 shows the bandgap evolution of hybrid systems with respect to the AGNR width. For comparison, bandgap evolution of pristine AGNRs with respect to its width is superposed. For the calculations, the hopping at the isolated edges were decreased in a 12% with respect to the hoppings in the bulk material due to edge relaxation [6, 115]. The armchair hybrids show a similar bandgap behavior as their pristine counterpart, and can be categorized in $3m$, $3m+1$, and $3m+2$ families, all of them semiconductors when edge hopping relaxation is considered. The right part of Fig.4.18 exhibits the conductivity of pristine 17-AGNR and 17-ABNNR. Hybrid systems show a intermediate bandgap between the pristine AGNR and ABNNRs, as illustrated in Fig.4.18(right).

4.5 Effect of impurities

To describe more realistic systems we also study roughness and a less sharped zigzag interface. Also, we considere atom diffusion from the BN region to the graphene interface[120]. We model this roughness by substituting carbon atoms by boron or nitrogen atoms in ev-

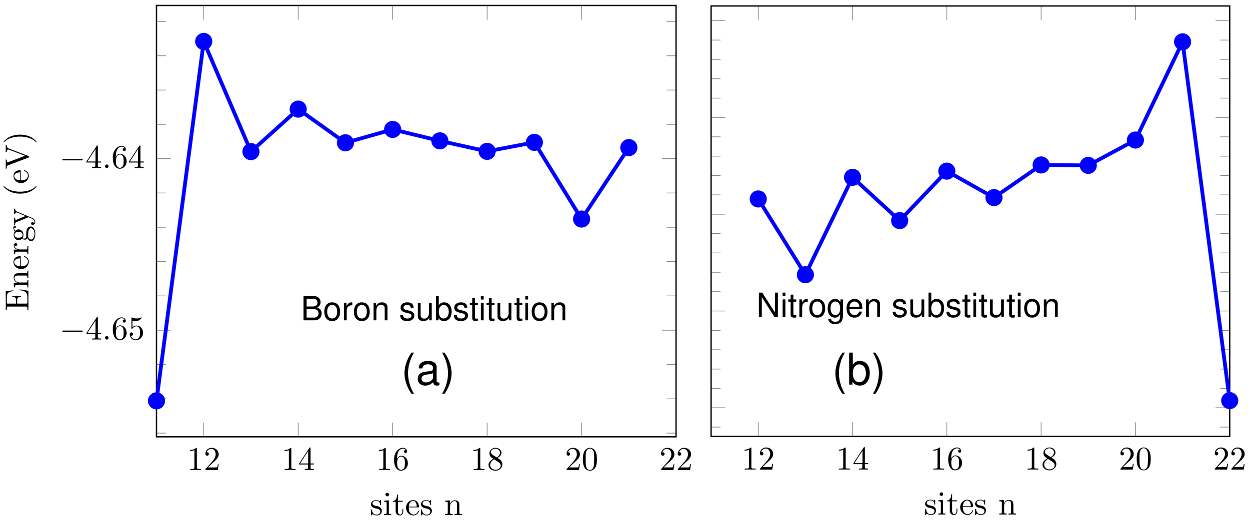

Figure 4.20: Total energy per unit cell when a boron (left) or nitrogen (right) atom substitutes a carbon atom in the hybrid system. The energy of the pristine system is −4.67 eV/unit cell.

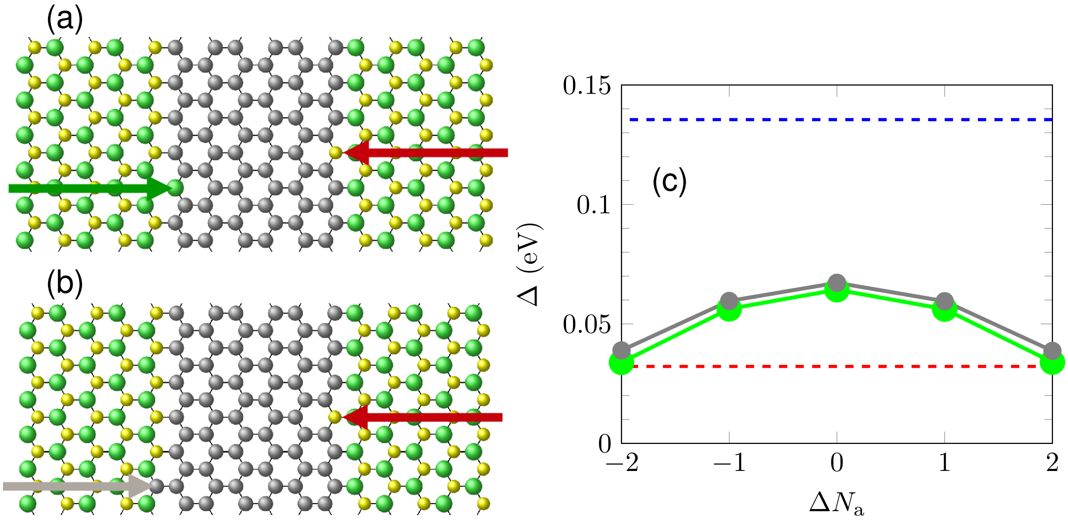

Figure 4.21: Gap dependence with respect to the relative position of two substitutional impurities at the graphene stripe. For $\triangle N_a = 0$, the two impurities belong to the same (n-th relative) armchair chain. The green(gray) line corresponds to a N-B (N-C) configuration near the two interfaces. Dashed lines are the bandgap up(blue) and down(red) for the pristine case.

ery periodic unit cell. Spontaneous magnetization in ZBNNRs doped with carbon atoms in substitutional positions in the lattices has been reported [121]. The understanding of the effects of such lattice imperfections on the electronic properties may improve the controlled electronic responses of those nanostructured materials.

Departing from the pristine configuration to treat a more realistic system with roughness at the interfaces will demand a high DFT computational cost. To overcome this difficulty, we use the TB model with the parameters and fitting curves we have found for the hybrid system. With this approach we can study larger nanoribbons engineer hybrid systems' bandgaps with a less computationally cost compared with DFT calculations.

We consider a system with a unit cell shown in Fig.4.19(a). Here, a boron (nitrogen) atom replaces a carbon atom, and we analyze the gap evolution Fig. 4.19.b(c) with respect to the substitution at the n-th site. Substituions at the interfaces h-BN/graphene increases the bandgap for channels up and down. We also obtain a diminishing gap trend and an enhancement of the half-metallic response when the impurity substitution is verified at the center of the graphene stripe. Boron and nitrogen impurities substitution exhibit, as expected, opposite trends for the bandgap behavior as a function of the impurity position along the graphene material.

Using our TB parameters with edge and interface potentials, we calculate the total energy of the system when a boron atom substitutes a carbon atom in the graphene stripe, as shown in Fig.4.20(left). We also include the results corresponding to the case when a carbon atom is substituted by a nitrogen atom. The curves indicate the preference for a boron subsituting a carbon atom at the interface, where it is bonded with a nitrogen atom. A similar behavior happens for the nitrogen substitution on the other edge. Our calculations are preliminar results that should be compared to DFT results. Work along this line is in progress.

We study further the effects of interaction between impurities at opposite interfaces. For a fixed nitrogen position inside the graphene stripe (marked with a red arrow in Figs.4.21 (a) and (b)), we vary the position of a boron and a carbon atom at the opposite BN/graphene interface (marked with green and gray arrows, respectively). The results Fig.4.21(c) shows maximum bandgap when impurities are located in the same armchair chain, located at opposite positions in the two interfaces.

4.6 Final considerations

In this chapter, we proposed and discussed the inclussion of an interface potential to explain the effects of a h-BN/graphene zigzag interface in a 2-dimensional hybrid system. Because of the ionic nature of B and N atoms, the h-BN/graphene interface works as an effective linear arrangement of electronic charges. Depending on the h-BN atoms at the interface, the effective accumulation of electronic charges causes a positive or negative potential, modifying the on-site energy values in the graphene region. Particularly, a ZGNR embedded in a pair of ZBNNRs shows a half-metallic response as if it were submerged in an intrinsic electric field generated by the ZBNNRs. This TB approach is used along with edge potentials to better explain the main features of DFT band structure results. The use of interface and edge potentials can contribute to explain the electronic properties of hybrid systems with defects and impurities, which, in the DFT, lead to time-consuming calculations.

5

Strain in nanoribbons

Since the original prediction by Fujita et al. [7], edge states in pristine graphene have been heralded as ideal ballistic channels with potential in electronic applications. To better understand the nature of these states, Sasaki et al. [8] studied the effects of a highly localized strain defect along different crystal directions (modeled by a δ-function gauge field in a Dirac model). The analytic solution showed the emergence of states along the zigzag direction with properties similar to those of edge states: pseudospin polarization, i.e., local sublattice symmetry breaking, and same flat band dispersion, but localized at the position of the deformation. These characteristics are well understood in terms of the effective pseudomagnetic field generated by the deformation[37, 38].

Here we show that longitudinal out-of-plane deformations along a graphene membrane generate extra conductance channels running parallel to the structure with the remarkable property of being valley polarized. As a consequence, a current injected parallel to the axis of the deformation will naturally split in space, with states from one valley running along the crest while states of the other valley run along the sides. These results [16] point towards a realistic implementation of valley polarized channels that can be achieved in current experimental settings by appropriate design of substrates or sample preparation.

This chapter is organized in the following sequence: first, we describe the hamiltonian of a deformed ZGNR in the framework of continuum elasticity theory, and the pseudomagnetic field due to the strain. Second, we study the effects of strain on the electronic and transport properties of ZGNRs. Finally, electronic correlation is added to the model to study the effects on the half-metallic response.

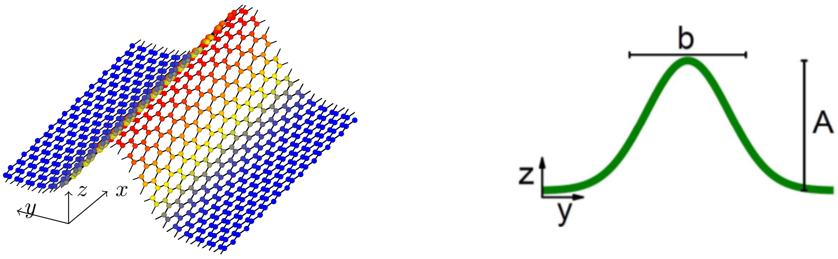

Figure 5.1: Left: Folded graphene nanoribbon. Colors indicate increasing height values along the z-axis. The system is periodic along the x-direction (zigzag edge). Right: Folding parameters, A and b, of the Gaussian function.

5.1 Model

Here we study a graphene nanoribbon under a Gaussian out-of plane strain (see Fig.5.1). If the edges of the nanoribbon are parallel to the x-axis, then we model a deformation centered at the nanoribbon axis and parallel to the edges according to the function

$$h(y) = A \exp(-(y/b)^2), \tag{5.1}$$

where $h(y_i)$ and y_i are the height and position along the unit cell of the i-th site, respectively. The deformation is then, characterized by the parameters A and b, describing the amplitude and extent of the deformation, respectively.

We use the TB model to study the effects of the deformation on the nanoribbon,

$$H = \sum_{\langle ij \rangle} t_{ij}(c_j^\dagger c_i + c_i^\dagger c_j), \tag{5.2}$$

the hopping parameter between the i-th and j-th atoms, t_{ij} (first nearest neighbors), depends on the value of the carbon-carbon distance l_{ij} according to

$$t_{ij} = t \exp\left(-\beta \left(\frac{l_{ij}}{d} - 1\right)\right), \tag{5.3}$$

where t and d are the hopping energy and carbon-carbon distance in the absence of strain. Here $t = 2.8\,\mathrm{eV}$, $d = 1.42\,\text{Å}$, and $\beta = \left|\frac{\partial \ln(t_0)}{\partial \ln(d)}\right| \simeq 3$[41, 122]. The variation in the hopping energy is due to the change in the superposition of π orbitals when the carbon-carbon distance is altered. In the linear elasticity theory framework[123, 124], the variation in the carbon-carbon distance is calculated in terms of the strain tensor,

$$\varepsilon_{\mu\nu} = \frac{1}{2}(\partial_\nu u_\mu + \partial_\mu u_\nu + \partial_\mu h \partial_\nu h), \tag{5.4}$$

where u_μ and h are the in-plane and out-of plane deformations, respectively. The carbon-carbon distance departs from d according to

$$l_{ij} = d + \varepsilon_{xx}\frac{x_{ij}^2}{d} + \varepsilon_{yy}\frac{y_{ij}^2}{d} + 2\varepsilon_{xy}\frac{x_{ij}y_{ij}}{d}, \tag{5.5}$$

where x_{ij} and y_{ij} are the projections of d over the x-axis and y-axis, respectively. In last equation, only the components of the strain tensor account for the deformation. x_{ij}, y_{ij} and d are measured when in the absence of strain. For a Gaussian deformation depending only on the y coordinate, the components of the strain tensor are null, except for the yy-component, i.e.,

$$\varepsilon_{yy} = \frac{1}{2}\partial_y h \partial_y h, \tag{5.6}$$

and consequently, the carbon-carbon distance becomes,

$$l_{ij} = d + \varepsilon_{yy}\frac{y_{ij}^2}{d}, \tag{5.7}$$

which can take its maximum value for a bonding parallel to the y-direction. The effect of strain is then maximized for zigzag nanoribbons with edges parallel to the Gaussian axis, in the configuration shown in Fig.5.1.

5.2 Pseudomagnetic field

In the neighborhood of the K valley, the hamiltonian of graphene approximates to the Dirac equation,

$$H_k = v_F \vec{\sigma} \cdot \vec{p}. \tag{5.8}$$

where v_F is the Fermi velocity and σ's are the Pauli matrices.

When the honeycomb lattice suffers strain, the geometry of the deformation can be mapped into the Dirac equation for graphene as[119, 125],

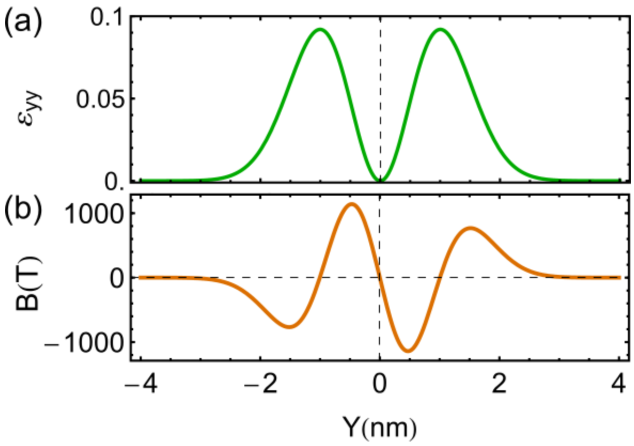

Figure 5.2: (a) Strain distribution and (b) pseudomagnetic field in the valley K in a ZGNR under the effects of a gaussian strain with parameters $A = 5d = 0.7\,\text{nm}$ and $b = 10d = 1.4\,\text{nm}$.

$$H_K = v_F \sigma \cdot (\vec{p} + \vec{A}(r)), \tag{5.9}$$

where **A** can be interpreted as a pseudomagnetic vector potential, and depends on the variations of the bonding distances with respect to the case with no strain. It can be demonstrated that [126]

$$\begin{pmatrix} A_x \\ A_y \end{pmatrix} = \begin{pmatrix} \varepsilon_{xx} - \varepsilon_{yy} \\ -2\varepsilon_{xy} \end{pmatrix} = \begin{pmatrix} -2(y^2/b^4)h^2 \\ 0 \end{pmatrix}, \tag{5.10}$$

and the pseudomagnetic field is calculated as $\vec{B} = \vec{\nabla} \times \vec{A}$.

From the Gaussian function 5.1, it can be shown that the maximum strain is located at $y_m = \pm b$, and from here we get that the maximum strain intensity $\varepsilon_m = \alpha^2/e$, with $e = 2.71828...$ and $\alpha = A/b$.

Fig.5.2 shows the strain distribution along the ZGNR, and the pseudomagnetic field for the valley K. Notice that the pseudomagnetic field inverts signal for the valley K' as can directly be shown by means of the Dirac equation for the valley K'. It is also interesting to notice the change of sign of the pseudomagnetic field that happens along the confinemet direction of the ZGNR.

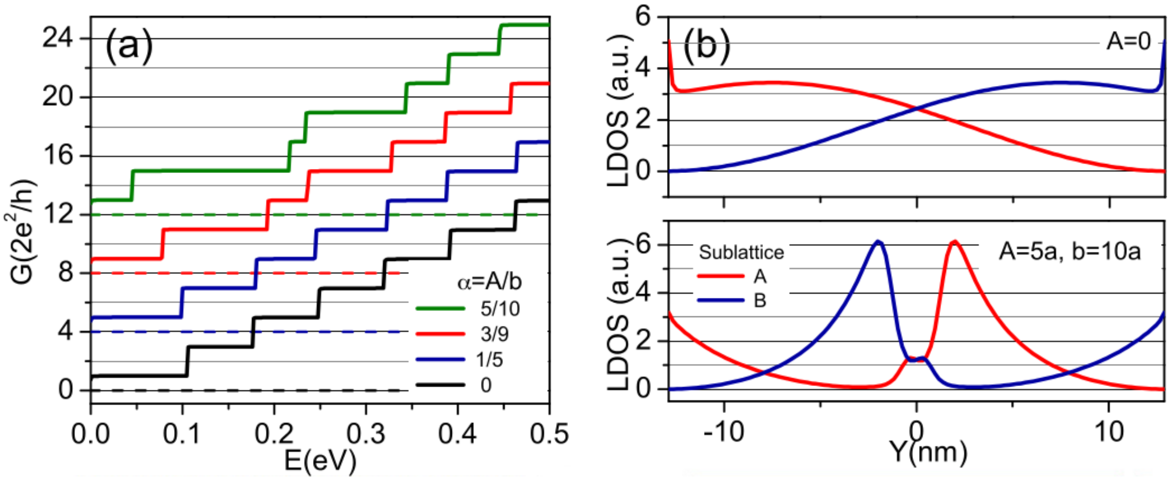

Figure 5.3: (a) Conductance for ribbon (width $W = 25.8\,\text{nm}$) with different strained folds parameters. Curves are shifted for clarity. Dashed horizontal lines mark zero value for proper comparison. (b) LDOS profile across the ribbon with upper/lower panels showing results for: $\varepsilon_m = 0\% - 9.2\%$ [black to green curves in (a)].

5.3 Effects of strain on the electronic properties

In Fig. 5.3 we show the conductance results for ZGNRs under no strain, $\varepsilon_m = 0$ (black line), and also for increasing values. For $\varepsilon_m = 0$, the first conductance plateau represents two ballistic channels (one per spin) due to edge states in the zero energy band while the second plateau contains six channels. As strain increases, the onset of the second conductance plateau moves to lower energies and becomes wider. The increase in width is produced by spectral transfer from other energies, and its onset at lower energies represents an effective increase in the conductance. The number of channels contributing to the conductance within the energy range of the first plateau in the unstrained ribbon (energies below 0.1 eV in Fig.5.4 (c) increases with strain from two to six (with four channels added to the existing two). Fig.5.3(b) shows two LDOS profiles across the ribbon at the energy $E = 0.05\,\text{eV}$, with the upper/lower panels showing results for ribbons with $\varepsilon_m = 0$ and $\varepsilon_m = 9.2\%$. An enhanced LDOS develops around the deformed region with a similar spatial distribution to the exhibited by the pseudomagnetic field (see Fig.5.2(b)). The increase in LDOS at the edges corresponds to edge states. A and B curves denote the two graphene nanoribbon sublattices.

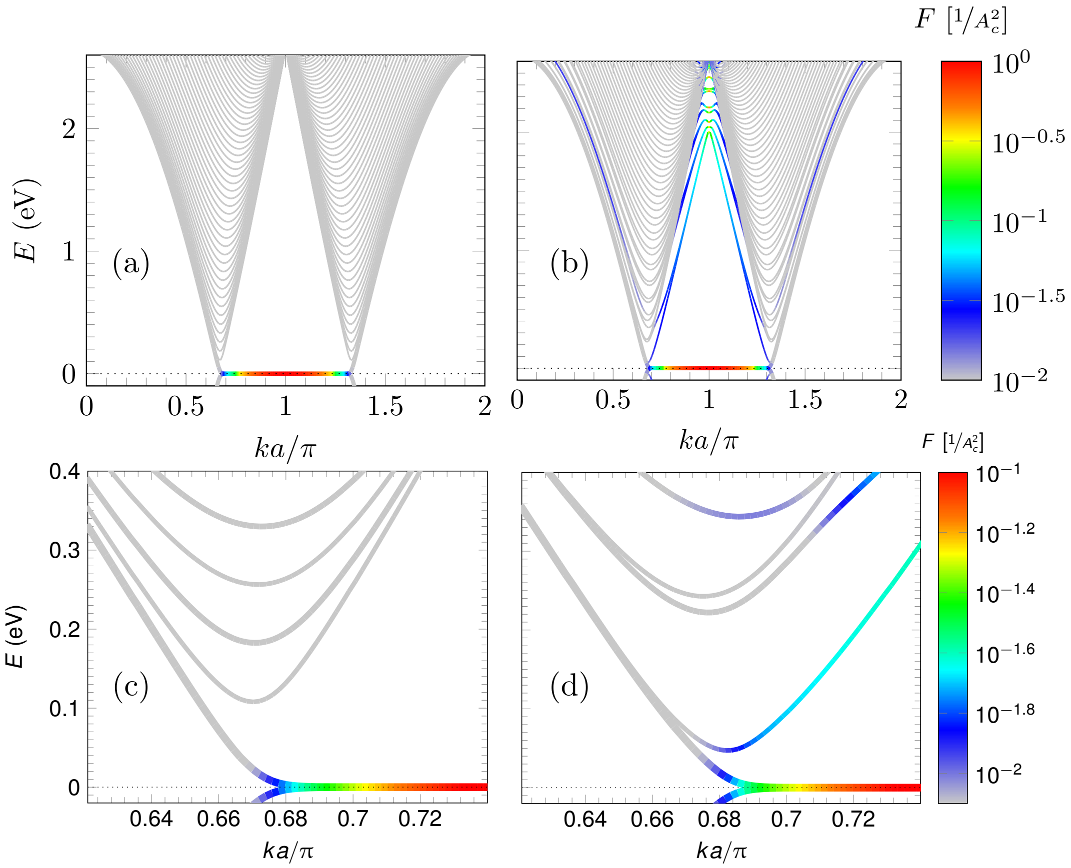

Figure 5.4: Band structure of a 112-ZGNR. Undeformed nanoribbon (a) is compared to the strained nanoribbon (b) with folding parameters $A = 5d = 0.7\,\text{nm}$ and $b = 10d = 1.4\,\text{nm}$. (c) and (d) shows a zoom of the band structures from (a) and (b), respectively. Colored lines represent the degree of F-electronic localization [16].

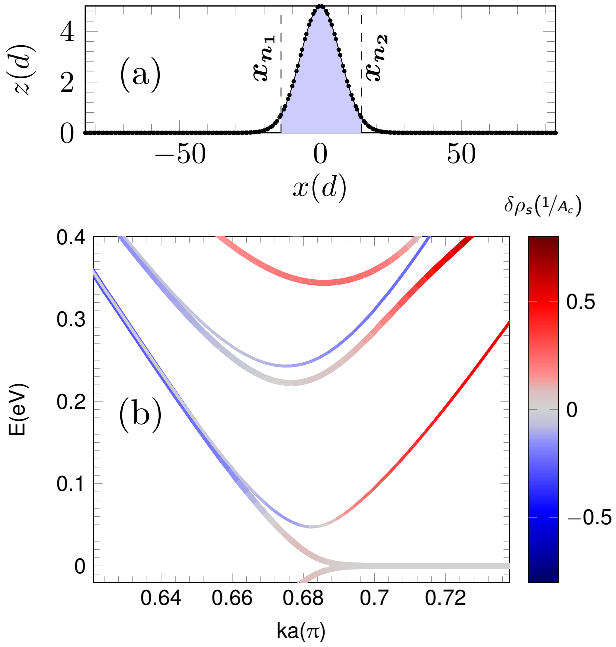

Figure 5.5: (a) Profile of a ZGNR under a folded strain with parameters $(A, b) = (5d, 10d)$. (b) Band structure of a 112-ZGNR under strain. Colored lines indicate the accumulation of charge in the central region between x_{n1} and x_{n2}.

5.3.1 Effects on the band structure

Now we analyze the electronic band structure of a 112-ZGNR to study the effects of such folded-like deformation. When no deformation is present, the hamiltonian for a N-ZGNR of the zigzag nanoribbon, at $ka = \pi$, is

$$H(ka=\pi)=\begin{pmatrix} [\varepsilon_0] & 0 & 0 & & & & 0\\ 0 & \varepsilon_0 & t & 0 & & & \\ 0 & t & \varepsilon_0 & 0 & & & \\ & 0 & 0 & \ddots & 0 & 0 & \\ & & & 0 & \varepsilon_0 & t & 0\\ & & & 0 & t & \varepsilon_0 & 0\\ 0 & & & & 0 & 0 & [\varepsilon_0] \end{pmatrix}, \tag{5.11}$$

with eigenvalues $E_m = \varepsilon_0 \pm t$ for $m = 2, ..., N-1$ leading to degenerate states as shown Fig.5.4(a). However, the degeneracy is lifted when the hopping energy values suffer a perturbation such as the folded deformation, as displayed in Fig.5.4(b). In this figure the strain parameters considered, A and b, lead to $\alpha^2 = 25\%$ that corresponds to a maximum strain of $\varepsilon_m = 9.2\%$. The strain also affects the bands near the Dirac point in the band structure diagram. Additionally, we verify a positive shift of the Dirac cone position at K for increasing stress, and a negative shift for the Dirac cone position at K'.

Strain causes a rearrangement of charge through the nanoribbon, as can be deduced from the degree of localization shown in the same figure. Here we use the definition of Zheng *et al*[13] for the F-localization, given in Eq.2.66. F is defined as a sum of the 4th powers of the wavefunction's probability coefficients, and it is summed over all the sites of our ZGNR unit cell. On one hand, delocalized electrons can be represented by a wavefunction with equal coefficients. A straightforward calculation would allow us to determine that F reaches the minimum value for our system. On the other hand, F can reach the maximum value, equal to one, when electrons are completely localized in only one site. This is the case for states from the zero energy band at $ka = \pi$ which are more electronically localized than those states near the Dirac point. Therefore, F is a number that provides us the localization signature of an electronic state. Lastly, not only F allows us a rapid search of states with localization in an energy-momentum diagram, but also it can be used as a way to compare the level of localization between different bands. For example, Fig.5.4(c) and (d) show the band structure of the same ZGNR in the neighborhood of the Dirac cone, before and after applying the strain. The result show that strain causes localization for high energy bands.

In order to determine the real position of the localized states with respect to the folded strain, we can define $\delta\rho_s$ as a sum of the squares of the wavefunction's probability coefficients, with the sum running over the sites belonging to the folding range. This sum is compared to the case when there is no folding $\varepsilon_m = 0$ over the same range,

$$\delta\rho_s \equiv \sum_i \left| c_i^{(\varepsilon)} \right|^2 - \sum_i \left| c_i^{(\varepsilon=0)} \right|^2 , \tag{5.12}$$

where c_i is the wave function amplitude at the i-th site (the wavefunction can be written in terms of orbitals centered at each site as $\Psi_{nk}(\vec{r}) = \sum_{i=1}^{N} c_i \phi(\vec{r} - \vec{R}_i)$). The sum in Eq.5.12 is calculated adding contributions from i-th sites around the strained region if the condition $h(y_i) \geq 0.01$ Å is satisfied. Roughly speaking, $\delta\rho_s$ help us to define where the localization is present, and whether or not the charge accumulation is due to the fold strain or due to edge states, for example. In an energy-momentum diagram, the color code would indicate which bands show an increase/decrease in the probability density (red/blue) in the fold structure. Fig.5.5 identifies the states where charge accumulates or decreases in the folded region, and we can identify that the high energy bands are localized inside the folded deformation.

5.3.2 Effects on the LDOS

The real space distribution of the localized states can be further analyzed by means of the probability density, $|c_i|^2$ with $i = 1, \ldots, 2N$ for a N-ZGNR. Figs.5.6(a) and (b) show the probability density at an energy $E = 0.15\,\mathrm{eV}$ for valleys K and K', respectively. Blue (red) symbols indicate a positive (negative) group velocity ($v \propto \partial E/\partial k$).

The states, labeled by k_1 and k_2 , are located at symmetric positions around both Dirac points (red and blue) as shown in panel (c). Full and empty symbols correspond to sub-lattice A and B, respectively. The color scale represents values of the pseudomagnetic field at each valley, as depicted in the bottom part of the panel.

Fig.5.6(c) shows the band structures in the neighborhood of valleys K and K'. For the valley K, two states with $E = 0.15\,\mathrm{eV}$ contributes to the LDOS with positive phase velocity, while just one state contributes to the LDOS with negative phase velocity. Valley K' mirrors the results for valley K.

Fig.5.6(d) shows the LDOS through the transverse direction of the ZGNR (across the strained fold) obtained by adding up all states at energy $E = 0.15\,\mathrm{eV}$ with the same group velocity, from both valleys K and K'. Mathematically,

$$s_{i_{A(B)}} \equiv \sum_{v>0,\, K'} \left| c_{i_{A(B)}} \right|^2 + \sum_{v>0,\, K} \left| c_{i_{A(B)}} \right|^2 . \tag{5.13}$$

Notice that two states with positive group velocity from valley K' (see Fig.5.6.c) contribute to the sum. We also add a bar color to identify if the main contribution comes from the valley K or valley K' by using the following rate,

$$r_{i_{A(B)}} \equiv \frac{\sum_{v>0,\, K'} \left| c_{i_{A(B)}} \right|^2 - \sum_{v>0,\, K} \left| c_{i_{A(B)}} \right|^2}{s_{i_{A(B)}}} . \tag{5.14}$$

Therefore, Fig.5.6(d) identifies the valley separation: LDOS for states from valley K is enhanced at the center (larger values of pseudomagnetic field) while that from valley K' is larger at the sides. We have obtained similar results for different ribbon sizes and strain values. This valley filtering is enhanced for larger pseudomagnetic field values (the maximum value of the pseudomagnetic field is $B_{pm} \propto \varepsilon_m/b$) and it can be modulated by narrowing the rate b/W (W is the nanoribbon width) with the same fixed strain ε_m.

We have then shown that for folded like ZGNRs states with the same velocity show real space valley polarization, i.e., a current injected along the deformed structure will

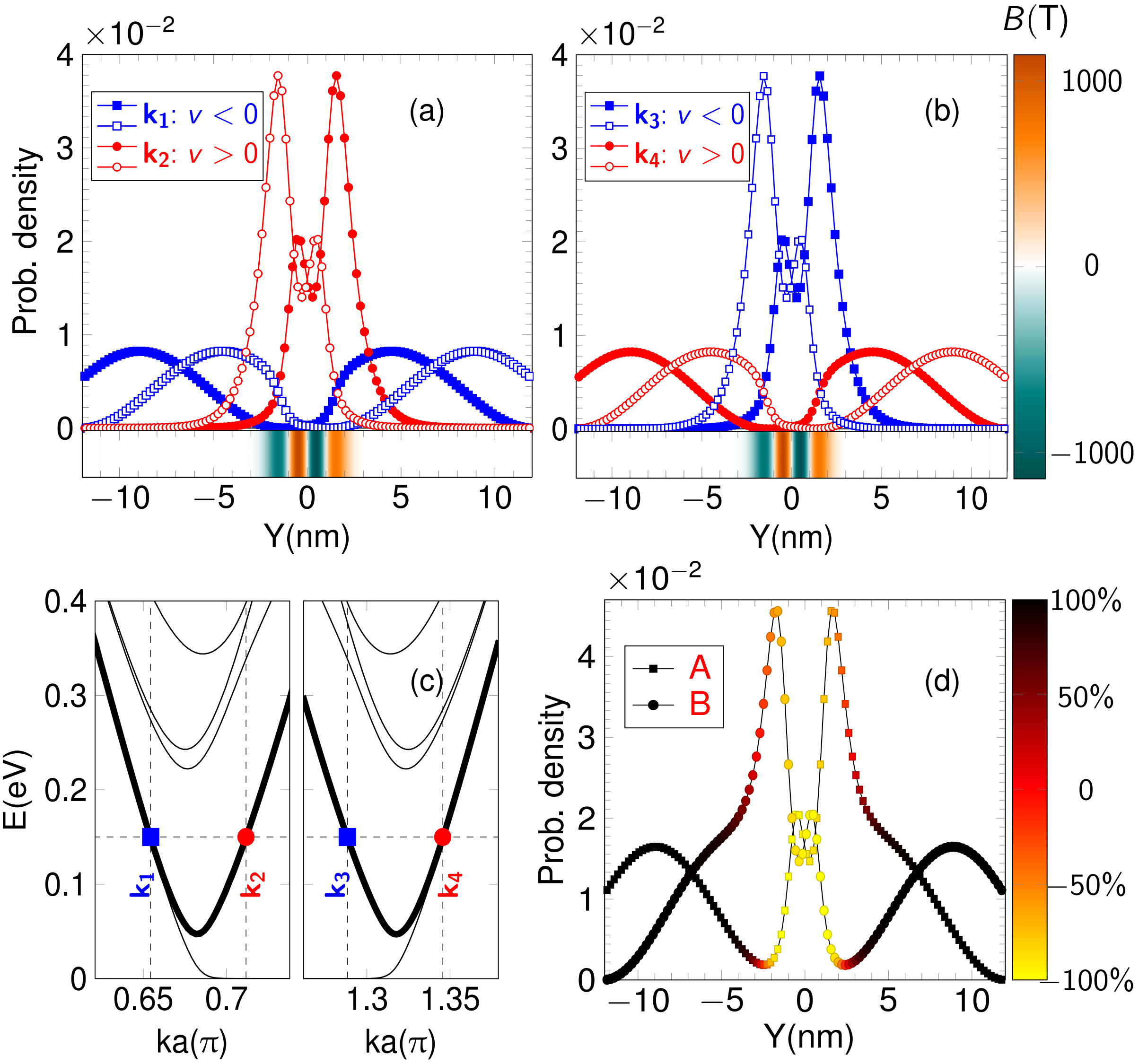

Figure 5.6: Probability densities for states at energy $E = 0.15\,\text{eV}$. Blue (red) curves correspond to state k_1 (k_2) with negative (positive) velocity. Filled (empty) symbols indicate sub-lattice A (B). (a) States near Dirac point K. (b) States near Dirac point K'. Color scale indicates magnitude of pseudomagnetic field (bottom). (c) Position of states in band structure: right K and left K', respectively. (d) Total LDOS with states from both valleys with same velocity. Color scale indicates location in band structure: yellow near K and black near K'. Results for a 112-ZGNR (width $W = 23.7\,\text{nm}$) and strain parameters $A = 5d = 0.7\,\text{nm}$ and $b = 10d = 1.4\,\text{nm}$ [16].

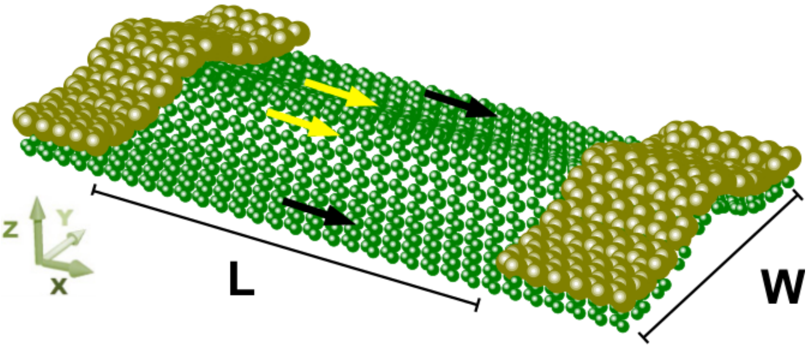

Figure 5.7: Schematic representation of deformed zigzag graphene nanoribbon with a Gaussian fold like out-of plane deformation acting as a valley filter separating the contributions from K and K' valley, marked with yellow and black arrows, respectively.

split into two currents: one along the center of the strained fold constituted by states from one valley, and another running at its sides with contributions from states of the other valley as shown schematically in Fig. 5.7.

5.4 Effects of electronic correlation in strained ZGNRs

We now discuss the effects of taking into account the electronic correlation in the fold-strained zigzag nanoribbon. First, we consider the case in which the ZGNR is under no strain. In the TB model, ZGNRs have a gap-less band structure and a pair of degenerate edge states at the Fermi level. However, electronic repulsion opens a bandgap that depends on the ribbon width[127] as shown in Fig.5.8. The figure exhibits the effects of considering electronic correlation on the band structure of nanoribbon with different widths. For wider nanoribbons, the zero-gap of a graphene sheet is eventually recovered.

When applying a transverse electric field, the degenerate band structure is lifted, and the bandgap evolves with respect to the external electric field as shown in Fig.5.9. Half-metallicity is achieved for a critical value of the electric field, as explained earlier in Sub-sec.3.2.3.1. Fig.5.9 also shows the bandgap oscillations for large electric field values, in agreement with the literature[128]. Additionally, Fig.5.9 exhibits the robustness of the half-metallic response for ZGNRs with large widths.

As discussed in the previous section, strain causes localization in high energy bands. We investigate then if the localization at higher energies can be further enhanced for increasing intensities of electronic correlation. The results are shown in Fig.5.10.

We now show in Fig.5.11 the results for the evolution of the bandgap with respect

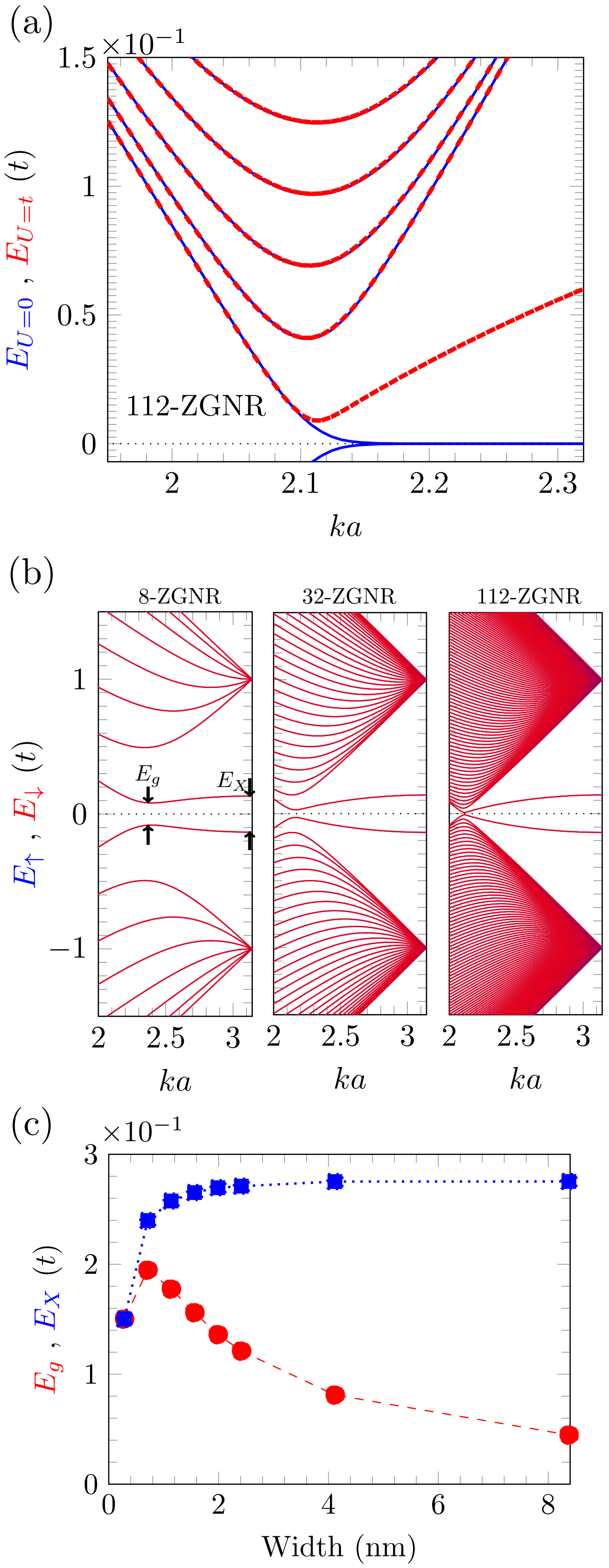

Figure 5.8: **(a)** Electronic band structure of a 112-ZGNR near the Fermi level with (red dashed lines) and without electronic correlation (blue lines). **(b)** 8, 32, and 112-ZGNR spin independent band structures, with $U = t$. E_X and the bandgap E_g are defined here. **(c)** E_X and E_g dependence with respect to the ZGNR width.

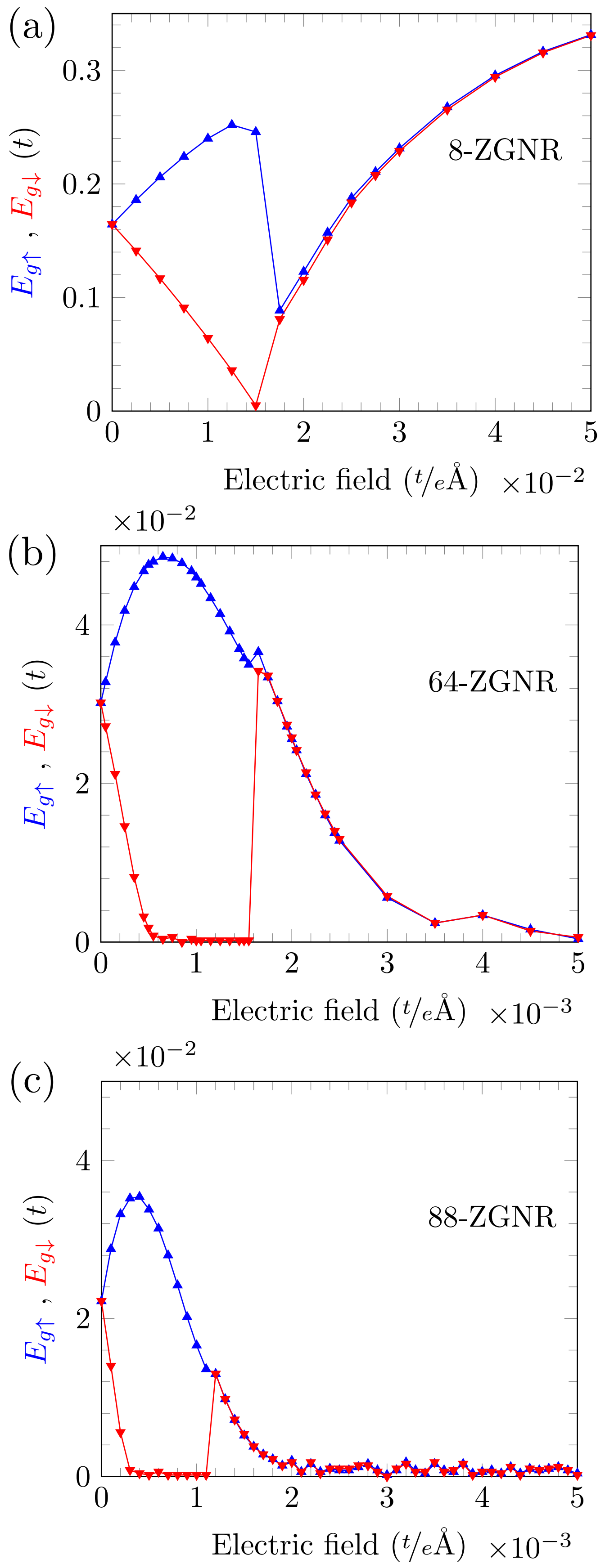

Figure 5.9: Bandgap dependence on a transverse electric field for N-ZGNRs, with N=8 (a), 64 (b), 88 (c), and $U = t$ and zero strain. e is the electron charge.

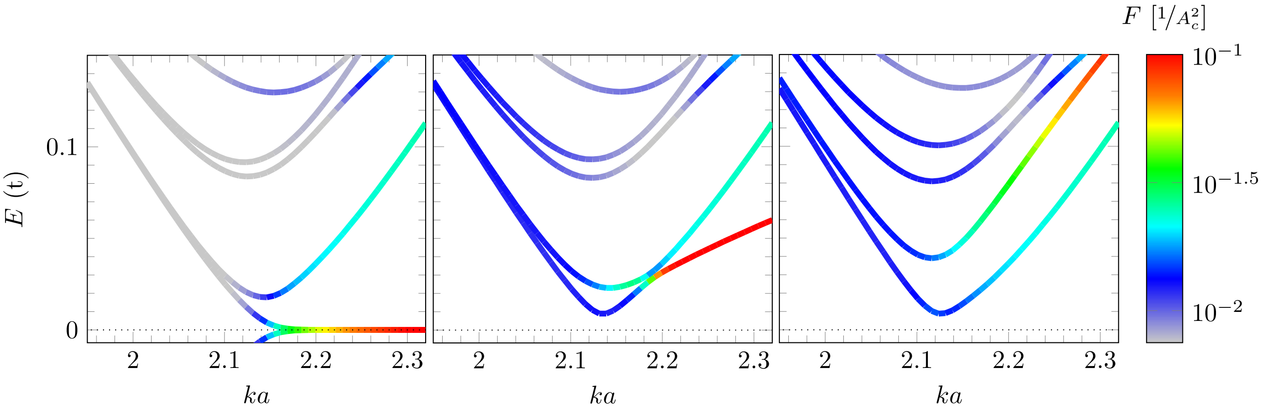

Figure 5.10: 112-ZGNR band structures with strain parameters, $(A, b) = (5d, 10d)$. $U = 0$ (left), $U = t$ (center), and $U = 2t$ (right).

to an external electric field, when both strain and correlations are considered for a 112-ZGNR. In all figures the results for $U = t$ are compared with those corresponding to null correlation ($U = 0$). The large width of the nanoribbon ensures that the strained fold is fully embedded in the system, i.e., $b/W \ll 1$. The figure shows almost no change in the critical electric field value to achieve half-metallicity, even for larger strain intensities, as shown in Fig.5.11(c). Figures (b) and (d) have the same $\alpha^2 = 6\%$ but different A and b parameters, and show almost no modification in the bandgap dependence with respect to the electric field. However, intense strain could lead to a degenerate bandgap even in the presence of smaller external field intensities, as ilustrrated in Fig.5.11(c). In that sense, the strain can be used to taylor the spin-dependence of the gaps.

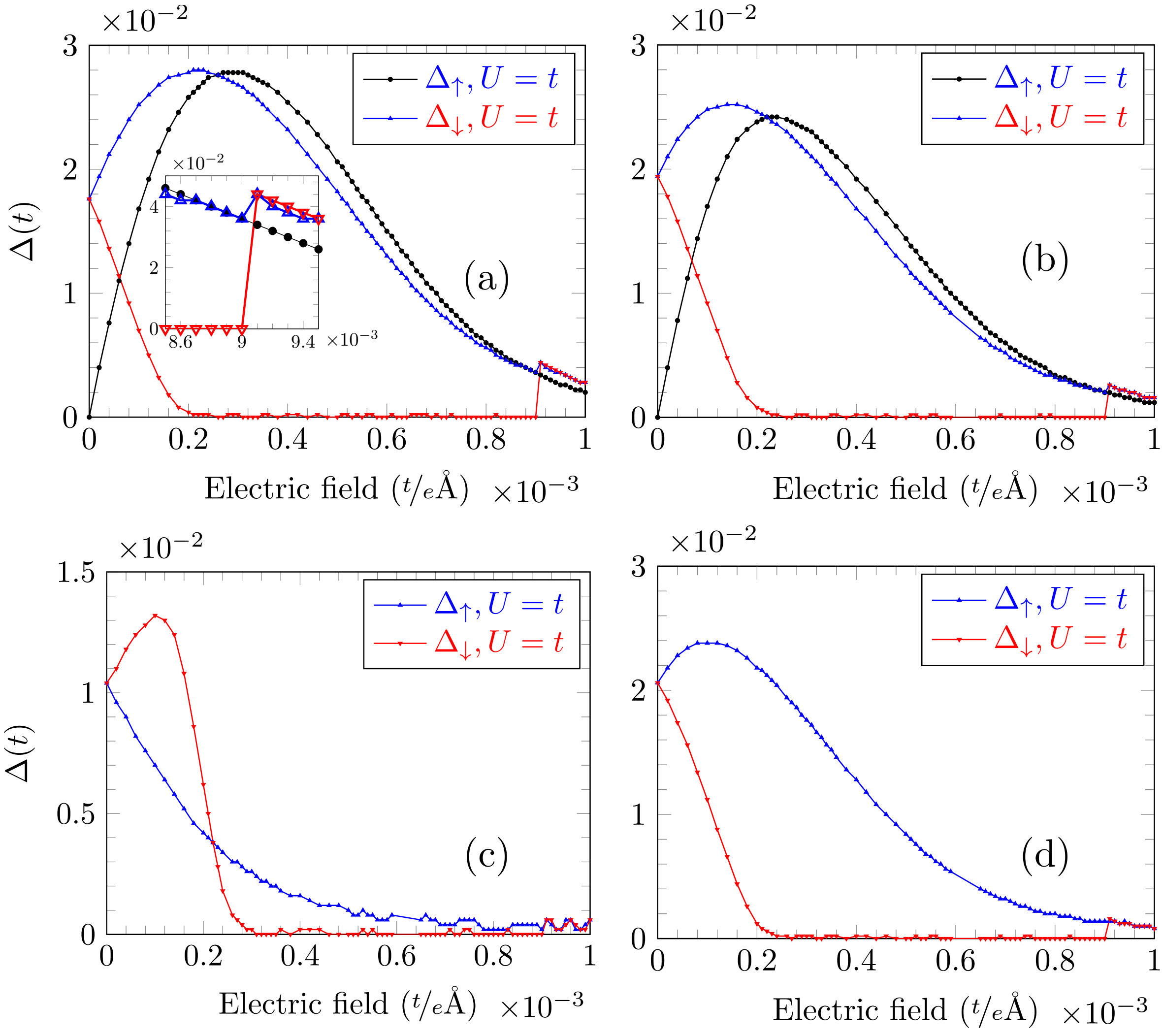

Figure 5.11: Gap evolution of a 112-ZGNR with respect to a transverse electric field. **(a)** The system experiences no strain, $A = 0$. **(b)** Strain is applied to the nanoribbon, $(A, b) = (2.5d, 10d)$ **(c)** Strain with $(A, b) = (5d, 7d)$ parameters, and **(d)** Strain with $(A, b) = (5d, 20d)$ parameters.

6

Conclusions

The proposal of this thesis was to develop theoretical approaches able to present a good description of graphene and hexagonal boron nitrate nanoribbon systems within extended tight binding models. We were particularly interested in modelling a hybrid system composed of a graphene nanoribbon embedded in two h-BN nanoribbons that could predict some of the main important band structure features next to the Fermi energy, revealed by density function theory results. Some effort has been put in investigating the half-metallicity phenomena that happens for a simple zigzag graphene nanoribbon in the presence of an electric field, and also for the hybrid system chosen of mixed graphene and h-BN nanoribbons in the absence of external fields.

With this in mind we analyze first the main aspects of the electronic properties of graphene and h-BN nanoribbons. Simple tight binding approximations were used as starting points and real-space normalization schemes are followed to derive Green's functions, total and local density of states and also the conductance. The hybrid graphene-BN nanoribbon system is studied via Hubbard-like model Hamiltonian within a mean field approximation. Edge potentials were proposed as corrections for on-site energies. Also, interface potentials between both systems were taken into account as extra corrections, to investigate how the BN-graphene nanoribbon interfaces are perturbed. Optimal tight-binding parameters are found from DFT calculations that are performed here by following the Quantum Espresso code, based on density-functional theory, plane waves and pseudopotentials. As predicted, due to different electronegativities of the boron and nitrogen atoms, an electric field is induced across the zigzag graphene strip, breaking the spin degeneracy of the electronic band structure. This is illustrates in the spin-dependent band structures, density of states and conductance results. We have also studied the evolution of the spin-dependent gaps as a function of an external electric field applied in the transversal direction of the nanoribbons. The results are actually relevant to propose this family of hybrid structures for possible applications in spintronic devices.

To deal with more real hybrid system we take into account the existence of some imperfections in the central region of the structures. Then, we studied the effects of impurities along the embedded graphene stripe and at the interface regions. We found that the energy gap sizes may be properly engineered by controlling the spatial doping process and, moreover, that binding energy impurity calculations may be used to study impurity diffusion processes along the mixed nanoribbons. We show that substitutional impurities may enhance half-metallic response. Different impurity configurations and the corresponding energy stabilities were studied.

As a second proposed theme we considered zigzag graphene nanoribbons under mechanical deformations that may be considered as central elements in the novel field of straintronics. Because strained folds can be engineered on graphene samples on appropriate substrates, we study their effects on graphene transport properties and on the local density of states. It is important to remark that various strain geometries have been theoretically proposed recently to produce specific properties as robust pseudomagnetic fields, but that their experimental realization has been limited to some particular examples in the literature. We have shown the existence of an enhanced local density of states along the direction of the strained fold that originates from localization of higher energy states and provides extra conductance channels at lower energies. Conductance calculations reveal extra channels within the energy range corresponding to the first conductance plateau for the undeformed ribbon, in addition to those due to edge states. Band structure calculations confirm that these channels were originated from higher energy states that localize along the strained fold-like area. More important, we have shown that states with the same velocity show real space valley polarization. In other words the results indicated that a current injected along the deformed structure will be split into two currents: one along the center of the strained fold constituted by states from one valley, and another running at its sides with contributions from states of the other valley. In addition to exhibiting sublattice symmetry breaking, these states are valley polarized, with quasiballistic properties in smooth disorder potentials. These findings could be tested in properly engineered experimental settings.

As an extension of the previous work we started an investigation on the half-metallic properties and the effects of Coulomb correlations on spatially inhomogeneous strain in graphene nanoribbons. A recent experimental setup of a graphene membrane laying over random-sized-SiO2 nanospheres generates periodic "strain pockets" on the graphene sheet[129]. The inhomogeneous deformation present in the samples produces confinement effects, that are expected to enhance local interactions. Experimental transport measurements show an oscillatory dependence on doping and an external magnetic field. Those results share similarities with quantum dot systems, where a Hubbard term successfully accounts for the effects of on-site electronic repulsion. The study of these systems are relevant because they can be used as a unique platform for electronic structure engineering to mix bandgap modulation, electronic confinement, and electronic interaction and may lead to a variety of responses such as spin-filtering properties, Mott insulator phase systems, or showing similar electronic properties to an array of quantum dots.

It is important to mention that different theoretical tools and approaches have been developed for all these studies and that the combination of them was seen to be quite important to a better description of our nanostructured system. Following these ideas we are also investigating now the role played by external magnetic fields on the graphene and BN isolated nanoribbons on lifting other degeneracies that are clearly marked in the respective band structures.

Bibliography

[1] J. H. Meng, X. W. Zhang, X. B. Wang, H. L.and Ren, C. H. Jin, Z. G. Yin, X. Liu, and H. Liu. Synthesis of in-plane and stacked graphene/hexagonal boron nitride heterostructures by combining with ion beam sputtering deposition and chemical vapor deposition. *Nanoscale*, 7:16046–16053, 2015. x, 3, 4

[2] W. Jang, H. Kim, Y. Shin, M. Wang, S. Jang, M. Kim, S. Lee, S. Kim, Y. Song, and S. Kahng. Observation of spatially-varying fermi velocity in strained-graphene directly grown on hexagonal boron nitride. *Carbon*, 74:139–145, 2014. x, xi, 5, 6, 7

[3] L. Liu, J. Park, D. A. Siegel, K. F. McCarty, K. W. Clark, W. Deng, L. Basile, J. C. Idrobo, A.-P. Li, and G. Gu. Heteroepitaxial growth of two-dimensional hexagonal boron nitride templated by graphene edges. *Science*, 343(6167):163–167, 2014. x, 3, 5, 44

[4] N. Levy, S. A. Burke, K. L. Meaker, M. Panlasigui, A. Zettl, F. Guinea, A. H. Castro Neto, and M. F. Crommie. Strain-induced pseudo–magnetic fields greater than 300 tesla in graphene nanobubbles. *Science*, 329(5991):544–547, 2010. xi, 6

[5] A. H. Castro Neto. Selected Topics in Graphene physics. *ArXiv e-prints*, April 2010. xi, 26

[6] Young-Woo Son, Marvin L. Cohen, and Steven G. Louie. Energy gaps in graphene nanoribbons. *Phys. Rev. Lett.*, 97:216803, Nov 2006. xii, 34, 39, 60, 64

[7] M. Fujita, K. Wakabayashi, K. Nakada, and K. Kusakabe. Peculiar localized state at zigzag graphite edge. *Journal of the Physical Society of Japan*, 65(7):1920–1923, 1996. xii, 34, 39, 68

[8] A. Pakdel, Y. Bando, and D. Golberg. Nano boron nitride flatland. *Chem. Soc. Rev.*, 43:934–959, 2014. xii, 42

[9] X. Zhong, R. G. Amorim, R. H. Scheicher, R. Pandey, and S. P. Karna. Electronic structure and quantum transport properties of trilayers formed from graphene and boron nitride. *Nanoscale*, 4:5490–5498, 2012. xii, 44, 46

[10] J. E. Padilha, Renato Borges Pontes, and Adalberto Fazzio. Bilayer graphene on h-bn substrate: investigating the breakdown voltage and tuning the bandgap by electric field. *Journal of Physics: Condensed Matter*, 24(7):075301, 2012. xii, 44, 46

[11] Yabo Gao, Yanfeng Zhang, Pengcheng Chen, Yuanchang Li, Mengxi Liu, Teng Gao, Donglin Ma, Yubin Chen, Zhihai Cheng, Xiaohui Qiu, Wenhui Duan, and Zhongfan Liu. Toward single-layer uniform hexagonal boron nitrideâgraphene patchworks with zigzag linking edges. *Nano Letters*, 13(7):3439–3443, 2013. PMID: 23758663. xii, 47

[12] J. Nakamura, T. Nitta, and A. Natori. Electronic and magnetic properties of BNC ribbons. *Phys. Rev. B*, 72:205429, Nov 2005. xii, 45, 48

[13] F. Zheng, K. Sasaki, R. Saito, W. Duan, and B.-L. Gu. Edge states of zigzag boron nitride nanoribbons. *Journal of the Physical Society of Japan*, 78(7):074713, 2009. xiii, i, 5, 23, 43, 45, 49, 51, 75

[14] C.-H. Park and S. G. Louie. Energy gaps and stark effect in boron nitride nanoribbons. *Nano Letters*, 8(8):2200–2203, 2008. PMID: 18593205. xiii, 55

[15] S. Bhowmick, A. K. Singh, and B. I. Yakobson. Quantum dots and nanoroads of graphene embedded in hexagonal boron nitride. *The Journal of Physical Chemistry C*, 115(20):9889–9893, 2011. xiii, 56, 57, 62

[16] R. Carrillo-Bastos, C. León, D. Faria, A. Latgé, E. Y. Andrei, and N. Sandler. Strained fold-assisted transport in graphene systems. *Phys. Rev. B*, 94:125422, Sep 2016. xv, xvi, 8, 68, 73, 77

[17] N. Greenwookd and A. Earnshaw. *Chemistry of the Elements. Second edition.* Elsevier Butterworth-Heinemann, 2005. i, 43

[18] R. Zhao, J. Wang, M. Yang, Z. Liu, and Z. Liu. BN-embedded graphene with a ubiquitous gap opening. *The Journal of Physical Chemistry C*, 116(39):21098–21103, 2012. i, 51, 55, 61, 62

[19] K. I. Bolotin, K. J. Sikes, Z. Jiang, M. Klima, G. Fudenberg, J. Hone, P. Kim, and H. L. Stormer. Ultrahigh electron mobility in suspended graphene. *Solid State Communications*, 146(9–10):351 – 355, 2008. 1

[20] C. Kittel. *Introduction to Solid State Physics, 8th edition.* Wiley, New York, 2004. 1

[21] A. H. Castro Neto, F. Guinea, N.M.R. Peres, K.S. Novoselov, and A.K. Geim. The electronic properties of graphene. *Rev. Mod. Phys.*, 81:109–162, Jan 2009. 1

[22] A. Geim M. Katsnelson, K. Novoselov. Chiral tunnelling and the klein paradox in graphene. *Nature Physics*, 2:620–625, August 2006. 1

[23] A. Celis, M. N. Nair, A. Taleb-Ibrahimi, E. H. Conrad, C. Berger, W. A. de Heer, and A. Tejeda. Graphene nanoribbons: fabrication, properties and devices. *Journal of Physics D: Applied Physics*, 49(14):143001, 2016. 1

[24] K. S. Novoselov, A. K. Geim, S. V. Morozov, D. Jiang, Y. Zhang, S. V. Dubonos, I. V. Grigorieva, and A. A. Firsov. Electric field effect in atomically thin carbon films. *Science*, 306(5696):666 –669, 2004. 1, 32, 33

[25] G. *et al* Bhimanapati. Recent advances in two-dimensional materials beyond graphene. *ACS Nano*, 9(12):11509–11539, 2015. PMID: 26544756. 2

[26] D. Akinwande *et al.* A review on mechanics and mechanical properties of 2d materialsâgraphene and beyond. *Extreme Mechanics Letters*, 13:42 – 77, 2017. 2

[27] Xiaolin Li, Xinran Wang, Li Zhang, Sangwon Lee, and Hongjie Dai. Chemically derived, ultrasmooth graphene nanoribbon semiconductors. *Science*, 319(5867):1229–1232, 2008. 2, 35

[28] J. Campos-Delgado, J. M. Romo-Herrera, X. Jia, D. A. Cullen, H. Muramatsu, Y. Ahm Kim, T. Hayashi, Z. Ren, D. J. Smith, Y. Okuno, T. Ohba, H. Kanoh, K. Kaneko, M. Endo, H. Terrones, M. S. Dresselhaus, and M. Terrones. Bulk production of a new form of sp2 carbon: Crystalline graphene nanoribbons. *Nano Letters*, 8(9):2773–2778, 2008. PMID: 18700805. 2

[29] J. Cai, P.. Ruffieux, R. Jaafar, M. Bieri, T. Braun, S. Blankenburg, M. Muoth, Ari P. Seitsonen, M. Saleh, X. Feng, K. Mullen, and R. Fasel. Atomically precise bottom-up fabrication of graphene nanoribbons. *Nature*, 466(7305):470–473, Jul 2010. 2

[30] L. Jiao, X. Wang, G.. Diankov, Hailiang Wang, and H. Dai. Facile synthesis of high-quality graphene nanoribbons. *Nat Nano*, 5(5):321–325, May 2010. 2

[31] A. L. Elías, A. R. Botello-Méndez, D. Meneses-Rodríguez, V. Jehová González, D. Ramírez-González, L. Ci, E. Muñoz Sandoval, P. M. Ajayan, H. Terrones, and M. Terrones. Longitudinal cutting of pure and doped carbon nanotubes to form graphitic nanoribbons using metal clusters as nanoscalpels. *Nano Letters*, 10(2):366–372, 2010. PMID: 19691280. 2

[32] V. Fal'ko. Graphene: Quantum information on chicken wire. *Nature Physics*, 3:151, 2007. 2

[33] Y. Son, M. L. Cohen, and S. G. Louie. Half-metallic graphene nanoribbons. *Nature*, 444:347–349, November 2006. 2, 40, 57, 62

[34] A. Pakdel, X. Wang, C. Zhi, Y. Bando, K. Watanabe, T. Sekiguchi, T. Nakayama, and D. Golberg. Facile synthesis of vertically aligned hexagonal boron nitride nanosheets hybridized with graphitic domains. *J. Mater. Chem.*, 22, 2012. 2

[35] X. Li, X. Wu, X. C. Zeng, and J. Yang. Band-gap engineering via tailored line defects in boron-nitride nanoribbons, sheets, and nanotubes. *ACS Nano*, 6(5):4104–4112, 2012. PMID: 22482995. 3

[36] A. K. Geim and I. V. Grigorieva. Van der waals heterostructures. *Nature*, 499(7459):419–425, Jul 2013. Perspectives. 5

[37] D. Moldovan, M. Ramezani Masir, and F. M. Peeters. Electronic states in a graphene flake strained by a gaussian bump. *Phys. Rev. B*, 88:035446, Jul 2013. 6, 68

[38] R. Carrillo-Bastos, D. Faria, A. Latgé, F. Mireles, and N. Sandler. Gaussian deformations in graphene ribbons: Flowers and confinement. *Phys. Rev. B*, 90:041411, Jul 2014. 68

[39] F. Guinea, M. I. Katsnelson, and A. K. Geim. Energy gaps and a zero-field quantum hall effect in graphene by strain engineering. *Nat Phys*, 6(1):30–33, Jan 2010.

[40] Vitor M. Pereira and A. H. Castro Neto. Strain engineering of graphene's electronic structure. *Phys. Rev. Lett.*, 103:046801, Jul 2009.

[41] Vitor M. Pereira, A. H. Castro Neto, and N. M. R. Peres. Tight-binding approach to uniaxial strain in graphene. *Phys. Rev. B*, 80:045401, Jul 2009. 69

[42] F. de Juan, M. Sturla, and M. A. H. Vozmediano. Space dependent fermi velocity in strained graphene. *Phys. Rev. Lett.*, 108:227205, May 2012.

[43] J. L. Mañes, F. de Juan, M. Sturla, and M. A. H. Vozmediano. Generalized effective hamiltonian for graphene under nonuniform strain. *Phys. Rev. B*, 88:155405, Oct 2013.

[44] J. V. Sloan, A. A. Pacheco Sanjuan, Z. Wang, C. Horvath, and S. Barraza-Lopez. Strain gauge fields for rippled graphene membranes under central mechanical load: An approach beyond first-order continuum elasticity. *Phys. Rev. B*, 87:155436, Apr 2013.

[45] E. Prada, P. San-Jose, G. León, M. M. Fogler, and F. Guinea. Singular elastic strains and magnetoconductance of suspended graphene. *Phys. Rev. B*, 81:161402, Apr 2010.

[46] M. M. Fogler, F. Guinea, and M. I. Katsnelson. Pseudomagnetic fields and ballistic transport in a suspended graphene sheet. *Phys. Rev. Lett.*, 101:226804, Nov 2008.

[47] M.A.H. Vozmediano, M.I. Katsnelson, and F. Guinea. Gauge fields in graphene. *Physics Reports*, 496(4):109 – 148, 2010.

[48] M. Mucha-K. and V.I. Fal'ko. Pseudo-magnetic field distribution and pseudo-landau levels in suspended graphene flakes. *Solid State Communications*, 152(15):1442 – 1445, 2012. Exploring Graphene, Recent Research Advances.

[49] D. Faria, A. Latgé, S. E. Ulloa, and N. Sandler. Currents and pseudomagnetic fields in strained graphene rings. *Phys. Rev. B*, 87:241403, Jun 2013.

[50] D. Gradinar, M. Mucha-K., H. Schomerus, and V. I. Fal'ko. Transport signatures of pseudomagnetic landau levels in strained graphene ribbons. *Phys. Rev. Lett.*, 110:266801, Jun 2013.

[51] D. A. Bahamon and Vitor M. Pereira. Conductance across strain junctions in graphene nanoribbons. *Phys. Rev. B*, 88:195416, Nov 2013.

[52] Hui Yan, Yi Sun, Lin He, Jia-Cai Nie, and Moses H. W. Chan. Observation of landau-level-like quantization at 77 k along a strained-induced graphene ridge. *Phys. Rev. B*, 85:035422, Jan 2012.

[53] M. Neek-Amal and F. M. Peeters. Strain-engineered graphene through a nanostructured substrate. i. deformations. *Phys. Rev. B*, 85:195445, May 2012. 6

[54] C. N. Lau, W. Bao, and J. Velasco. Properties of suspended graphene membranes. *Materials Today*, 15(6):238–245, 2012. 6

[55] N.N. Klimov, S. Jung, S. Zhu, T. Li, C. A. Wright, S. D. Solares, D. B. Newell, N. B. Zhitenev, and J. A. Stroscio. Electromechanical properties of graphene drumheads. *Science*, 336(6088):1557–1561, 2012.

[56] H. Lim, J. Jung, R. S. Ruoff, and Y. Kim. Structurally driven one-dimensional electron confinement in sub-5-nm graphene nanowrinkles. *Nature Communications*, 6(8601), 2015. 6, 7

[57] T. Georgiou, L. Britnell, P. Blake, R. V. Gorbachev, A. Gholinia, A. K. Geim, C. Casiraghi, and K. S. Novoselov. Graphene bubbles with controllable curvature. *Applied Physics Letters*, 99(9):093103, 2011.

[58] T. Mashoff, M. Pratzer, V. Geringer, T. J. Echtermeyer, M. C. Lemme, M. Liebmann, and M. Morgenstern. Bistability and oscillatory motion of natural nanomembranes appearing within monolayer graphene on silicon dioxide. *Nano Letters*, 10(2):461–465, 2010. PMID: 20058873. 6

[59] M. Y. Han and P. Kim. Graphene nanoribbon devices at high bias. *Nano Convergence*, 1(1):1, Feb 2014. 6

[60] D. Bischoff, A. Varlet, P. Simonet, M. Eich, H. C. Overweg, T. Ihn, and K. Ensslin. Localized charge carriers in graphene nanodevices. *Applied Physics Reviews*, 2(3):031301, Jul 2015. 6

[61] J. Baringhaus, M. Ruan, F. Edler, A. Tejeda, M. Sicot, A. Taleb-Ibrahimi, A.-P. Li, Z. Jiang, E. H. Conrad, C. Berger, C. Tegenkamp, and W. A. de Heer. Exceptional ballistic transport in epitaxial graphene nanoribbons. *Nature*, 506(7488):349–354, 2014. 6

[62] S. Datta. *Quantum Transport: Atom to transistor*. Cambridge University PRESS, 2005. 11, 14

[63] M. Di Ventra. *Electrical Transport in Nanoscale Systems*. Cambridge University Press, 2008. 12

[64] S. Datta. *Electronic Transport in Mesoscopic Systems, 1st edition, pp 152*. Cambridge University Press, 1995. 14

[65] M. Paulsson. Non equilibrium Green's functions for dummies: Introduction to the one particle NEGF equations. *arXiv:cond-mat/0210519v2 [cond-mat.mes-hall]*, 2006. 14, 15, 17

[66] D. A. Areshkin and Branislav K. Nikolić. Electron density and transport in top-gated graphene nanoribbon devices: First-principles green function algorithms for systems containing a large number of atoms. *Phys. Rev. B*, 81:155450, Apr 2010. 15

[67] E. Economou. *Green's Functions in Quantum Physics*. Springer, 2006. 18

[68] J. C. Slater and G. F. Koster. Simplified LCAO method for the periodic potential problem. *Phys. Rev.*, 94:1498–1524, Jun 1954. 27, 51

[69] W. Kohn and L. J. Sham. Self-consistent equations including exchange and correlation effects. *Phys. Rev.*, 140:A1133–A1138, Nov 1965. 28

[70] P. Giannozzi *et al.* Quantum ESPRESSO: a modular and open-source software project for quantum simulations of materials. *Journal of Physics: Condensed Matter*, 21(39):395502 (19pp), 2009. 28, 51

[71] David Vanderbilt. Soft self-consistent pseudopotentials in a generalized eigenvalue formalism. *Phys. Rev. B*, 41:7892–7895, Apr 1990. 28

[72] A. Calzolari, N. Marzari, I. Souza, and M. B. Nardelli. Ab initio transport properties of nanostructures from maximally localized Wannier functions. *Phys. Rev. B*, 69:035108, Jan 2004. 29, 51

[73] A. Ferretti, B. Bonferroni, A. Calzolari, and M. B. Nardelli. Want code. 29, 51

[74] D. Tománek and S. G. Louie. First-principles calculation of highly asymmetric structure in scanning-tunneling-microscopy images of graphite. *Phys. Rev. B*, 37:8327–8336, May 1988. 31

[75] D. Gosálbez-Martínez, J. J. Palacios, and J. Fernández-Rossier. Spin-orbit interaction in curved graphene ribbons. *Phys. Rev. B*, 83:115436, Mar 2011. 31

[76] N. D. Mermin. Crystalline order in two dimensions. *Phys. Rev.*, 176:250–254, Dec 1968. 32

[77] S. Cahangirov, M. Topsakal, E. Aktürk, H. Şahin, and S. Ciraci. Two- and one-dimensional honeycomb structures of silicon and germanium. *Phys. Rev. Lett.*, 102:236804, Jun 2009. 32

[78] P. R. Wallace. The band theory of graphite. *Phys. Rev.*, 71:622–634, May 1947. 32

[79] J. W. McClure. Band structure of graphite and de haas-van alphen effect. *Phys. Rev.*, 108:612–618, Nov 1957. 33

[80] J. C. Slonczewski and P. R. Weiss. Band structure of graphite. *Phys. Rev.*, 109:272–279, Jan 1958. 33

[81] H. W. Kroto, J. R. Heath, S. C. O'Brien, R. F. Curl, and R. E. Smalley. C60: Buckminsterfullerene. *Nature*, 318:162–163, November 1985. 33

[82] S. Iijima. Helical microtubules of graphitic carbon. *Nature*, 354:56–58, November 1991. 33

[83] S. Bae, H. Kim, Youngbin. Lee, X. Xu, J. Park, Y. Zheng, J. Balakrishnan, T. Lei, H. Ri Kim, Young Il. Song, Y.-J. Kim, K. Kim, B. Ozyilmaz, J.-H. Ahn, B. Hong, and S Iijima. Roll-to-roll production of 30-inch graphene films for transparent electrodes. *Nat Nano*, 5(8):574–578, Aug 2010. 33

[84] Y. Lee, S. Bae, H. Jang, S. Jang, S. Zhu, S. Sim, Y. Song, B. Hong, and J. Ahn. Wafer-scale synthesis and transfer of graphene films. *Nano Letters*, 10(2):490–493, 2010. PMID: 20044841. 33

[85] S. Cahangirov, M. Topsakal, and S. Ciraci. Armchair nanoribbons of silicon and germanium honeycomb structures. *Phys. Rev. B*, 81:195120, May 2010. 33

[86] Hong Li, Nabil Al-Aqtash, Lu Wang, Rui Qin, Qihang Liu, Jiaxin Zheng, Wai-Ning Mei, R.F. Sabirianov, Zhengxiang Gao, and Jing Lu. Electromechanical switch in metallic graphene nanoribbons via twisting. *Physica E: Low-dimensional Systems and Nanostructures*, 44(10):2021 – 2026, 2012. 35

[87] K. Tanaka, S. Yamashita, H. Yamabe, and T. Yamabe. Electronic properties of one-dimensional graphite family. *Synthetic Metals*, 17(1-3):143 – 148, 1987. 35

[88] K. Kobayashi. Electronic structure of a stepped graphite surface. *Phys. Rev. B*, 48:1757–1760, Jul 1993. 35

[89] K. Wakabayashi and S. Dutta. Nanoscale and edge effect on electronic properties of graphene. *Solid State Communications*, 152(15):1420–1430, 2012. 38

[90] Y. Li, Z. Zhou, C. R. Cabrera, and Zhongfang Chen. Preserving the edge magnetism of zigzag graphene nanoribbons by ethylene termination: Insight by clar's rule. 3:2030 EP –, Jun 2013. Article. 38

[91] Wen cai Yi, Wei Liu, Lei Zhao, Rashed Islam, Mao sheng Miao, and Jing yao Liu. Asymmetric passivation of edges: a route to make magnetic graphene nanoribbons. *RSC Adv.*, 7:27932, 2017. 38

[92] C. Tao, L. Jiao, O. Yazyev, Y. Chen, J. Feng, X. Zhang, R. Capaz, J. Tour, A. Zettl, H. Dai S. Louie, and M. Crommie. Spatially resolving edge states of chiral graphene nanoribbons. *Nature Physics*, 7:616–620, August 2011. 38

[93] K. Nakada, M. Fujita, G. Dresselhaus, and M. S. Dresselhaus. Edge state in graphene ribbons: Nanometer size effect and edge shape dependence. *Phys. Rev. B*, 54:17954–17961, Dec 1996. 38

[94] Wen-Xiao Wang, Mei Zhou, Xinqi Li, Si-Yu Li, Xiaosong Wu, Wenhui Duan, and Lin He. Energy gaps of atomically precise armchair graphene sidewall nanoribbons. *Phys. Rev. B*, 93:241403, Jun 2016. 39

[95] R. Ramprasad, Paul von Allmen, and L. R. C. Fonseca. Contributions to the work function: A density-functional study of adsorbates at graphene ribbon edges. *Phys. Rev. B*, 60:6023–6027, Aug 1999. 41

[96] P. Lou. A new kind of edge-modified spin semiconductor in graphene nanoribbons. *The Journal of Physical Chemistry C*, 118(8):4475–4482, 2014. 41

[97] G. Cassabois, P. Valvin, and B. Gil. Hexagonal boron nitride is an indirect bandgap semiconductor. *Nature Photonics*, 10, 2016. 42

[98] J. Xue, J. Sanchez-Yamagishi, D. Bulmash, P. Jacquod, A. Deshpande, K. Watanabe, T. Taniguchi, P. Jarillo-Herrero, and Brian J. LeRoy. Scanning tunnelling microscopy and spectroscopy of ultra-flat graphene on hexagonal boron nitride. *Nature Materials*, 10:282, 2011. 42

[99] R. Decker, Y. Wang, V. W. Brar, W. Regan, H.-Z. Tsai, Q. Wu, W. Gannett, A. Zettl, and M. F. Crommie. Local electronic properties of graphene on a bn substrate via scanning tunneling microscopy. *Nano Letters*, 11(6):2291–2295, 2011. PMID: 21553853. 42

[100] C. R. Dean, A. F. Young, I. Meric, L. Wang C. Lee, S. Sorgenfrei, K. Watanabe, P. Kim T. Taniguchi, K. L. Shepard, and J. Hone. Boron nitride substrates for high-quality graphene electronics. *Nature Nanotechnology*, 5:722, 2010. 42

[101] K. Lee, H. Shin, J. Lee, I. Lee, G. Kim, J. Choi, and S. Kim. Large-scale synthesis of high-quality hexagonal boron nitride nanosheets for large-area graphene electronics. *Nano Letters*, 12:714, 2012. 42

[102] J.-W. Huang, C. Pan, S. Tran, B. Cheng, K. Watanabe, T. Taniguchi, C. N. Lau, and M. Bockrath. Superior current carrying capacity of boron nitride encapsulated carbon nanotubes with zero-dimensional contacts. *Nano Letters*, 15(10):6836–6840, 2015. PMID: 26390365. 42

[103] K. Watanabe, T. Taniguchi1, and H. Kanda. Direct-bandgap properties and evidence for ultraviolet lasing of hexagonal boron nitride single crystal. *Nature Materials*, 3, 2004. 43

[104] Xiao-jun Wu, Men-hao Wu, and Xiao Cheng Zeng. Chemically decorated boron-nitride nanoribbons. *Frontiers of Physics in China*, 4(3):367–372, Sep 2009. 43

[105] L. Lai, J. Lu, G. Luo, J. Zhou, R. Qin, Z. Gao, and W.juan Mei. Magnetic properties of fully bare and half-bare boron nitride nanoribbons. *The Journal of Physical Chemistry C*, 113:2273, 2009. 43

[106] Y. Wang, Y. Ding, and J. Ni. Electronic structures of fe-terminated armchair boron nitride nanoribbons. *Appl. Phys. Lett.*, 99, 2011.

[107] H.M. Rai, S.K. Saxena, V. Mishra, R. Late, R. Kumar, P.R. Sagdeo, N.K. Jaiswal, and P. Srivastava. Half-metallicity in armchair boron nitride nanoribbons: A first-principles study. *Solid State Communications*, 212:19 – 24, 2015. 43

[108] W. Chen, Y. Li, G. Yu, C.-Z. Li, S. B. Zhang, Z. Zhou, and Z. Chen. Hydrogenation: A simple approach to realize semiconductor-half-metal-metal transition in boron nitride nanoribbons. *Journal of the American Chemical Society*, 132(5):1699–1705, 2010. PMID: 20085366. 43

[109] R. Quhe, J. Zheng, G. Luo, Q. Liu, R. Qin, J. Zhou, D. Yu, S. Nagase, W.-N. Mei, Z. Gao, and J. Lu. Tunable and sizable band gap of single-layer graphene sandwiched between hexagonal boron nitride. *NPG Asia Mater*, 4:e6, Feb 2012. 44

[110] P. Sutter, R. Cortes, J. Lahiri, and E. Sutter. Interface formation in monolayer graphene-boron nitride heterostructures. *Nano Letters*, 12(9):4869–4874, 2012. PMID: 22871166. 44

[111] Z. Liu, L. Ma, G. Shi, W. Zhou, Y. Gong, S. Lei, X. Yang, J. Zhang, J. Yu, K. P. Hackenberg, A. Babakhani, J.-C. Idrobo, R. Vajtai, J. Lou, and P. M. Ajayan. In-plane heterostructures of graphene and hexagonal boron nitride with controlled domain sizes. *Nat Nano*, 8(2):119–124, Feb 2013. 44

[112] J. M. Pruneda. Origin of half-semimetallicity induced at interfaces of c-bn heterostructures. *Phys. Rev. B*, 81:161409, Apr 2010. 51

[113] L. A. Agapito, A. Ferretti, A. Calzolari, S. Curtarolo, and M. Buongiorno Nardelli. Effective and accurate representation of extended bloch states on finite hilbert spaces. *Phys. Rev. B*, 88:165127, Oct 2013. 53

[114] Yi Ding, Yanli Wang, and Jun Ni. Electronic properties of graphene nanoribbons embedded in boron nitride sheets. *Appl. Phys. Lett*, 95:123105, 2009. 57

[115] C. Ritter, S. S. Makler, , and A. Latgé. Energy-gap modulations of graphene ribbons under external fields: A theoretical study. *Phys. Rev. B*, 77:195443, May 2008. 60, 64

[116] K. Zhao, M. Zhao, Z. Wang, and Y. Fan. Tight-binding model for the electronic structures of sic and bn nanoribbons. *Physica E: Low-dimensional Systems and Nanostructures*, 43(1):440 – 445, 2010. 60

[117] F. Culchac, R. Capaz, A.T. Costa, and A. Latgé. Magnetic response of zigzag nanoribbons under electric fields. *Journal of Physics: Condensed Matter*, 26(21):216002, 2014. 62

[118] T. Nomura, D. Yamamoto, and S. Kurihara. Electric field effects in zigzag edged graphene nanoribbons. *Journal of Physics: Conference Series*, 200(6):062015, 2010. 62

[119] Ken ichi Sasaki, Shuichi Murakami, and Riichiro Saito. Gauge field for edge state in graphene. *Journal of the Physical Society of Japan*, 75(7):074713, 2006. 62, 70

[120] K. S. Novoselov, A. Mishchenko, A. Carvalho, and A. H. Castro Neto. 2d materials and van der waals heterostructures. *Science*, 353(6298), 2016. 64

[121] A.J. Du, Sean C. Smith, and G.Q. Lu. *Chemical Phys. Lett.*, 44(181), 2007. 66

[122] A. H. Castro Neto and Francisco Guinea. Electron-phonon coupling and raman spectroscopy in graphene. *Phys. Rev. B*, 75:045404, Jan 2007. 69

[123] L. Landau and E. M. Lifshitz. *Theory of elasticity. (Volumen 7 of A Course of Theoretical Physics)*. Pergamon Press, Cambridge, 1970. 69

[124] M. I. Katsnelson. *Graphene: Carbon in Two Dimensions*. Cambridge University Press, Cambridge, 2012. 69

[125] J. C. Slonczewski and P. R. Weiss. Band structure of graphite. *Phys. Rev.*, 109:272–279, Jan 1958. 70

[126] Hidekatsu Suzuura and Tsuneya Ando. Phonons and electron-phonon scattering in carbon nanotubes. *Phys. Rev. B*, 65:235412, May 2002. 71

[127] K. Wakabayashi, K. Sasaki, T. Nakanishi, and T. Enoki. Electronic states of graphene nanoribbons and analytical solutions. *Science and Technology of Advanced Materials*, 11(5):054504, 2010. 78

[128] T. S. Li, Y. C. Huang, S. C. Chang, Y. C. Chuang, and M. F. Lin. Transport properties of ab-stacked bilayer graphene nanoribbons in an electric field. *The European Physical Journal B*, 64(1):73–80, 2008. 78

[129] Y. Zhang, Y. Kim andd M. Gilbert, and N. Mason. Electron transport in strain superlattices of graphene. *arXiv:1703.05689 [cond-mat.mes-hall]*, 2017. 85